# Instability and mixing in a turbulent stratified Taylor-Couette Flow

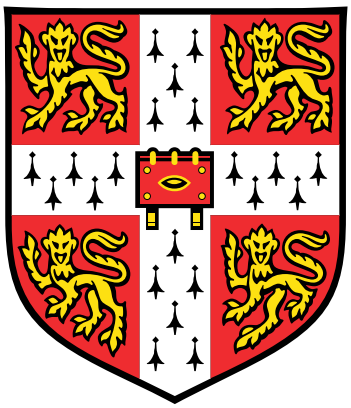

**Kanwar Nain Singh**

Supervisor: Prof. Colm-cille P. Caulfield

Department of Applied Mathematics and Theoretical Physics
University of Cambridge

This dissertation is submitted for the degree of
*Doctor of Philosophy*

Homerton College

September 2019

# Declaration

I hereby declare that this dissertation is the result of my own work and includes nothing which is the outcome of work done in collaboration except where specifically specified in the text. It is not substantially the same as any that I have submitted, or, is being concurrently submitted for a degree or diploma or other qualification at the University of Cambridge or any other University or similar institution. I further state that no substantial part of my thesis has already been submitted, or, is being concurrently submitted for any such degree, diploma or other qualification at the University of Cambridge or any other University or similar institution.

Kanwar Nain Singh
September 2019

# Acknowledgements

I am grateful to Prof. Colm Caulfield for giving me a chance to work on this intriguing topic and all the discussions and support so far in this PhD work. I would also like to thank Prof. Stuart Dalziel for all the experimental help either directly or via Jamie. I would definitely want to thank Dr. Jamie Partridge for the long hours spent discussing and working towards experiments, analysis and understanding the data. I also really appreciate the help I received from Chris Howland towards the stability analysis formulation and subsequent code debugging. I am also extremely grateful to the technicians, David, Colin, Paul, Andy and John for always being their to help with any technical difficulties. In the end, I would like to thank SGPC-Cambridge Commonwealth Trust scholarship for providing me with the financial support throughout this PhD tenure.

I am also incredibly thankful to my girlfriend, Swapan who has been extremely supportive especially during the last days of this PhD. I would also like to thank all my friends in Cambridge for all those amazing memories over the years.

# Abstract

In this thesis, we investigate mixing mechanisms in a stably stratified turbulent Taylor-Couette flow, which is the flow in the annular region of two co-axial cylinders, both capable of rotating at different speeds independently, in the presence of vertical stable stratification. Oglethorpe (2014) found that, for an initially linearly stratified Taylor-Couette (STC) flow with fixed outer cylinder, the flow spontaneously forms well-mixed layers of constant height separated by sharp density gradient interfaces. She also observed a quasi-periodic mixing phenomenon across the interfaces. Through laser induced fluorescence and particle images velocimetery, we discover the structure of this mixing instability. We find that the mixing occurs as a result of a flow phenomenon generated by two in-phase boundary trapped waves, with azimuthal wavenumber $m = 1$, riding on the interface. We further look into the flux across the interface resulting from this instability. We find that, for high stratification, the molecular diffusion plays a significant part in the overall observed flux across the interface, and the buoyancy flux does not tend to a constant as previously discussed by Oglethorpe (2014). As a result, we find that the entrainment coefficient, $E \sim Ri_B^{-3/2}$, where $Ri_B = g' \frac{R_2}{(\Omega R_1)^2}$ with $R_1$ and $R_2$ being the inner and the outer cylinder radii respectively and $\Omega$ being the angular velocity of the inner cylinder, which is consistent with the classical observations of Turner (1968). Overall, we observe that the buoyancy flux monotonically increases as the mixing occurs (i.e. with reducing $Ri_B$) to a maximum where the interface is overturned by the turbulent eddies present in each of the layers. Furthermore, we perform stability analysis of the STC flow using a base flow having a dependence in both the radial $r$ and the axial $z$ directions,using the mean turbulent flow profile varying in $r$ as the base velocity profile and a density profile with a sharp gradient in the $z$ direction as the base density profile. Using our model, we are able to consistently predict the period of the empirically observed instability, which suggests that this instability has its origins in a linear instability. Finally, we look at the implications of rotating the outer cylinder on the observed instability. Through qualitative experiments and stability analysis, we discover that the same instability exists even outside the domain of centrifugal instability prescribed by Rayleigh's criterion (Rayleigh, 1917).

# Table of contents

# List of figures

# List of tables

# Chapter 1

# Introduction and Motivation

## 1.1 Stratified Flows

Our earth's oceans and atmosphere are both stably stratified on average, where the density decreases with height. Also, flow in the oceans and the atmosphere is known to be turbulent. Turbulent mixing has a significant contribution in the circulation of the oceans (Ferrari & Wunsch, 2009). Hence, stably-stratified turbulent flows are common in nature, and play a key role in climate dynamics (Lilly, 1983).

As per the Intergovernmental Panel on Climate Change 2013 (IPCC, 2013) report, owing to the increase in greenhouse gases concentrations in the atmosphere, the average land and ocean surface temperature has been increasing. This is principally because of radiative forcing, i.e. the greenhouse gases, carbon dioxide and others, in the atmosphere restrict the heat to be radiated back into the outer atmosphere which leads to an increase in the total energy stored in the lower atmospheric layer. It was also reported in IPCC (2013) that most of this energy is stored in the oceans (greater than 90%), with about 30% in the deep ocean (below 700 m) and more than 60% in the upper ocean (0-700 m). Not only for heat, but the oceans also serve as a sink for carbon dioxide as well. It has been reported that about 30% of the anthropogenic carbon dioxide emissions are absorbed in the oceans (IPCC, 2013).

The absorbed heat and carbon dioxide in the ocean gets transported to the deep ocean owing to the ocean circulation, which eventually gets released back into the atmosphere (Munk & Wunsch, 1998). Since the timescale of this circulation is on the order of centuries (Alford *et al.*, 2013), the ocean hence acts as a heat and carbon sink over this timescale, and helps in mitigation of the overall global warming effect. On the other hand, the anthropogenic carbon dioxide concentrations in the atmosphere have been increasing rapidly (increasing by 40% in last 4 decades, as per the IPCC (2013)), which has resulted in an increase in average land and ocean temperatures. Now with this continuous warming of the ocean, it is

not certain but quite plausible that it might weaken the ocean circulation and in turn, further enhance the heating up of the atmosphere (Alford *et al.*, 2013; IPCC, 2013; Schmittner *et al.*, 2005). Therefore, to ascertain the likely effects of the anthropogenic climate change, one needs to understand ocean circulation processes.

Some of the turbulent mixing processes occur over scales that are much smaller than those being resolved by present ocean circulation models (Eden *et al.*, 2014). But these processes play a critical role in determining properties of ocean circulation (Ferrari & Wunsch, 2009; Ivey *et al.*, 2008), and therefore, require parametric modeling. Ocean circulation models can be very sensitive to the parameterisation of the vertical mixing processes (Jayne, 2009; Zaron & Moum, 2009). A good understanding of how these mixing processes in the oceans should be parameterised is lacking (Jayne, 2009; Wunsch & Ferrari, 2004), making it difficult to predict future ocean states. The long term aim of this PhD is to have a better understanding of the turbulent mixing processes in a stably stratified environment, and have some parameters which could be incorporated to these parameterisation models to improve their accuracy.

In a stably-stratified flow, buoyancy typically acts as a stabilizing force by suppressing the vertical motion. For mixing to happen, work is therefore required to be done against the buoyancy force, thereby increasing potential energy of the fluid. The strength of stratification can be quantified in terms of a Bulk Richardson number $(Ri_B)$, which tells us about the relative strength of the buoyancy force per unit volume $(F_B)$ compared to the inertial force $(F_I)$ of the flow, i.e.

$$F_B \sim g\Delta\rho,\ F_I \sim \rho\frac{u^2}{d},\ Ri_B = \frac{F_B}{F_I} = \frac{g\Delta\rho d}{\rho u^2}, \tag{1.1}$$

where $g$ is acceleration due to gravity, $\Delta\rho$ is the density difference over the vertical extent of the flow (which is positive, as $\rho$ increases with depth since the flow is stably stratified), and $d$ and $u$ are are the length and velocity scales respectively. It can also be interpreted as the ratio of potential energy required for mixing $(\sim g\Delta\rho d)$ to the available kinetic energy $(\propto \rho u^2)$. This means at low $Ri_B$, there is not enough energy available to work against the buoyancy (Linden, 1979). However, mixing still happens at high enough $Ri_B$ as was observed by Turner (1979) in the oceans, where mixing happens even when $Ri_B$ is large, $O(10^2)$. Although the buoyancy force is quite strong, there are always some regions locally where inertial effects can still cause mixing.

Local stability of the flow is characterised by a local Richardson number, $Ri$, which is defined as the ratio of buoyancy frequency to the vertical shear,

$$Ri = \frac{N^2}{(\frac{\partial u}{\partial z})^2}, \tag{1.2}$$

where N is the buoyancy frequency,

$$N^2 = -\frac{g}{\rho}\frac{\partial \rho}{\partial z}.$$

In a stratified turbulent flow, there can be a non-uniform variation of velocity and density with depth, which has also been observed in the ocean (Bluteau *et al.*, 2013; Sherwin, 2010).These variations in $\frac{\partial u}{\partial z}$ and $\frac{\partial \rho}{\partial z}$ result in formation of local mixing regions where $Ri \ll Ri_B$.This means these regions are locally present where kinetic energy of the flow is large enough to work against the buoyancy forcing and have well mixed 'layers' in those regions, separated by 'interfaces' where $Ri \gg Ri_B$. This suggests the formation of step-like vertical density profiles which has also been observed within the ocean (Holbrook & Blacic, 2010; Turner, 1979)). The formation of these step-like density profiles is often attributed to double-diffusive effects (Sommer *et al.*, 2013), but at the same time these layers have also been observed in freshwater lakes (Simpson & Woods, 1970), so may not always be due to double diffusion. Layering has also been observed in laboratory experiments with initial linear stratification (Holford & Linden, 1999; Ruddick *et al.*, 1989). Therefore, understanding of the vertical fluxes of buoyancy through a layered stratification, can also give us insights into the fluxes of heat and salt in the ocean.

## 1.2 Energetics of stratified turbulence

From the Navier-Stokes equations and applying the Boussinesq approximation, with an assumption that there is no net transport across the boundaries of the domain, the evolution of kinetic energy of a stratified flow, per unit mass, can be described as

$$\frac{d\mathscr{K}}{dt} = -\mathscr{B} - \mathscr{E}, \tag{1.3}$$

where

$$\mathscr{K} = \frac{1}{2}\langle|\mathbf{u}|^2\rangle,\ \mathscr{B} = \frac{1}{\rho_o}\langle g\rho' w\rangle,\ \mathscr{E} = \nu\langle|\nabla\mathbf{u}|^2\rangle.$$

Here $\mathscr{K}$ is the kinetic energy density, $\mathscr{B}$ is the vertical flux of buoyancy, $\mathscr{E}$ is the viscous dissipation, $\rho_o$ is the reference density, $\rho'$ is the perturbation from the hydrostatic density, $\mathbf{u}$ is the velocity vector, $w$ is the vertical velocity, $\nu$ is the viscosity and the angle brackets denote volume average (Peltier & Caulfield, 2003). The evolution of potential energy density,

$$\frac{d\mathscr{P}}{dt} = \langle \frac{g\rho' z}{\rho_o} \rangle, \tag{1.4}$$

which can also be interpreted as

$$\frac{d\mathscr{P}}{dt} = \mathscr{B} + \mathscr{D}_m, \tag{1.5}$$

where $\mathscr{D}_m$ is the rate of increase of $\mathscr{P}$ in a stable density distribution in the absence of any fluid motion. In a turbulent flow, $\mathscr{B}$ varies on scales much smaller than those presently resolved in the ocean circulation models and hence, parameterisation for $\mathscr{B}$ is required.

To date, there have been many studies trying to understand the fluxes of heat and salt in the ocean and find better parametrisation for the models. Munk (1966) used field measurement data of the temperature and salinity structure to get average fluxes in the ocean. Many experiments have been done in laboratories to study the turbulent mixing in a stably stratified environment, typically starting with either a linear density gradient or having two homogeneous layers of different density separated by an interface, with turbulence being generated either mechanically (Linden, 1980; Park *et al.*, 1994; Turner, 1968; Zellouf *et al.*, 2005) or by shear at the density interface (Kato & Phillips, 1969; Narimousa & Fernando, 1987; Strang & Fernando, 2001). However, more recently there have been studies investigating stably-stratified turbulent mixing in Taylor-Couette flow, both in two-layered stratified (Guyez *et al.*, 2007; Oglethorpe *et al.*, 2013; Woods *et al.*, 2010) and linearly stratified environment (Oglethorpe *et al.*, 2013), where turbulence is generated by horizontal shear unlike the previous experiments where turbulence was generated either by mechanical stirring or by large scale vertical shear at the interface.

There is a non-monotonic relationship found in these studies between vertical buoyancy flux and the bulk Richardson number $(Ri_B)$. For Boussinesq flow (i.e. $\Delta\rho \ll \rho_o$), the bulk Richardson number is defined as,

$$Ri_B = \frac{g\Delta\rho}{\rho_o}\frac{d}{u^2},$$

where $\rho_o$ is a reference density and $\frac{g\Delta\rho}{\rho_o}$ is a measure of the vertical buoyancy variation. At small $Ri_B$, the buoyancy forcing is not significant enough to affect the flow and the buoyancy flux, $\mathscr{B}$ increases with increasing $Ri_B$ (as $\Delta\rho$ increases) while $w$ remains almost unchanged.

As $Ri_B$ increases further, the buoyancy force becomes significant enough to suppress some vertical fluid motion, thereby reducing $w$. Hence, possibly there is a critical $Ri_B$ where the flux then starts to reduce as $Ri_B$ is increased further as the decrease in $w$ becomes more significant than an increase in $\Delta\rho$. In the past experiments with mechanical stirring, at large $Ri_B$, the flux either reduced to zero or stays constant as $Ri_B$ continues to increase. However, for Taylor-Couette flow experiments i.e. in the presence of horizontal shear, Guyez *et al.* (2007) found that the flux increases with $Ri_B$ at large $Ri_B$, while later Woods *et al.* (2010) observed that the flux remains constant with increasing $Ri_B$ in a similar configuration. Oglethorpe *et al.* (2013) performed experiments to observe the complete evolution of buoyancy flux over the whole range of $Ri_B$, starting with a high enough $Ri_B$ until the point when the fluid was fully mixed. They were the first to find a universal flux curve for stably stratified Taylor-Couette flow, as shown in figure 1.4. It is explained in more details in the following sections.

## 1.3 Mixing across an interface in stratified flows

The presence of turbulence in two-layer stratified flows causes mixing as a result of fluid from one layer being entrained into the other layer and vice-versa. The entrainment concept originally hails from the theory of plumes by Morton *et al.* (1956), where they assume that the velocity of the fluid being entrained in the plume, $u_e$ is proportional to its characteristic vertical velocity

$$u_e = Ew \tag{1.6}$$

where $w$ is the characteristic flow velocity. They called this constant of constant of proportionality $E$ as the 'entrainment coefficient'. Ellison & Turner (1959) suggested that for the stratified flows, since the entrainment occurs in the vertical direction and across a density gradient which is capable of inhibiting the vertical motion, the entrainment coefficient $E$ is a decreasing function of bulk Richardson number $Ri_B$.

The entrainment coefficient is useful in quantifying the amount of mixing by measuring the amount of fluid being transported across the interface. However, we are primarily interested in the buoyancy flux, which is proportional to the change of potential energy. Linden (1979) defined a non-dimensional parameter 'flux Richardson number', $R_f$ as a measure of the buoyancy flux, which is the fraction of the available kinetic energy being converted to potential energy by mixing the stratification. The rate of change of potential energy per unit volume for a stratified flow with two layers of equal height is given by

$$\mathscr{B} = \frac{1}{\rho_0}\langle g\rho' w\rangle = \frac{1}{2}\frac{g\Delta\rho}{\rho_0}u_e, \tag{1.7}$$

since the fluid parcels with density variations of $\Delta\rho$ are entrained with velocity $u_e$ into each layer occupying half of the total volume. The rate of supply of kinetic energy per unit volume goes as

$$\frac{d\mathscr{K}}{dt} \propto \frac{1}{2}u^2\left(\frac{u}{d}\right), \tag{1.8}$$

where $d$ and $u$ are the characteristic length and velocity scales in the flow respectively. As shown by Linden (1979), $R_f$ is given as

$$R_f = \frac{\mathscr{B}}{d\mathscr{K}/dt} \propto \frac{u_e}{u}\frac{g\Delta\rho}{\rho_0}\frac{d}{u^2} \propto ERi_B. \tag{1.9}$$

Now if

$$E \propto Ri_B^{-n}, \tag{1.10}$$

since $E$ is a decreasing function of $Ri_B$, this implies

$$R_f \propto Ri_B^{1-n}. \tag{1.11}$$

Turner (1968) stirred the fluid in the two layers using an oscillating grid, and found that

$$E \propto Ri_B^{-1} \qquad \text{and} \qquad E \propto Ri_B^{-3/2}, \tag{1.12}$$

for a heat and salt stratification respectively. This means that for heat stratification, the $R_f$ remains constant with changing $Ri_B$, and for salt stratification, $R_f$ decreases as $Ri_B$ increases. Later, Zellouf *et al.* (2005) conducted similar experiments to Turner (1968) and found that for salt stratification, the buoyancy flux was constant at high $Ri_B$ and increased with reducing $Ri_B$ at a lower $Ri_B$. Linden (1980) performed experiments by dropping a horizontal grid through the density interface and found that as $Ri_B$ increased from zero, $R_f$ increases as well up to a maximum, then $R_f$ decreases as $Ri_B$ increases further.

There have been some shear mixing experiments on stratified flows looking at the flux across the density interface as well. Narimousa & Fernando (1987) used a closed-loop water channel, and investigated the mixing over a vertically sheared density interface. They found the buoyancy flux to be proportional to the rate of turbulent kinetic energy dissipation, hence, resulting in a constant $R_f$. They also observed a change in the nature of mixing between high and low $Ri_B$. They suggested that the mixing occurred due to the breakdown of large coherent vortices, while at high $Ri_B$, it is due to wave breaking. Later Strang & Fernando (2001) performed more detailed measurements of a similar experiment and found that the flux increases with increasing $Ri_B$ at low $Ri_B$ to a maximum, then starts to decrease till a point beyond which the flux appears to remain approximately constant with increasing $Ri_B$.

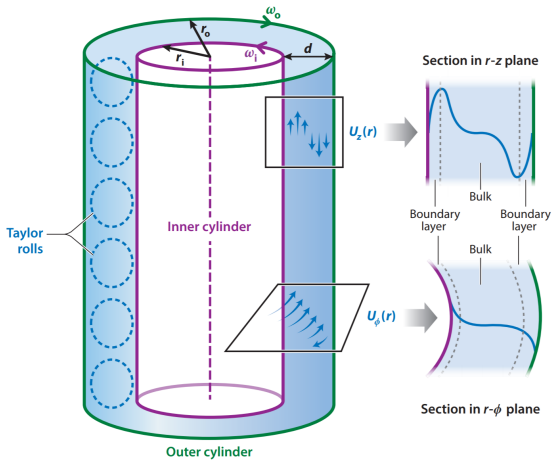


Fig. 1.1 A typical sketch of Taylor-Couette apparatus with unstratified flow, taken from Grossmann *et al.* (2016). $r_i$ and $r_o$ are the radii of the inner and outer cylinder respectively, and their respective angular velocities are $\omega_i$ and $\omega_o$. $d$ is the gap width. The dashed rolls represent the Taylor rolls, which are considered to be the largest eddies of the turbulent Taylor-Couette flow. Plot also shows the typical velocity profiles for the axial velocity ($U_z(r)$) and the azimuthal velocity ($U_\phi(r)$) in the boundary layers and the bulk.

More recently, Oglethorpe (2014) performed a horizontally sheared stratified experiment using a Taylor-Couette apparatus and found similar buoyancy flux behaviour as Strang & Fernando (2001).

Going through the literature, we found that there seems to be an ambiguity in the nature of stratified flows at high $Ri_B$, whether $R_f$ is constant or decreases with increasing $Ri_B$. However, it could also be possible that the flow behaves differently for grid-mixing experiments where the grid imposes a length scale on the flow, and for shear mixing experiments.

## 1.4 Taylor-Couette Flow

In this section, we review the features and the properties of Taylor-Couette flow, and then previous studies on mixing in a Taylor-Couette flow in the presence of a two-layer or linearly stratified environment. A Taylor-Couette apparatus consists of a set of two coaxial cylinders, both capable of rotating independently at different speeds. The annular region between the two cylinders is the test region and the flow in this region is called the Taylor-Couette flow.

Taylor-Couette flow is one of the classical hydrodynamics stability problems of great importance since the pioneering work of Couette (1890) and Taylor (1923). It is the flow in the annular region of two coaxial cylinders with vertical axes, both rotating independently. A typical sketch of the Taylor-Couette apparatus, taken from the annual rewiew on Taylor-

Couette flow by Grossmann *et al.* (2016), is shown in figure 1.1. This flow has been extensively in use to test various concepts of fluid dynamics such as instabilities (Coles, 1965; Donnelly, 1991; Tuckerman, 2014), non-linear dynamics (Smith & Townsend, 1982; Strogatz, 1994), pattern formation (Andereck *et al.*, 1986; Büchel *et al.*, 1996), and turbulence (Lathrop *et al.*, 1992).

Taylor-Couette flow is a canonical flow that is experimentally accessible with high precision, given the simple geometries and high symmetries. In fact, Taylor-Couette flow has an edge over Rayleigh-Bénard flow (another commonly used flow, which is a buoyancy-driven flow produced when the fluid is heated from below and cooled from above) for studying turbulence because of its experimental ease to achieve the 'ultimate' turbulent regime (Grossmann *et al.*, 2016) where even the wall boundary layers are turbulent. Also, on the other hand, there exists a strong analogy between the Taylor-Couette flow and the pipe flow, which is considered one of the most important turbulent flows from a technological and industrial point of view (Grossmann *et al.*, 2016), making Taylor-Couette flow an important research case in industrial research as well.

The Taylor-Couette flow is produced by rotating either the inner or the outer cylinder, or both and is known to go through various flow regimes (see Andereck *et al.* (1986)). It is quantified in dimensionless form by the respective Reynolds numbers (which is the ratio of inertial to viscous forces in the flow),

$$Re_{1,2} = \frac{R_{1,2}\Omega_{1,2}\Delta_R}{\nu},$$

where $R_1$ and $R_2$ are the inner and outer radii respectively, $\Delta_R = R_2 - R_1$ is the annular gap width, $\Omega_1$ and $\Omega_2$ are angular velocities of inner and outer cylinder respectively and $\nu$ is the kinematic viscosity of the flow. Taylor-Couette flow is known to be linearly stable for outer cylinder rotation and for a fixed or only slowly rotating inner cylinder. The onset of instabilities at increasing Reynolds number of the inner cylinder is caused by the driving centrifugal force and can be estimated by force balance arguments (Grossmann *et al.*, 2016). The flow could also be characterised using another set of non-dimensional parameters, Taylor number and Rossby number. The Taylor number tells us about the relative strength of the inertial forces due to rotation of the fluid about an axis in comparison to the viscous forces, and is defined as

$$Ta = 4Re_1^2 \frac{(1-\mu)}{\eta^2} \frac{(1-\eta)}{(1+\eta)}$$

where $\eta = \frac{R_1}{R_2}$ is the radius ratio and $\mu = \frac{\Omega_2}{\Omega_1}$ is the rotation ratio. The Rossby number ($Ro$) is defined as the ratio of the shear rate $[\frac{(\Omega_1-\Omega_2)}{\Delta_R}]$ to solid-body rotation ($\frac{\Omega_2}{R_1}$). The inverse of

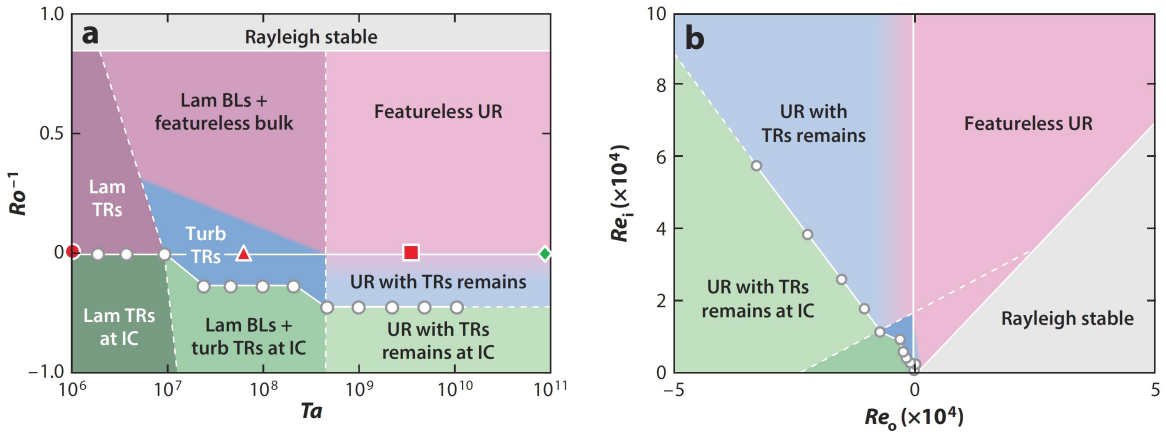


Fig. 1.2 Different regimes in the unstratified Taylor-Couette flow presented $(a)$ on a $(Ta, Ro^{-1})$ phase diagram and $(b)$ on a $(Re_o, Re_i)$ phase diagram. This plot was taken from Grossmann *et al.* (2016). Abbreviations: IC, inner cylinder; TR, Taylor roll; BL, Boundary layer; UR, ultimate regime. The green diamond on the plot represents the flow parameters used for purely centrifugally unstable experiments discussed in this thesis.

Rosby number, $Ro^{-1}$ characterizes the strength of driving Coriolis force, and is given by

$$Ro^{-1} = \frac{2\Omega_2 \Delta_R}{|\Omega_1 - \Omega_2| R_1} = 2\frac{(1-\eta)}{\eta}\frac{\mu}{(1-\mu)}.$$

The richness of unstratified Taylor-Couette flow and various regimes that were observed can be seen in figure 1.2, which is the plot showing different regimes on a $(Ta, Ro^{-1})$ phase space taken from Grossmann *et al.* (2016).

In our present work, we have principally considered the centrifugally unstable flow with the outer cylinder stationary (Rayleigh, 1917). The flow is induced by rotating only the inner cylinder i.e. $\mu = 0$. Even for this specific case, a variety of different regimes have been observed. The instabilities start to develop in the flow at some critical Taylor number, $Ta_c$ (Chandrasekhar, 1961; Rayleigh, 1965), and the gap between the cylinders is filled with a vertical series of axisymmetric coherent structures called the 'Taylor vortices' (Di Prima & Swinney, 1985). As $Ta$ increases, the length scale of these vortices starts to decrease and the flow goes through a series of different regimes (for example, wavy vortices, modulated wavy vortices, etc.). At around $Ta \approx 700 Ta_c$, the coherence length scale of structures becomes smaller than the characteristic integral length scale, which is the gap width $\Delta_r$, and the flow becomes turbulent (Grossmann *et al.*, 2016; Koschmieder, 1979). The mean flow still consists of large-scale vortices, called 'turbulent Taylor vortices' which are statistically axisymmetric. As the $Ta$ increases further, the flow transits to the featureless turbulence regime.

Rayleigh (1965) found the critical Taylor number for the onset of instabilities for a range of radius ratios. Oglethorpe (2014) did a spline interpolation to the data and found the critical Taylor number for her experiments. She performed experiments with Reynolds number, $Re = O(10^4)$ and Taylor number $Ta > O(10^4)$, thereby ensuring that these numbers were far from those at which the flow first becomes turbulent and expected the flow to be fully turbulent. Since in our experiments, the dimensions of the apparatus used (details in the next section) are quite similar to those of Oglethorpe (2014), we believe that our experiments are in the fully turbulent regime as well. Referring to figure 1.2, our experiments lie on the right most end of the $(Ta, Ro^{-1})$ phase diagram on the $Ro^{-1} = 0$ line, in the featureless 'ultimate' regime (represented by green diamond in figure 1.2).

In the past, the interaction of buoyancy forces with centrifugal forces has not received much attention, even though stratified flows have direct relevance and application to geophysical, environmental and astrophysical flows. Stratified Taylor-Couette (STC) flow is the horizontally sheared flow where the energy input and hence, turbulence generated is uniformly distributed throughout the length of the tank, unlike many other stratified flow experiments where the energy input is very localised in the flow. STC, thus, acts as a good representation of various real life fluid flow scenarios, one such being the mixing in the oceans. Moreover, STC, like its unstratified case, is known to be prone to instabilities as well, so much so that instabilities have been observed in the domain outside of that set by Rayleigh's criterion (Rayleigh, 1917). The Rayleigh criterion states that the flow is centrifugally unstable, in the inviscid limit, when angular momentum is decreasing radially,

$$\frac{d(r^2\Omega)}{dr} < 0$$

or

$$\mu < \eta^2.$$

It was first shown by Molemaker *et al.* (2001) and (Yavneh *et al.*, 2001) theoretically that STC could have instabilities in the Rayleigh's centrifugally stable domain. They found that the dominant instability is non-axisymmetric and, therefore, is different from the conventional Taylor vortices. They postulated that the sufficient condition for inviscid instability in the STC was $\mu > 1$. Recently Park & Billant (2013) found the instability even in the domain of increasing angular momentum, i.e. $\mu < 1$. They came to a striking conclusion that the STC is always linearly unstable, and the only exception is the case of solid body rotation. All these instabilities came from the resonance of two boundary trapped helicoidal modes, and was named as stratorotational instability (SRI) by Dubrulle *et al.* (2005). SRI has also been

confirmed experimentally by Le Bars & Le Gal (2007) and computationally in the works of Shalybkov & Rüdiger (2005) and Rüdiger & Shalybkov (2009).

## 1.5 Mixing in Stratified Taylor-Couette (STC) flow

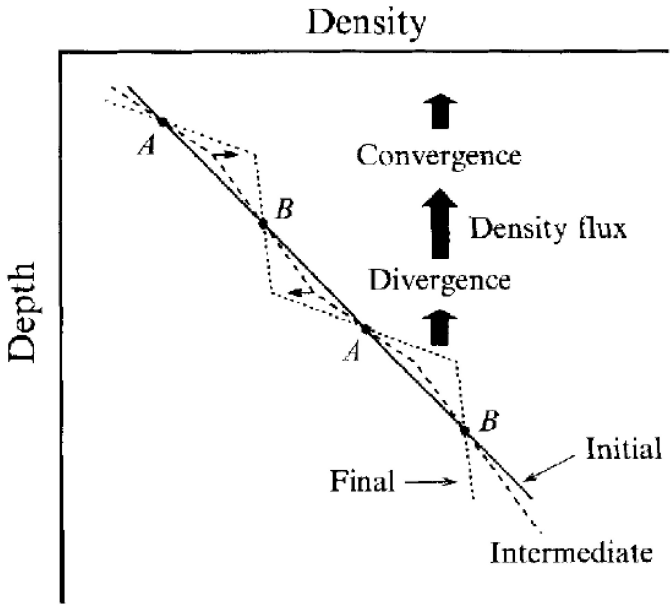


Fig. 1.3 Schematic of the layer formation process, as proposed by Phillips (1972). This diagram has been taken from Park *et al.* (1994). The solid and the dashed lines shows the initial linear stratification and a perturbation to this initial stratification respectively. The density gradient increases at points labeled A and decreases at points labeled B due to the perturbation. The dotted line shows the final density profile.

The first work on stratified Taylor-Couette flow was a theoretical study by Thorpe (1966), where it was found that the occurrence of the rolls in the azimuthal direction is delayed by the presence of stratification which reduces their vertical extent as well. The first experimental study on STC was later done by Boubnov *et al.* (1995), where they observed the layer formation in an initially linearly salt stratified experiment with a fixed outer cylinder. They found that the height of these layers, $h \sim \frac{\Omega d}{N}$, where $d$ was some fixed length scale in the experiment. Hua *et al.* (1997) and Caton *et al.* (1999, 2000) later revisited the work of Boubnov *et al.* (1995) numerically and experimentally respectively, and looked at the details of instability onset. Later Guyez *et al.* (2007) and Woods *et al.* (2010) looked at the buoyancy flux through a density interface in a two-layered stratified experiment. Flux Richardson number, $R_f$ which is the fraction of the available kinetic energy converted to potential energy by mixing the stratification, defined by Linden (1979) was used to quantify buoyancy flux,

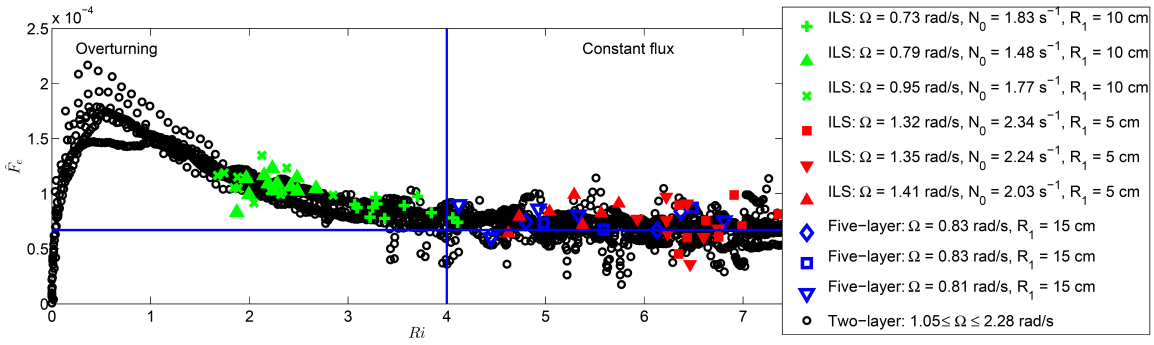


Fig. 1.4 Plot showing variation non-dimensional flux $\hat{F}_e$ through the density interfaces against bulk Richardson number $Ri$. $\hat{F}_e = \frac{\Delta_r}{(\Omega r_i)^3} F$, where $F$ is the buoyancy flux through the interface. This plot was taken from Oglethorpe (2014). Abbreviations: ILS, Initial linear stratification; IFL, Initial five-layer stratification; ITL, Initial two-layer.

given as

$$R_f \propto \frac{d}{u^3} F \ ,$$

where $d$ is the characteristic size of the turbulent eddies in the layers, and $u$ is the root-mean-square eddy velocity. Guyez *et al.* (2007) found that $R_f$ increased to a maximum with increasing $Ri_B$, then decreased with increasing $Ri_B$ and started increasing again at high $Ri_B$. On the other hand, Woods *et al.* (2010) only looked at high $Ri_B$, and found that $R_f$ remains constant with change in $Ri_B$. Oglethorpe (2014) looked at $R_f$ over a wide range of $Ri_B$, starting with a high $Ri_B$ till the point that the fluid was completely mixed. Her results at high $Ri_B$ were consistent with those of Woods *et al.* (2010). She suggested that the Reynolds number in experiments of Guyez *et al.* (2007) may not have been high enough and the flow may not be fully turbulent. Oglethorpe (2014) defined the non-dimensional buoyancy flux, $\hat{F}$ (which is proportional to $R_f$) as

$$\hat{F} = \frac{\Delta_r}{(\Omega r_1)^3} F \ . \tag{1.13}$$

Effectively this non-denationalisation assumed that both the flux and the dissipation had the inertial scaling $\frac{u^3}{d}$ where $d$ and $u$ are the length and velocity scales respectively. Here,

$$F = -\frac{H}{4} \frac{g}{\rho_o} \frac{d\Delta\rho}{dt} \ ,$$

where $\Delta_r$ is the annular gap width between the two cylinders and $H$ is the total height of the fluid. The non-dimensional flux curve she found for the two layer experiments over the whole range of bulk Richardson number is shown in figure 1.4.

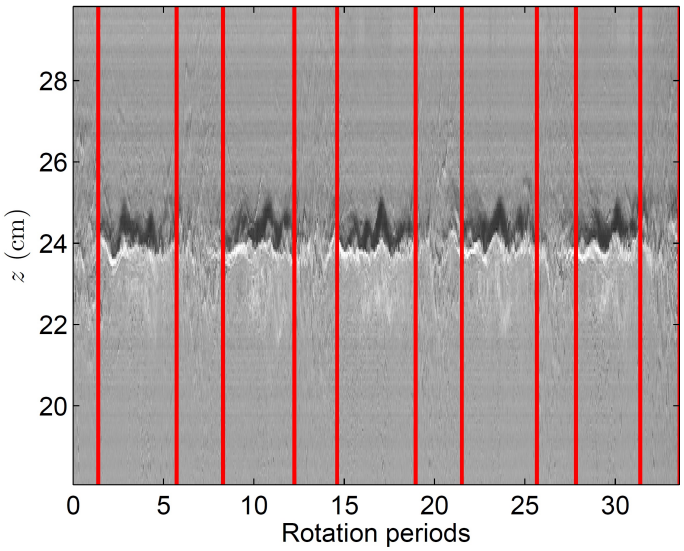


Fig. 1.5 Time series of a vertical slice for the shadowgraph images showing the presence of periodic mixing mechanism. This picture was taken from Oglethorpe (2014).

Oglethorpe (2014) also performed experiments with an initial linear stratification and an initial five-layered stratification and looked at the buoyancy flux through the interfaces. It was observed that the initially linearly stratified flow spontaneously forms layers, separated by sharp density gradient interfaces. The flux through these interfaces was very similar to that across the interface in an initial five-layered stratification or the initial two-layered stratification experiments (refer figure 1.4). She attributed this formation of layers to the 'Phillips Mechanism', shown in figure 1.3. According to Phillips (1972), a small perturbation from linear stratification will continue to grow, if the vertical buoyancy flux is decreasing with increasing density gradient. In the regions where density gradient decreases because of the perturbation (labeled B in figure 1.3), the flux is increased which makes the density gradient decrease further. This continues and eventually fluid around that region is well mixed. On the other hand, at regions where the density gradient increases, the flux further reduces as a result of this increase, which makes the density gradient to increase and eventually an interface is formed around that region with a sharp density gradient. This leads to the formation of a step-like density profile. She found that characteristic height of layers, $h \propto \frac{U_H}{N}$, where $U_H = \sqrt{\Delta_r r_i}\Omega$ is the horizontal velocity scale, consistent with Boubnov *et al.* (1995). By combining results from all of her experiments, she found a universal flux curve for the buoyancy flux, as shown in figure 1.4. It was found that for low $Ri_B$ ($Ri_B < Ri_c \approx 0.5$, where $Ri_c$ is the critical Richardson number where flux is maximum), the flux increases with $Ri_B$. For $Ri_c \leq Ri_B \leq Ri_a$ ($Ri_a$ is represented by blue vertical line in figure 1.4), it starts to decrease as $Ri_B$ increases and follows a power law. However, for high $Ri_B$ ($Ri_B > Ri_a \approx 4$), the flux

deviates from any power law decay and tends to a non-zero constant consistent with Woods *et al.* (2010). Oglethorpe (2014) also observed a periodic signal in density measurements at the interface (see figure 1.5), and she believed that this periodic structure was associated with the dominant mixing mechanism. Note the shadowgraph shows the integration of density gradients along the line of passage of light rays, and therefore, it is not possible to find the exact location and structure of the instability using shadowgraphy. She also performed a similar shadowgraph experiments but with the light projected from above and the bottom of the tank acting as a screen. Analysing this data, she came up with a mixing hypothesis. She hypothesized that the mixing mechanism consists of "$(i)$ mixing across the interface in the high shear and high speeds of the boundary layer of the inner cylinder, to create a region of mixed fluid within the boundary layer; $(ii)$ the release of this mixed fluid from the boundary layer and its subsequent development into a quasi-steady nonlinear travelling wave state, which appears to be an attracting state of the system and which transports mixed fluid radially outwards and around the annulus; $(iii)$ the homogenization of this mixed fluid into the layers by the large scale turbulent eddies in the layers" (Oglethorpe, 2014).

In this thesis, we investigate some of the open questions on STC flow that still exists. Specifically, we investigate the four following issues.

1. Oglethorpe (2014) found the universal flux curve for the STC flow in her experiments and suggests flux to be constant at $Ri_B > 4$. However, the flux curve was determined only for $Ri_B \lesssim 7$. Guyez *et al.* (2007), in their experiment with similar parameters, observed the flux to increase at high $Ri_B$. It still remains an open question as to the nature of the flux curve at higher $Ri_B$, especially at exceptionally strong stratification ($Ri_B \gg 1$).

2. Oglethorpe (2014) observed a periodic mixing phenomenon occurring on the interface in her shadowgraph recordings (refer to figure 1.5). No more quantitative information is available on the structure of this mixing event and its physical properties that result in mixing.

3. The periodic mixing event that exists on the interface is an extremely robust one and stays throughout the experiment. What is the mechanism behind the observed periodicity and what sustains it? Since the phenomenon is so robust at varying range of $Re$, could it be possible that this observed instability is related to a linear instability of the mean turbulent base flow?

4. An initially linearly stratified STC flow is known to be unstable even in the centrifugally stable regime i.e. radially increasing angular momentum (Rayleigh, 1917) and forms

the strato-rotational instability (SRI). The nature of the SRI is very different from that of a centrifugally unstable instability observed by Oglethorpe (2014). Would there be instability on the interface in a two-layer STC flow in a centrifugally stable regime? If it exists, could it be related to periodic mixing instability observed by Oglethorpe (2014) in a centrifugally unstable regime?

In this thesis, we look into the above open questions and make an attempt to provide answers. In chapter 2, we present information on observed buoyancy flux at high $Ri_B$. In chapter 3, we perform LIF and PIV analysis on a two-layer STC and present the discovered structure of the observed periodic mixing event. We then perform linear stability analysis using the mean turbulent velocity varying the in the radial direction and a two-layer density profile varying in the vertical direction as the base flow. The results are shown in chapter 4. In chapter 5, we discuss the implications on the observed instability by rotating the outer cylinder as well. Lastly, we perform some experiments at low Péclet number which are discussed in chapter 6. We draw our conclusions and suggest future directions of research in Chapter 7.

# Chapter 2

# Flux across the interface at high Richardson number

## 2.1 Introduction

In this chapter, the flux curve across the interface in a two-layer stratified Taylor-Couette flow is discussed in further detail, in order to find out what causes the flow to change its behaviour at a certain Richardson number resulting in a change in the nature of flux curve as observed by Oglethorpe *et al.* (2013).

Linearly stratified turbulent flows are known to spontaneously form layers (Holford & Linden, 1999; Park *et al.*, 1994; Ruddick *et al.*, 1989)), owing to the Phillips mechanism (refer to section 1.5). Oglethorpe (2014) also observed the layering for her initially linearly stratified Taylor-Couette experiments. She also found that the flux across the interface (refer to figure 1.4) and the observed mixing instability at the interface (discussed in further detail in chapter 3) is exactly the same as that in the two-layer stratified experiments. Therefore, in order to make things easier, two-layer stratified experiments are performed to study the mixing processes.

There are three previous studies of two-layer stratified Taylor-Couette flow, Guyez *et al.* (2007); Oglethorpe (2014); Woods *et al.* (2010), who have experimentally explored the buoyancy flux across the interface in a two-layer stratified Taylor-Couette flow with varying $\Delta\rho$. The buoyancy flux per unit area across the interface, $F$, is defined as

$$F = \frac{d}{dt}\int_0^{H/2} \frac{g(\rho(z,t)-\rho_0)}{\rho_0} dz, \tag{2.1}$$

where $H/2$ is the height of each layer with the interface being at $z = 0$, $g$ is the acceleration due to gravity, $\rho(z)$ is the density of the fluid, $\rho_0$ is a reference density (using Boussinesq approximation) and $\Omega$ is the rotation rate of the inner cylinder. The Reynolds number, $Re$, is defined as

$$Re = \frac{\Omega R_1 \Delta_R}{\nu}, \tag{2.2}$$

where $R_1$ is the radius of the inner cylinder, $\Delta_R$ is the gap width of the annulus and $\nu$ is the kinematic viscosity of the fluid. Since the fluid is well mixed in each of the two layers, the buoyancy flux equation (equation 2.1) can be written in terms of density difference across the interface, $\Delta\rho$, as (Oglethorpe, 2014)

$$F = -\frac{H}{4}\frac{g}{\rho_0}\frac{d\Delta\rho}{dt}, \tag{2.3}$$

where $\Delta\rho = \rho_{max} - \rho_{min}$ and $\rho_{max}$ is the density of the bottom heavier layer while $\rho_{min}$ is the density of the upper lighter layer. It is worth noting here that the rate of change of density in the each of the layers is half of the rate of change of density difference in the two layers (Woods *et al.*, 2010), which was used to derive equation 2.3. The strength of stratification is quantified using the bulk Richardson number, $Ri_B$, which is defined as

$$Ri_B = \frac{g\Delta\rho}{\rho_0}\frac{d}{u^2}, \tag{2.4}$$

where $d$ is the length scale and $u$ is the characteristic velocity of the turbulent flow. Oglethorpe (2014) found that the outer cylinder radius, $R_o$ and velocity of the fluid at the inner cylinder, $\Omega R_i$ to be the appropriate length scale and velocity scale respectively, and the same scaling has been used for the present study as well.

Guyez *et al.* (2007) performed their experiment at a Reynolds number of $Re = 3407$ and found that with increasing $Ri_B$, the flux, $F$ increases to a maximum, then decreases, and then start to increase again at high $Ri_B$. Woods *et al.* (2010) reproduced this experiment at a higher Reynolds number, $10^4 < Re < 10^5$, ensuring the flow is turbulent and looked at the flux across the interface only for a sufficiently high $Ri_B$. They found that, at high $Ri_B$, $F$ is a non-zero constant and is independent of the value of $Ri_B$. Oglethorpe *et al.* (2013) on the other hand, looked at $F$ over a wide range of $Ri_B$, starting from high $Ri_B$ until $Ri_B = 0$ where the fluid was completely mixed. They found a universal flux curve for the buoyancy

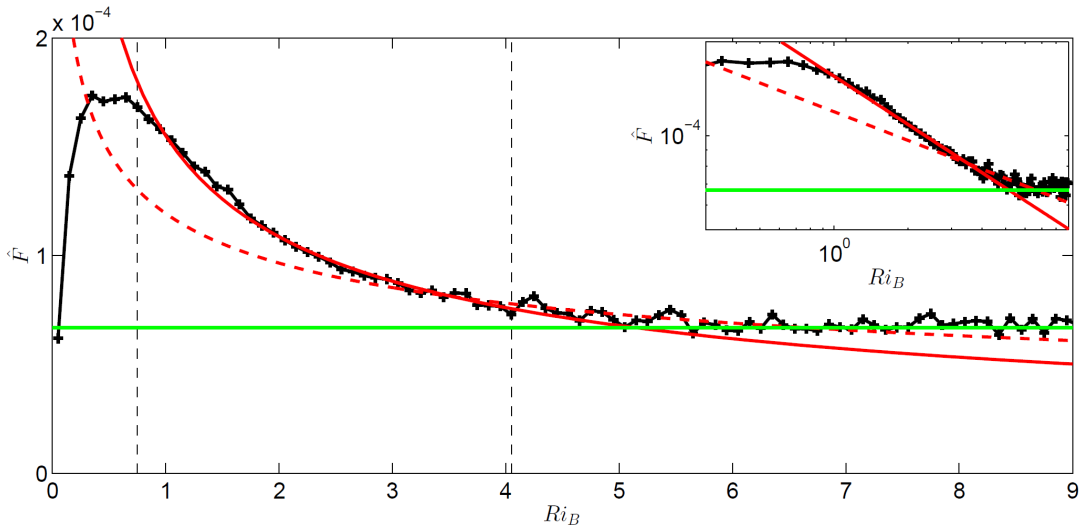


Fig. 2.1 Plot showing best-fit power laws to the flux data by Oglethorpe (2014). Here $\hat{F}$ is the non-dimensional flux defined in equation 1.13. The solid red line represents $\hat{F} \propto Ri_B^{-0.51}$, the dashed red line is $\hat{F} \propto Ri_B^{-0.31}$ and the green line is the asymptotic constant flux. The plot is copied from figure 2.8 of Oglethorpe (2014).

flux (refer to figure 1.4) for the full range of $Ri_B$. They reported that at high $Ri_B$, the flux remains constant with reducing $Ri_B$ and called it the 'asymptotic regime'. This is consistent with observations of Woods *et al.* (2010). The 'asymptotic regime' continues until a critical $Ri_B$ ($Ri_B \approx 4$) where the flow transits to the enhanced flux regime as the mixing continues (i.e. reducing $Ri_B$). This continues until another critical $Ri_B$ ($Ri_B \approx 0.75$) where the density difference across the interface is not strong enough to resist the vertical motion of fluid and it mixes completely. They believed that the mismatch with the data by Guyez *et al.* (2007) is because the experiments of Guyez *et al.* (2007) were performed at a lower Reynolds number and the flow was not fully turbulent, and there may be some effects of viscosity at high $\Delta\rho$.

The change of the flow behaviour from constant flux to enhanced flux was reported to be at a critical $Ri_B = 4$ by Oglethorpe (2014). They also explored the best-fit power law on their flux data and found two different power laws for different regions of the $Ri_B$ range studied, also pointing towards change in nature of the flow (refer to figure 2.1). They found that, in the enhanced flux regime, the buoyancy flux, $\hat{F} \propto Ri_B^{-0.51}$, which was consistent with the previous studies on stratified turbulence, such as those by Deardorff & Yoon (1984); Linden (1980); Turner (1968). On the other hand, for $2.75 < Ri_B < 7.5$, they found the best-fit power law to be $\hat{F} \propto Ri_B^{-0.31}$. Using the discussion in section 1.3, this would mean that the entrainment coefficient, $E \propto Ri_B^{-1.51}$ in the enhanced flux regime, $E \propto Ri_B^{-1.31}$ for $2.75 < Ri_B < 7.5$ and $E \propto Ri_B^{-1}$ for $Ri_B > 4$. Previous studies on stratified turbulence have

shown either $E \propto Ri_B^{-1}$ or $E \propto Ri_B^{-1.5}$, but none of them, to the best of our knowledge, have discussed such drastic change of entrainment behaviour.

In this chapter, we investigate the few open questions that still remain in regards to the flux across the interface in a two-layer Taylor-Couette flow, as mentioned below.

1. Guyez *et al.* (2007) performed their experiments at $Re = 3407$, which for an unstratified Taylor-Couette flow is in the regime of turbulent Taylor rolls (Grossmann *et al.*, 2016), which ensures that the flow, although not in the ultimate turbulent regime, was turbulent. We have also performed experiments at $Re = 3000$ and have found the same instability on the interface as observed by Oglethorpe (2014) (discussed in more detail in chapter 5). This leads us to the first open question, why is the buoyancy flux curve observed by Guyez *et al.* (2007) so different from that of Woods *et al.* (2010) and Oglethorpe *et al.* (2013)?

2. Oglethorpe (2014) observed the distinct transition of the flow behaviour from that of constant flux to that of enhanced flux at around $Ri_B = 4$. This is also shown by the fact that they were able to fit different power laws in different regions of the plot. In the enhanced flux regime, since the $\hat{F} \propto Ri_B^{-0.51}$, this means the entrainment coefficient, $E \propto Ri_B^{-1.51}$ (refer to section 1.3). For $Ri_B > 4$, the observed flux is constant, which gives $E \propto Ri_B^{-1}$. This leads to another open question as what makes the flow change the entrainment behaviour at $Ri_B = 4$?

3. As discussed in section 1.5, for an initial linear stratification to spontaneously form layers, the Phillips mechanism requires the flux to decrease with increasing density difference across the interface. Oglethorpe *et al.* (2013) for some of their experiments found the layer formation with density difference across the interfaces corresponding to the constant flux regime which violates the pre-requisite for the Phillips mechanism. The last open question is if the Phillips mechanism is the dominant mechanism of layer formation in stratified Taylor Couette flow?

## 2.2 Experiment

The experiments shown in this chapter use a Taylor-Couette apparatus, similar to that used by Woods *et al.* (2010) and Oglethorpe *et al.* (2013). It consists of two concentric cylinders with vertical axes, both capable of rotating at different speeds. The fluid is contained in the annular region between the cylinders. The outer cylinder has an inner radius of $R_2 = 24\,\mathrm{cm}$, and is made of transparent cast acrylic with a thickness of approximately 5 mm. It is attached to a turntable which can rotate at a range of angular velocities, $0.1\,\mathrm{rad\,s^{-1}} < \Omega_o < 3.4\,\mathrm{rad\,s^{-1}}$.

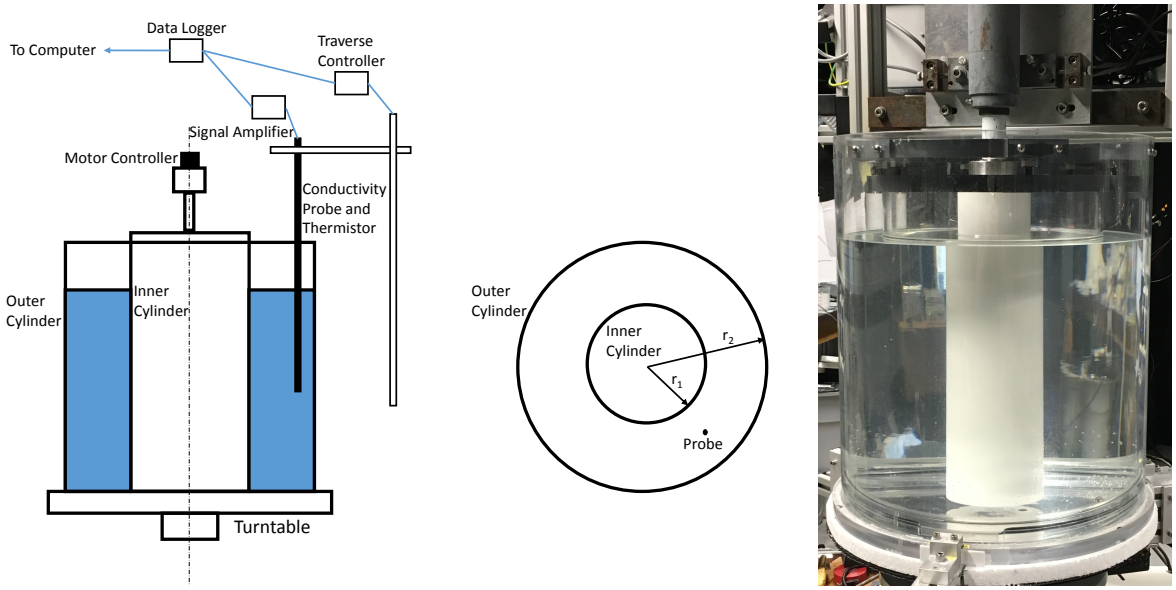


(a) (b)

Fig. 2.2 $(a)$ A schematic of the experimental apparatus; $(b)$ a photo of the apparatus.

For the experiments shown in this chapter, the outer cylinder has been kept stationary. The inner cylinder is also made of cast acrylic, and is painted white. Three inner cylinders of radii $R_1 = \{6, 10, 15\}$cm were available. The inner cylinder was connected via a shaft to a brushless DC motor, which was mounted overhead and was controlled by a computer. It could also be rotated at a range of different angular velocities from $0.1\,\mathrm{rad\,s^{-1}} < \Omega_i < 3\,\mathrm{rad\,s^{-1}}$. The error in the angular velocities of both the inner and outer cylinder is $<1\%$[1]. Figure 2.2 shows the schematic and a picture of the experimental apparatus. To note here the apparatus used by Oglethorpe (2014) could only run during the day time and had to be stopped in the evening, which disrupted the experiments. The present apparatus is capable of running at night as well which means with this apparatus we can perform a long experiment to study the flow behaviour throughout.

As mentioned before, the dimensions of our experimental apparatus and parameters at which experiments are conducted are similar to those used by Oglethorpe (2014), the Taylor number of the flow is $O(10^5) \times Ta_c$, where $Ta_c$ is the critical Taylor number. This is sufficiently high that the flow is far from the point of transition and is fully turbulent (Lewis & Swinney, 1999).

[1]This was checked by Dr. Jamie Partridge by putting a marker to the cylinder surface and recording the same using a high speed camera.

### 2.2.1 Stratified fluid in the tank

A pair of computer controlled peristaltic pumps are used to fill the annular region between the two concentric cylinders. Each pump is connected to a separate reservoir, one with a relatively lighter fluid ($\rho_1$) and the other with a denser fluid ($\rho_2$) respectively. Fluid in the reservoirs is left for a period of at least 24 hours to allow for air to escape, in order to minimize the bubble formation during the experiment, and also to ensure that the fluid in both the reservoirs is at a consistent temperature, almost equal to the ambient temperature of the laboratory. The output of the two pumps is connected to a long, thin tube with sponge fixed at the outlet of the tube, which helps to reduce the vertical momentum and thereby reduce mixing. For these two-layer stratification experiments, the bottom half of the annular region is first filled with the relatively lighter fluid and then the denser fluid is pumped slowly at the bottom of the lighter fluid layer using the tube. Although care is taken to ensure minimal mixing, nevertheless the interface thickness after filling is about $1-2$ cm, which is significantly larger than the few millimetres over which the interface would spread by molecular diffusion during the several hours of filling time. The two layers hence formed are of equal height and the total height of fluid in the tank is $42.0 \pm 0.5$ cm. A polystyrene lid is used at the top of the fluid surface (floating on the surface with a small gap near the inner cylinder ensuring no momentum transfer from the inner cylinder to the lid) to ensure that the fluid feels similar boundary conditions both at the top and the bottom.

### 2.2.2 Conductivity probe and Thermistor

A conductivity probe, mounted on a traverse is used to obtain density profiles in salt-stratified experiments. The traverse is fixed on a support frame above the cylinder. The variation of temperature throughout the day has an effect on the output of the conductivity probe, which could hinder the precise measurement of density and hence, the flux. In order to correct for the temperature variations, a thermistor is also mounted on the same traverse to have temperature profiles. The density or temperature profiles were measured across a large region, approximately $>80\%$ of the height $H$ of the fluid during experiment, over a period of O(10 s) which is quite small compared to time period of density evolution. Only the data from the downward motion of the conductivity probe or thermistor is used, since during the upward motion the data is affected by the presence of the probe's wake.

The thermistor and the conductivity probe both needed to be calibrated to have an accurate measure of the density of the fluid. Conductivity probes work on the principle that the resistance offered by the fluid to the flow of current is proportional to the number of ions present in that fluid. In our case, the fluid is the common salt (NaCl) solution. Salt when

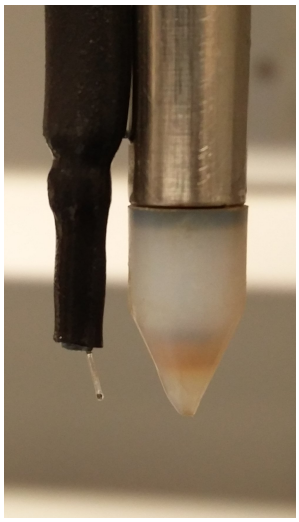

Fig. 2.3 A photograph of the tip of the conductivity probe (right) and the attached thermistor (left).

added to water dissociates into sodium and chloride ions, changing the resistance of the fluid as these ions are the current carriers. By measuring the resistance of the fluid, the probe could then be calibrated to have a measure of the salinity of the fluid, which in turn can tell us the density of the fluid. The probe consists of a long cylindrical conductive tube of diameter 10 mm with a conical tip at one end. The probe tip has a small hole, 0.3 mm in diameter, through which the ambient fluid whose density is to be measured enters the probe. There is a small conductive cylinder inside the tip, separated from the outer cylinder by an insulating material. As the fluid passes through the tip, a circuit is then constructed between the two cylinders. The resistance offered by the fluid in the circuit is the measure of the salinity of the fluid. The fluid at the tip is continuously replenished by continuously siphoning the fluid out through the head of the probe, to have a good response to a quick change in salinity. A pinch valve, which blocked the drain end of the probe tube when activated, is used to stop the fluid siphoning during the upward motion of the probe and during the period between measurements, to save the fluid from being removed when the measurement is not happening. The overall height of the fluid hence decreased by less than a couple of centimeters over a span of a few days, and it is small enough that it can be neglected. The probe tip is also required to be submerged in water for a while before using as it expands by absorbing water and hence also must be stored in water when not in use.

The conductivity probe was calibrated by fitting a curve through voltages recorded from many samples of known densities. The voltage data produced during the experiment was then mapped on to the fitted curve to get the density data. It was found that conductivity of salt water is temperature dependent and the temperature in the lab changes over time.

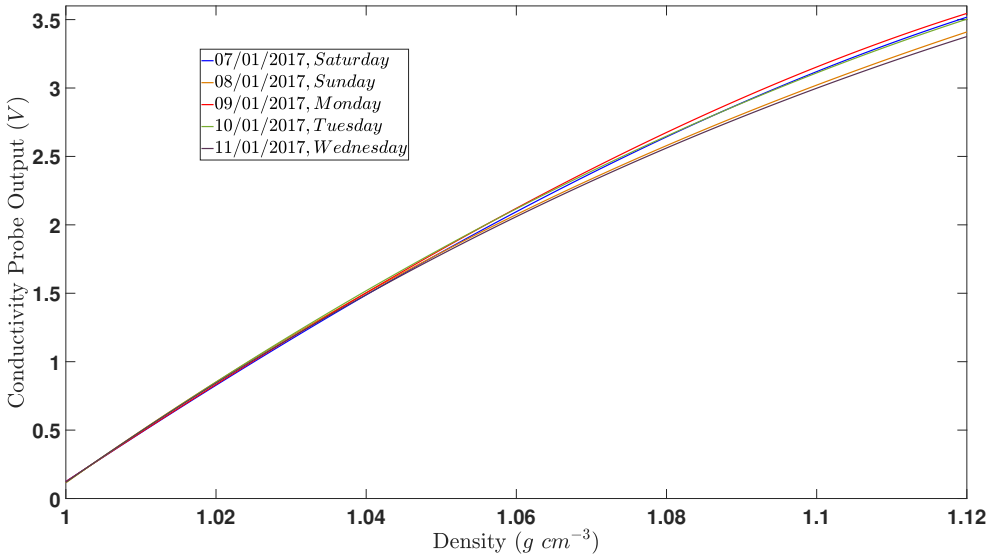


Fig. 2.4 Calibration curves showing probe voltages with respect to density of the fluid at 20°C. The curves are different for different days because of the change in temperature in the laboratory.

Figure 2.4 shows the calibration curves for the probe plotted for five different days in January 2017. Since the temperature in the lab keeps changing, the curves are different. As discussed earlier, we additionally attach a thermistor to the side of the probe, which can be seen in figure 2.3. The thermistor consists of a temperature sensitive semiconductor sensor whose resistance changes with the change in temperature.

The conductivity probe and the thermistor were then calibrated simultaneously. For a given salinity, we varied the temperature of the fluid and recorded the corresponding change in voltages in both the probe and the thermistor. To do this, we prepared a fluid solution of known density that was cooled to a low temperature ($\approx 5°$C). The thermistor was set to read between 0-10 V for a range of temperature, approximately between 15°C and 25°C, as the change in temperature in the laboratory was well within this range. Some of the cold fluid was then taken in a separate beaker and then inserted in a heat water bath to have the hot fluid ($\approx 40°$C) of the same salinity. In another beaker, both the hot and the cold fluids were mixed to have the fluid at a temperature approximately 24°C. The probe was inserted in this fluid and the measurements began. The cold fluid was slowly added to the beaker to lower its temperature, and another measurement was taken after stirring it with a spatula to ensure that it was at a homogeneous temperature. This process continued until the thermistor measured around 0 V. Hot fluid was then slowly added and measurements were taken as the temperature increased. This process was repeated for several different density fluid solutions.

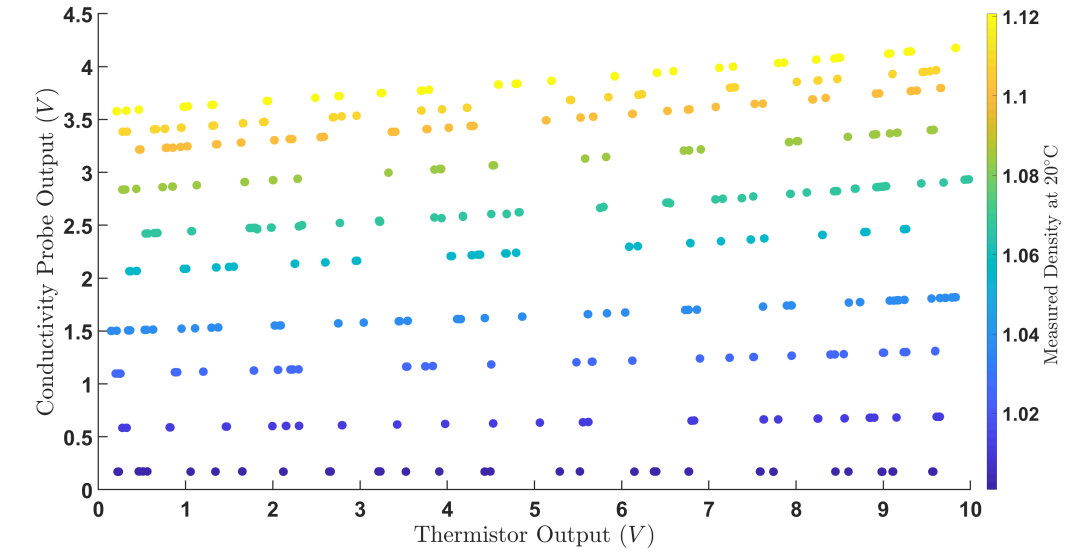


(a)

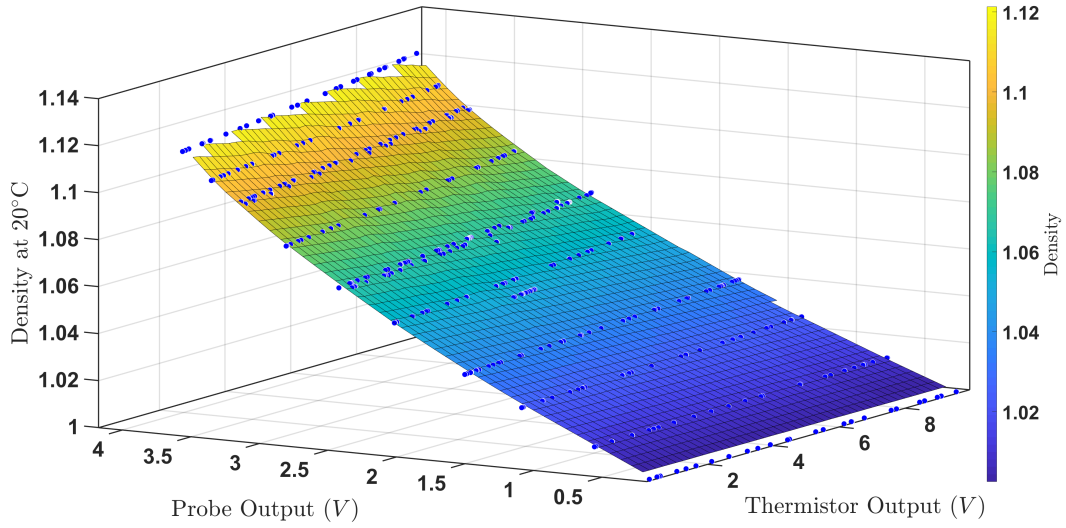


(b)

Fig. 2.5 Plot showing $(a)$ various conductivity probe voltage measurements vs thermistor voltage output in volts for different salinity samples and with varying temperature (colourbar shows the density of the respective sample at 15°C), and $(b)$ third order surface fit to the conductivity probe and the thermistor data, which is our calibration surface. Blue solid circles on the sheet are the same data points from $(a)$.

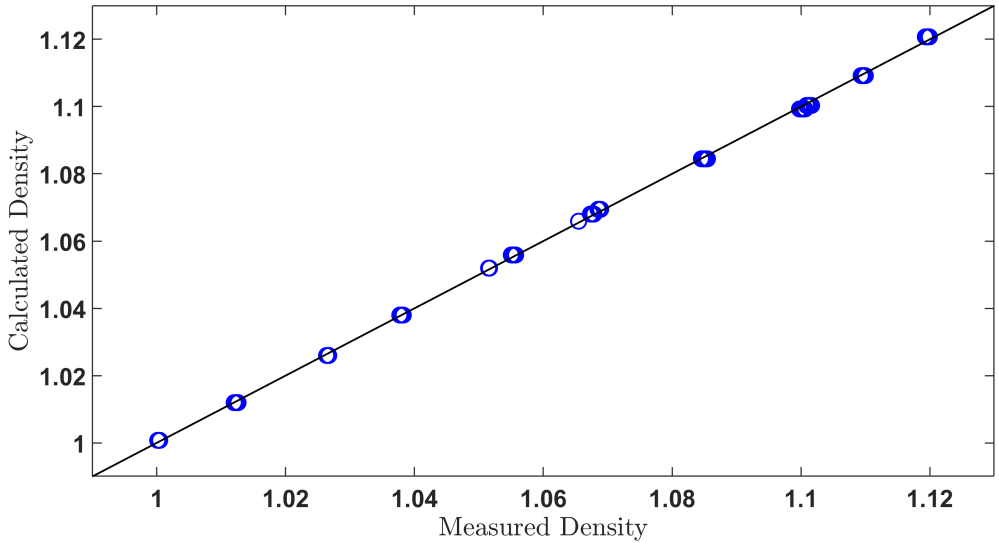


Fig. 2.6 Plot of the calculated vs measured density values. Standard deviation of the calculated values from the measured values is $3.44 \times 10^{-4}\,\mathrm{g\,cm^{-3}}$.

The recorded data can be seen in figure 2.5a. Probe voltage vs thermistor voltage is plotted and the colour represents the density of fluid at 20°C (measured using Anton Paar DMA 5000 density meter), which was our measure of the fluid salinity. A third order surface was fitted onto this data (figure 2.5b) which acts as our calibration surface. Now, once we get the probe and the thermistor voltages for the experiment, those values are then mapped on the calibration surface to get the density. In order to check for the accuracy of our fitted surface, we plot the computed density of each calibration point versus the measured density as shown in figure 2.6. A linear solid line fit represents a good agreement. The standard deviation of the computed density values from the measured values is $3.44 \times 10^{-4}\,\mathrm{g\,cm^{-3}}$, which is very similar to that seen by Olsthoorn (2017) for his calibration procedure. It is also worth noting here that the standard deviation in the recorded density data due to the electrical noise is $O(10^{-4}\,\mathrm{g\,cm^{-3}})$, which is similar to the standard deviation of the above computed density values, showing the consistency of our calibration procedure.

It is worth noting here that the flow in the experiments was fully turbulent, and the presence of the conductivity probe in the flow did not effect the turbulent properties of the flow. This was checked by Dr. Jamie Partridge[2] by performing different experiments, with probe inserted throughout the experiment and with probe inserted during the part of the experiments, and comparing the fluxes. The observed fluxes were consistent in both the cases.

[2]There experiments were performed without any help from the author.

## 2.3 Observations

To begin the experiment, the annular region is filled with two different density layers forming a stable stratification, as described in the previous section. The inner cylinder is then made to rotate which produces the centrifugally unstable flow and generates turbulence. The turbulence then scours the interface and makes it even sharper, which then stays at an approximately constant thickness throughout until near the end of the experiment (consistent with observations of Woods *et al.* (2010) and Oglethorpe (2014)). To note here that the comment about the interface thickness is based on observing the density profiles. However, in reality the interface structure is much more complex and will be discussed in detail in chapter 3. As the time progresses, the density of the upper layer increases while that in the lower layer decreases continuously. A typical evolution of density in a two-layer stratified Taylor-Couette experiment can be seen in figure 2.7a. Figure 2.7b shows some individual density profiles at different times over the span of an experiment. These profiles are at an equal time period apart (except from the last one), and the density of the fluid in each layer appears to change much faster at later times. This is also observed in figure 2.8 which shows the variation of density difference in the two layers over time. $\Delta\rho$ appears to decrease at a constant rate throughout most of the experiment and decreases much more rapidly at a later stage, which is consistent with Oglethorpe (2014). As the $\Delta\rho$ decreases below a critical value where stratification is no longer able to suppress the vertical motion of the fluid parcels, the interface overturns.

As the mixing progresses, the bulk Richardson number, $Ri_B$ (equation 2.4) decreases due to reduction in $\Delta\rho$. Oglethorpe (2014) defined the non-dimensional buoyancy flux as

$$\hat{F} = \frac{\Delta_R}{(\Omega R_1)^3} F. \tag{2.5}$$

The same scaling is used in the present study as well. Figure 2.9 shows the variation of observed non-dimensional flux (defined in equation 2.3) with $Ri_B$ for different Reynolds numbers, $Re$, plotted in comparison to the universal flux curve observed by Oglethorpe (2014). $\Delta\rho$ is calculated by taking the mean of the observed density in each of the layers which then is used to calculate $F$. The universal flux curve is obtained by digitising figure 2.6c from Oglethorpe (2014). The experiments shown are performed with the inner cylinder of radius, $R_i = 10\,\text{cm}$ and $15\,\text{cm}$. The cylinders are made to rotate with a different angular velocity for each separate experiment. An experiment is also performed by using the completely de-aerated fluid (achieved using a vacuum chamber) in order to make sure that there were no discrepancies in the flux measurements due to the bubble formation on the cylinder surfaces during the experiment. The flux curve produced using de-aerated fluid is exactly the same as

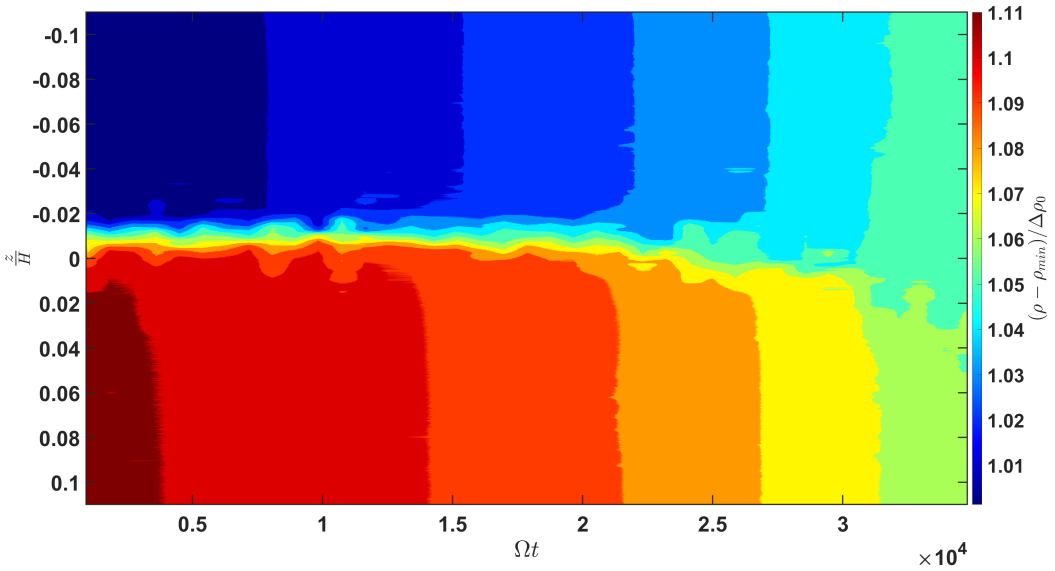


(a)

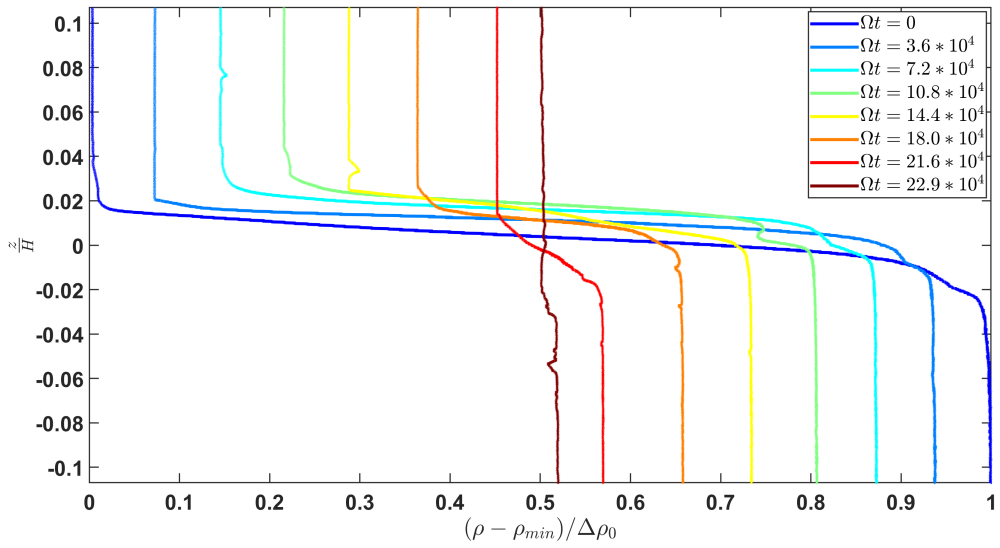


(b)

Fig. 2.7 $(a)$ Plot showing the evolution of density in a two-layer Taylor-Couette flow over time ($R_1 = 10\,\text{cm}, \Omega = 2\,\text{rad}\,\text{s}^{-1}, \Delta\rho_0 = 0.115\,\text{g}\,\text{cm}^{-3}$). $(b)$ Eight different density profiles from another similar two-layer stratified Taylor-Couette experiment with $\Omega = 1\,\text{rad}\,\text{s}^{-1}$, at different times throughout the span of the experiment. In these experiments, the conductivity probe was made to traverse 10 cm with interface approximately in the middle. $H = 42\,\text{cm}$.

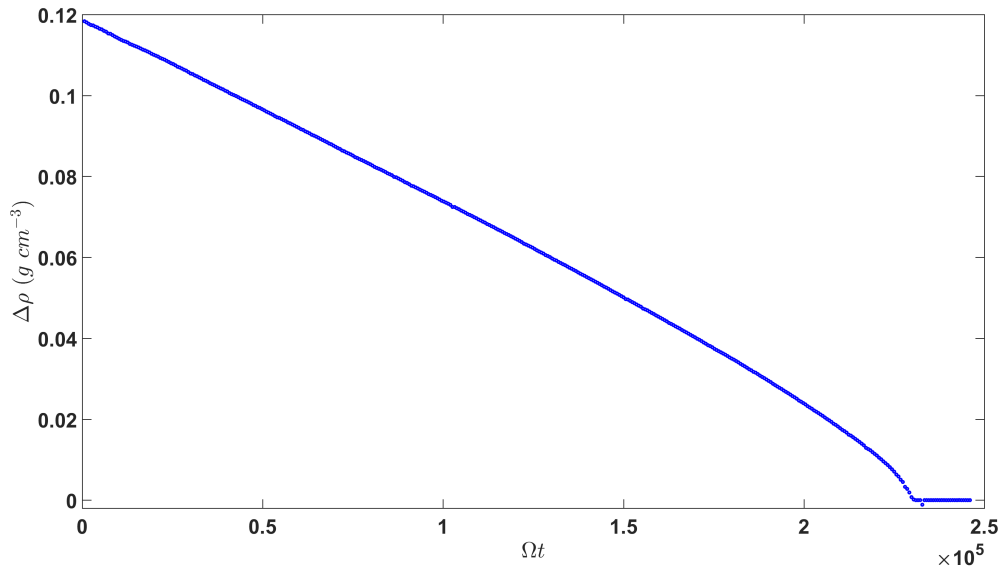


Fig. 2.8 Plot showing the evolution of $\Delta\rho$ over time.

in the other case. We find that the flux curves at high $Ri_B$ are consistent with the Oglethorpe (2014)'s universal flux curve. At high $Ri_B$, the flux is observed to be constant ('asymptotic regime'), until a critical $Ri_B$ where flux starts to increase with decreasing $Ri_B$ ('enhanced flux regime') to a maximum where the interface overturns and fluid mixes completely ('overturning regime', as described by Oglethorpe (2014)). The experiment at $\Omega = 2\,\mathrm{rad\,s^{-1}}$ ($Re = 28000$) produces the flux curve that is slightly different from the universal flux curve. We believe that this is because at that speed, the starting $Ri_B$ for $\Delta\rho_0$ used is already in the enhanced flux regime and the flow does not get much time to stabilise. To note, this also suggests that the interface reaching its steady state by initial scouring by the turbulent eddies is important. We believe that for $\Omega = 2\,\mathrm{rad\,s^{-1}}$ experiment, the interface was not able reach its steady state, which meant the entraining fluid parcels felt a different density gradient, and hence, a different flow behaviour. Also, the flux in the 'asymptotic regime' is a little higher than that in the universal flux curve, which could be because of these two reasons: $(a)$ the surface roughness of the cylinder surfaces used in our experiments is different from those used by Oglethorpe (2014), as the roughness increases the flux transport (refer to chapter 4 of Oglethorpe (2014)), or $(b)$ it is the inherent scatter in the flow because of the non-linear properties of turbulence (consistent with figure 2.6c of Oglethorpe (2014)).

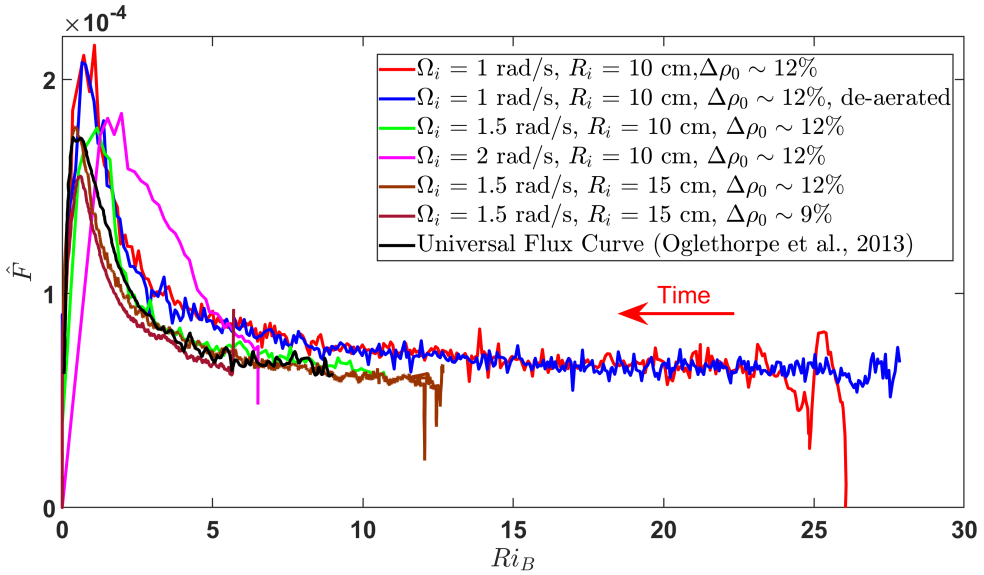


Fig. 2.9 Non-dimensional flux, $\hat{F}$ variation with bulk Richardson number, $Ri_B$ at different rotation speeds. Other parameters for the experiments are $R_i = 10\,\text{cm}$ and $\Delta\rho_0 \sim 0.12\,\text{g cm}^{-3}$. Black line is the universal flux curve given by Oglethorpe (2014).

## 2.4 Analysis

We analyse the flux observations described above to find how the buoyancy flux behaves with changing $Ri_B$ by analysing various contributors to the flux.

### 2.4.1 Different contributors to the total flux

Oglethorpe (2014) assumed the Boussinesq approximation and came up with the scaling for $F$ and $Ri_B$ (refer to equation 2.4 and 2.5). We assume the Boussinesq approximation as well and use the same scaling to calculate $F$ and $Ri_B$. Figure 2.9 shows the flux curves obtained for various different experiments. We use the data from the experiment that is performed with de-aerated fluid to look into different contributors to the observed flux. It was executed at $Re = 14000$ ($\Omega_i = 1\,\text{rad/s}$ and $R_1 = 10\,\text{cm}$) with a starting density difference, $\Delta\rho_0 \sim 0.12\,\text{g cm}^{-3}$. To give an idea of the duration of the experiments, the above mentioned experiment took three days to completely mix. Fresh water and Sodium Chloride solution in water were used as the two fluids. Note that the high $\Delta\rho_0$ was chosen in order to have a high enough starting $Ri_B$. We are aware that the $\Delta\rho_0 \sim 12\%$ means that the Boussinesq approximation might not be valid. As the experiment progresses, $\Delta\rho$ decreases, ensuring that Boussinesq approximation will be valid eventually.

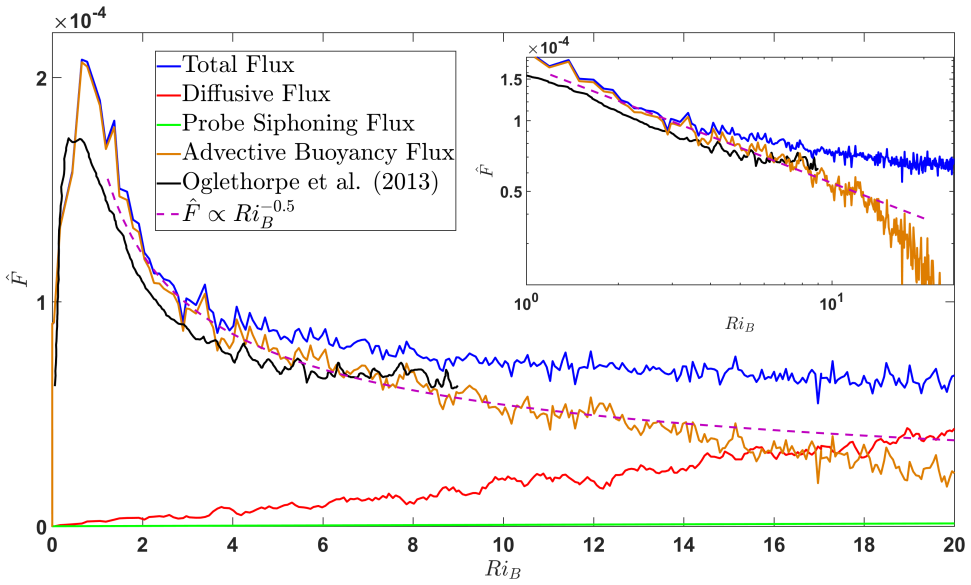


Fig. 2.10 Plot showing different contributors to the total flux observed in a two-layer stratified Taylor-Couette experiment performed at $Re = 14000$ with $\Delta\rho_0 \sim 0.12\,\mathrm{g\,cm^{-3}}$ (same as blue curve in figure 2.9). The dashed pink curve is the $\hat{F} \propto Ri_B^{-0.5}$ curve, with a very good agreement with the buoyancy flux curve in the range $1.5 \leq Ri_B \leq 15$. The inset plot shows the same buoyancy flux curve and the universal flux curve by Oglethorpe (2014) drawn on a log-log plot.

Over time, the density of the upper layer increases while that in the lower layer decreases, which means the salt is being transferred from the bottom layer to the upper layer across the interface. This flux across the interface (refer to equation (1.5)) is the sum of advection flux (buoyancy flux), diffusion flux across the sharp density gradient at the interface, and some additional flux which is caused when the fluid from each of the layers is removed due to conductivity probe siphoning. Hence, the final rate of change of mass in each of the layers can be written as

$$S\frac{H}{2}\frac{d\rho_u}{dt} = S\,\dot{m}_e + S\kappa\frac{d\rho}{dz}\bigg|_{interface} - Q_p\rho_u \tag{2.6}$$

$$S\frac{H}{2}\frac{d\rho_l}{dt} = -S\,\dot{m}_e - S\kappa\frac{d\rho}{dz}\bigg|_{interface} - Q_p\rho_l \tag{2.7}$$

where $S = \pi(R_2^2 - R_1^2)$ is the surface area in the annular gap, $\rho_u$ and $\rho_l$ are the densities of the upper (lighter) and lower (heavier) layers respectively, $\dot{m}_e = \Delta\rho\ u_e$ is the rate of mass

transport due to entrainment velocity ($u_e$), $\kappa$ is the coefficient of diffusion of Sodium Chloride (NaCl) solution, $\left.\frac{d\rho}{dz}\right|_{interface}$ is the density gradient at the interface, and $Q_p$ is the volumetric rate of fluid being siphoned out of the conductivity probe.

Now subtracting equation 2.6 from equation 2.7 gives

$$S\frac{H}{2}\frac{d(\Delta\rho)}{dt} = -2S\,\dot{m}_e - 2S\kappa\left.\frac{d\rho}{dz}\right|_{interface} - Q_p\Delta\rho$$

The mass transport due to buoyancy flux can be obtained from the above equation and can be written as

$$\dot{m}_e = -\frac{H}{4}\frac{d(\Delta\rho)}{dt} - \kappa\left.\frac{d\rho}{dz}\right|_{interface} - \frac{1}{2}\frac{Q_p}{S}\Delta\rho \tag{2.8}$$

The total buoyancy flux, $F_B$ can be calculated using above as $F_B = \frac{g}{\rho_0}\dot{m}_e$. It gives

$$F_B = \underbrace{-\frac{H}{4}\frac{g}{\rho_0}\frac{d(\Delta\rho)}{dt}}_{\text{Total flux observed in the experiment}} \underbrace{-\kappa\frac{g}{\rho_0}\left.\frac{d\rho}{dz}\right|_{interface}}_{\text{Diffusive flux}} - \underbrace{\frac{1}{2}\frac{g}{\rho_0}\frac{Q_p}{S}\Delta\rho}_{\text{Flux due to probe siphoning}} \tag{2.9}$$

Hence, in order to calculate the buoyancy flux, the diffusive flux and the flux due to probe siphoning needs to be subtracted from the total flux observed in the experiment. The total volume of siphoned fluid was measured at the end of the experiment which gave us an idea of $Q_p$, which in turn was used to calculate the flux due to probe siphoning. For this calculation, it is assumed that same volume of fluid was siphoned from each of the layers i.e. the interface was exactly in the middle of the traverse, which looking at the density profiles in figure 2.7b is a fair assumption. $\left.\frac{d\rho}{dz}\right|_{interface}$ is calculated by finding the middle of the interface (represented by green solid circle in figure 2.11) for the empirical density profiles and evaluating the gradient at that point. The gradient is calculated by assuming linear density profile for 200 recorded density points around the middle of the interface (density was recorded at a sampling rate of 1024 samples per second while the probe was traversing at a speed of $0.01\,\mathrm{m\,s^{-1}}$), end points being represented by red diamonds in figure 2.11. Looking at figure 2.11, it can be seen that the assumption of linear density profile at the middle of the interface is reasonable. Further, the coefficient of diffusion for NaCl used in

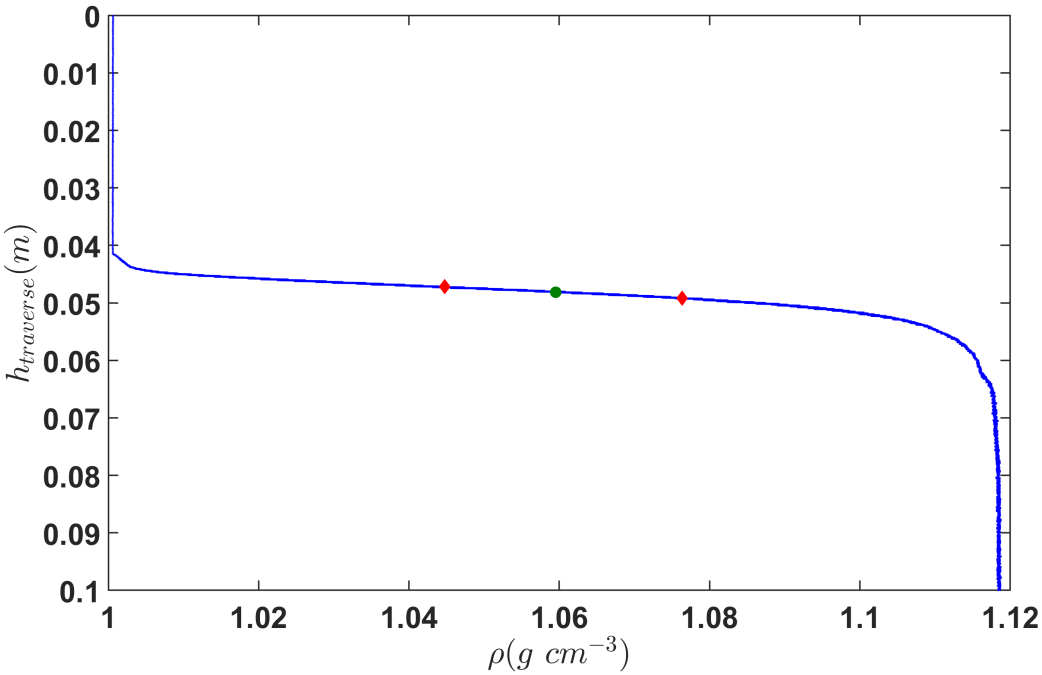


Fig. 2.11 Plot showing a typical recorded density profile along the probe traverse. Green solid circle shows the middle of the interface with the density as the mean of the density in the two layers. The density profile around this point was assumed to be linear and the gradient was assumed to be the linear gradient between the two red diamonds. Note: The density was recorded during the downward motion of the probe.

calculation of diffusive flux is $\kappa = 1.5 \times 10^{-9}\,\mathrm{m^2\,s^{-1}}$ (Chang & Myerson, 1985). Fluxes are non-dimensionalised using the scaling mentioned in equation 2.5.

Oglethorpe (2014) assumed that the flux due to diffusion is negligible and did not consider the flux due to probe siphoning. Figure 2.10 shows the different components of total flux plotted individually for the above mentioned experiment against $Ri_B$. The blue curve is the total flux observed in the experiment. The red and the green curves represent the diffusive flux and the flux due to probe siphoning respectively. The yellow curve is the calculated buoyancy flux curve. The flux from siphoned fluid is negligible and can be ignored, but the flux due to diffusion is significant, especially at high $Ri_B$ and can not be neglected. The observed 'asymptotic regime' for buoyancy flux by Oglethorpe (2014) was a consequence of assuming the diffusive flux to be negligible. The actual buoyancy flux monotonically increases with decreasing $Ri_B$, with higher rate as the $Ri_B$ decreases, until a critical $Ri_B$ where the interface overturns and fluid mixes completely.

Further, the Phillips mechanism suggests that if the flux of density decreases as the vertical density gradient increases, then any perturbation causing an increase in the gradient

will be amplified. Since the buoyancy flux curve in the STC now satisfies this condition, it suggests that the layering process by this mechanism is preferred in an initially linearly STC flow.

### 2.4.2 Flux power law

Oglethorpe (2014) computed the best-fit power law for her flux data and found that for $1 < Ri_B < 4$, $\hat{F} \propto Ri_B^{-0.51}$, which is consistent with the previous studies on stratified turbulence (Deardorff & Yoon, 1984; Turner, 1968; Zellouf *et al.*, 2005). She also found that for $2.75 < Ri_B < 7.5$, $\hat{F} \propto Ri_B^{-0.31}$. She concluded that it was the change in nature of the fluid flow at $Ri_B = 4$, from enhanced flux to constant flux with increasing $Ri_B$, resulting in different best-fit power law for different $Ri_B$ ranges. She performed this calculation on the total flux observed in the experiment and not the buoyancy flux, as she had assumed diffusive flux to be negligible. We, however, now know that the total flux curve is not a correct representation of the buoyancy flux.

The dashed pink curve in figure 2.10 represents $\hat{F} \sim Ri_B^{-0.5}$. The inset plot in figure 2.10 shows the buoyancy flux curve and Oglethorpe's universal flux curve from the main plot on a log-log plot. The dashed pink curve looks to be in a good agreement with the calculated buoyancy flux curve until $Ri_B \approx 15$, which can also be confirmed on the inset plot. We believe that at higher $Ri_B$, our Boussinesq approximation does not stay valid, and it is the reason for non-agreement. The flux curve by Oglethorpe (2014) also agrees well with the dashed pink curve until $Ri_B = 5$ as diffusive flux is relatively not significant in this region. Beyond $Ri_B = 5$, the diffusive flux being significant, her flux curve appears to deviate from $\hat{F} \sim Ri_B^{-0.5}$ curve.

The buoyancy flux curve being proportional to $Ri_B^{-0.5}$ gives that the entrainment coefficient $E \propto Ri_B^{-3/2}$, which is consistent with the observations of Turner (1968) and Linden (1980) for their salt stratification experiments. This suggests that the mixing behaviour is consistent in grid mixing and in the STC.

### 2.4.3 Flux at very high $Ri_B$

As discussed in section 2.1, Guyez *et al.* (2007) in their STC experiments observed a very different flow behaviour from the observations of Woods *et al.* (2010) and Oglethorpe (2014). They used laser induced fluorescence technique to observe the evolution of a scalar dye in the layers, which gave them the measurement of flux. They found that as the $Ri_B$ increases from zero, the flux increases to a maximum, then starts to decrease and then later increase again. In our experiments discussed so far, we have not observed the increase of flux at high

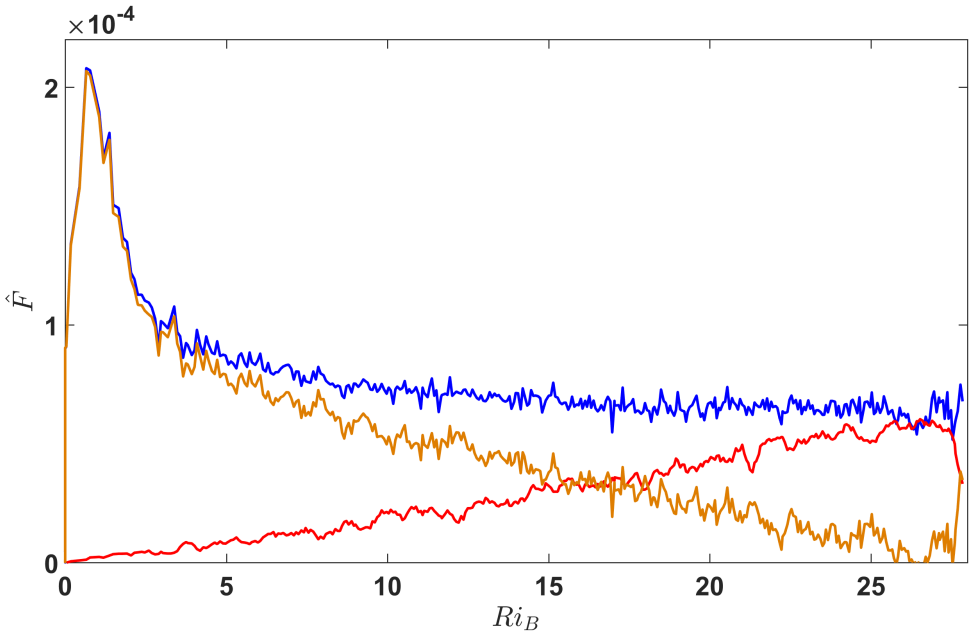


Fig. 2.12 Plot showing the same flux curve as in figure 2.10 with higher limits on $Ri_B$ axis. The blue curve is the observed flux total flux, the red curve is the diffusion flux and the yellow curve is the buoyancy flux calculated after subtracting the diffusion flux from the total flux.

$Ri_B$. To note here that, in Guyez *et al.*'s experiment, the starting $Ri_B \approx 70$ which is much greater than the $Ri_B$ in our experiments.

However, the experiment performed by us which is analysed in figure 2.10 was started at $Ri_B \approx 28$. Figure 2.12 shows the same plot that is shown in figure 2.10 over the complete range of calculated $Ri_B$. The blue curve is the total observed flux, the red curve is the diffusion flux and the yellow curve is the buoyancy flux calculated after subtracting diffusion flux from total flux. It can be seen that around $Ri_B \approx 27$, almost all of the observed flux is because of diffusion, and the total buoyancy flux becomes negligible. Extrapolating the observed plot at even high $Ri_B$ would mean that the total flux starts to increase owing to increased diffusion. Since Guyez *et al.* (2007) were measuring flux through observing a diffusing scalar, they were actually measuring the total flux and not the buoyancy flux. Their increase in buoyancy flux observed at higher $Ri_B$ was as a result of diffusion dominating the flow. The diffusion dominated STC flows are discussed in more detail in chapter 6.

## 2.5 Discussion

In this chapter, we have looked into the flux across the interface in a two-layer STC experiment at a significantly higher $Ri_B$ than that by Oglethorpe (2014). We observe that the rate of

change in density difference, $\Delta\rho$ across the interface is constant during most of the experiment. However, at low $\Delta\rho$, the density difference starts to reduce comparatively much rapidly. This is also seen in the flux curves for various different experiments, performed using inner cylinders of radii $R_1 = \{10, 15\}$cm and rotating those at different speeds, where the total observed flux across the interface is approximately constant at high $Ri_B$. Then after a critical $Ri_N$, the flux starts to increase rapidly with reducing $Ri_B$ until a maximum where the interface overturns and the fluid is fully mixed. The total flux curves look consistent with Oglethorpe's universal flux curve.

We, then break down the different components of the observed total flux, which primarily are the buoyancy flux and the diffusive flux (refer to figure 2.10). We observe that the flux due to diffusion is a significant contributor to the total flux, especially at high $Ri_B$, which was ignored by Oglethorpe (2014). We then calculate the buoyancy flux after subtracting the diffusion flux from the total flux and find that it is a monotonically decreasing function of $Ri_B$. Analysing further, we find that the buoyancy flux is proportional to $Ri_B^{-0.5}$ in the region were the Boussinesq approximation is valid. Hence, the entrainment coefficient for the flow goes as

$$E \sim Ri_B^{-3/2}, \tag{2.10}$$

which is consistent with the observations of Turner (1968) for their salt stratification grid-mixing experiments. This suggests a consistency in entrainment behaviour for STC and stratified grid-mixing experiments.

It is worth noting here that Turner (1968) performed grid mixing experiments and found $E \propto Ri_B^{-3/2}$ in their salt stratification experiments. Later, Zellouf *et al.* (2005) performed similar experiments and found the $E \propto Ri_B^{-1}$. The maximum density difference $(\Delta\rho/\rho_0)$ in the experiments by Turner (1968) was about $5 \times 10^3$, whereas that in the experiments by Zellouf *et al.* (2005) was about three times larger, at $1.4 \times 10^2$. The stirring frequencies were similar in both the experiments. Zellouf *et al.* (2005) found the flux by calculating the rate of change of salinity in each of the layers, which meant they were calculating total flux and not only the buoyancy flux. Since the initial density difference in experiments of Zellouf *et al.* (2005) was higher than that in experiments of Turner (1968), it means the diffusion was also more prominent for Zellouf *et al.*. It is probable that if the diffusion is removed from the flux measurements of Zellouf *et al.* (2005), they will observe a similar flux to Turner (1968) and in turn, a similar entrainment coefficient.

Moreover, since we find that the buoyancy flux is a monotonically decreasing function of $Ri_B$ (other than for $Ri_B$ in the 'overturning regime'), it satisfies the pre-requisite for 'Phillips mechanism'. Now any perturbation that causes the increase in density gradient will be amplified, which can lead to layer formation in a linearly stratified flow. This suggests that

the layer formation by the 'Phillips mechanism' is preferred in an initially linearly stratified STC flow.

Lastly, we look at the flux at very high $Ri_B$. As seen in figure 2.12, if we continue to increase $Ri_B$, the diffusion becomes dominant flux contributor. If $Ri_B$ is increased further, the total flux observed would start to increase due to enhanced diffusion across the interface, which would be consistent with observations of Guyez *et al.* (2007).

# Chapter 3

# Mixing Instability

## 3.1 Introduction

In this chapter, we explore in detail the mixing mechanism resulting in a buoyancy flux across the density interface in a stratified Taylor Couette flow.

Oglethorpe (2014) observed that for a linearly stratified turbulent Taylor-Couette flow, the flow spontaneously forms layers, with each layer well-mixed and separated by sharp interfaces. She found that the height of each of the well-mixed layers, $h_l$ is scaled as,

$$h_l \sim \frac{U_H}{N_0} + c \tag{3.1}$$

where $U_H = \sqrt{\Delta_R R_1}\Omega$ and $N_0 = \sqrt{-\frac{g}{\rho_0}\frac{\partial \rho}{\partial z}}$ are the horizontal velocity scale and buoyancy frequency respectively, and c is a constant. This was consistent with previous studies on vertical bars/grid generated stratified turbulence (Holford & Linden, 1999; Park *et al.*, 1994; Ruddick *et al.*, 1989). These studies concluded that the layer formation was due to the 'Phillips mechanism' (figure 1.3). Recent progresses with stratified Taylor-Couette (STC) flow, as discussed in chapter 2, also concludes that 'Phillips mechanism' is the most likely mechanism for layer formation for STC.

Oglethorpe (2014) also looked into flux across each of the, hence-formed, interfaces. In addition, she also performed the same for a two-layer STC, and found the non-dimensional flux across the interface was exactly the same as that observed for the linear STC (figure 1.4), which meant that the mixing mechanism is the same in both cases. She found that with reducing $Ri_B$, the flux stayed constant at high $Ri_B$, while at lower $Ri_B$ it starts to increase till a maximum where the interfaces overturn and the flux reduces to zero, which was consistent for the two-layer and the initially linearly STC case.

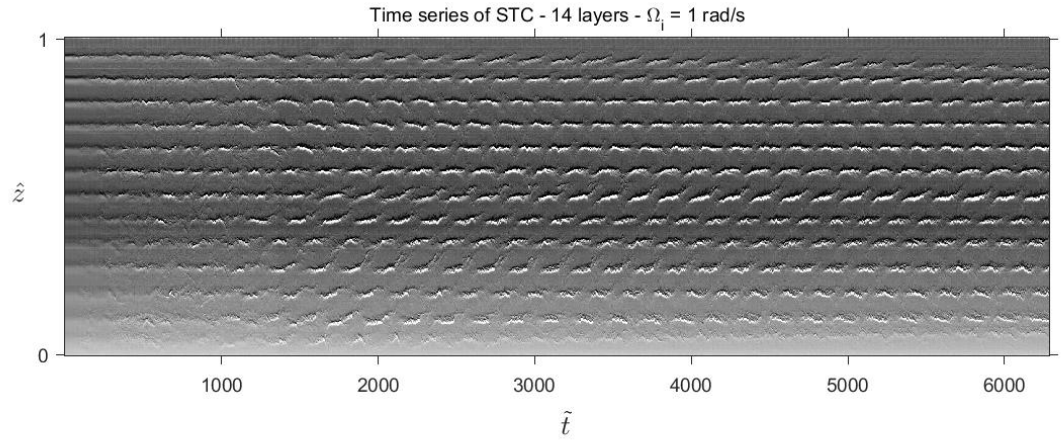


Fig. 3.1 Plot showing evolution of density gradients in a initially linearly stratified Taylor-Couette experiment, along one vertical line over time. Figure courtesy: Dr. Jamie Partridge[1].

However, Oglethorpe (2014), in her work, had looked into mixing properties for the two layer case only. She performed experiments on two-layer STC at various different starting density differences across the interface and with varying height of the fluid in the tank (both layers across the interface were always of equal height). She used the shadowgraph technique to visualise the interface, both horizontally (from the side of the tank) and from the top. A time series of a vertical line from one of her shadowgraph experiments is shown in figure 1.5. A periodic mixing mechanism is observed at the interface. She found, analysing all her empirical data, that the appropriate scaling for the time period ($T$) of this instability goes as

$$T = C\sqrt{\frac{\Delta_R}{R_1}}\frac{2\pi}{\Omega} \tag{3.2}$$

where $C = 4.82$ (or 3.98) for smooth (or rough) inner cylinders. This observed time period was independent of the density difference across the interface, $\Delta\rho$ or the height of fluid in the tank, $H$. Further analysing the images from her shadowgraph experiments with the camera looking from the top, she also found that this periodic coherent structure, associated with mixing across the interface, travels around the annulus. She hypothesised that in the high shear region in the boundary layer of the inner cylinder, the small-scale turbulent eddies mix the fluid around the interface. This results in formation of a region of mixed fluid that grows over time. The mixed fluid parcels then moves outward and around into the annulus in a form of an intrusive gravity current on the interface. These parcels are then entrained by the period blob in the annulus. The increase in the amplitude of the blob by entraining parcels of mixed fluid is balanced by its radial transport outwards. This mixed fluid from the blob is then homogenised in each of the layers via the large scale turbulent eddies in the layers.

The periodic mixing instability is also observed on the interfaces formed in an initially linearly stratified STC. Figure 3.1 shows a vertical line from the shadowgraph experiment performed with an initially linear stratification [1], with time. The observed period on the interfaces is exactly the same as that for its two-layer counterpart. It is also seen in figure 3.1 that the instability on every adjacent interface is out of phase while being in complete phase with that on every alternate interface, which tells us that the interfaces are coupled. Another experiment was performed to track the instability completely around the annulus using mirrors and it was observed that this instability was always azimuthal mode = 1 [2]. Leclercq *et al.* (2016*b*) performed a direct numerical simulation (DNS) of the linearly stratified STC. They suggested that the interfaces are the result of interactions of two helical modes of opposite handedness. In their simulations, they were able to recover the observed layer height by Oglethorpe (2014) and apparently explain the observed coupling between interfaces, but their simulation always gave the azimuthal wavenumber greater than 1 unlike that observed in the laboratory experiments.

We look into the structure of the periodic flow pattern at the interface in this chapter, which will give us further information about the dominant mixing mechanism. This can then give insights into the non-linear patterns observed on the flux curve and help understand the origin of this instability. We use quantitative techniques like laser induced fluorescence (LIF) and particle image velocimetery (PIV) to study the structure and the results are explained in this chapter.

## 3.2 Experiment

The experiments shown in this chapter uses the same Taylor-Couette apparatus as discussed in section 2.2. The inner cylinder of radius, $R_1 = 10\,\text{cm}$ is used. It was painted matte back in order to have minimal reflections of the laser light off its surface. For experiments using the conductivity probe, fresh water and common salt (NaCl) solution in water are used to produce the stratification. For PIV and LIF experiments, sodium chloride (NaCl) solution in water and sodium nitrate ($NaNO_3$) solution in water is used (explained in detail in a subsequent section). The tank is filled as discussed in section 2.2.1. The conductivity probe is also calibrated as before (refer to section 2.2.2). An acrylic lid attached to the outer cylinder is used on the free surface to ensure symmetry in the boundary conditions, and for experiments

[1] This experiment was performed by Dr. Jamie Partridge, who is a postdoctoral fellow in the GK Batchelor laboratory at DAMTP, University of Cambridge. It was done before had I joined the laboratory.

[2] This experiment was also performed by Dr. Jamie Partridge.

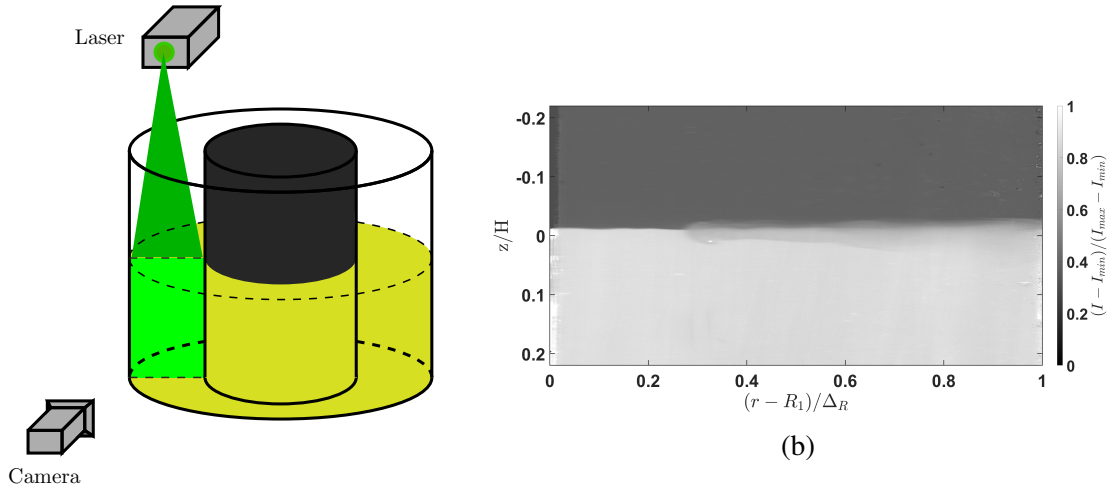


(a) (b)

Fig. 3.2 $(a)$ A schematic of the apparatus for LIF experiment. $(b)$ A typical recorded image from the LIF experiment.

with horizontal laser sheet at the interface, where camera is mounted at the top of the tank, to look through at the fluid flow.

### 3.2.1 Laser Induced Fluorescence (LIF)

LIF is a technique that is used to quantify the scalar field in the flow. The plane of measurement is illuminated by a laser sheet produced by using a set of optics in the path of a laser beam. The laser used for our experiments was either a Litron Nano dual pulsed Nd:YAG laser, producing 532 nm wavelength pulses of 50 mJ at 100 Hz from each laser, or a continuous line laser. The laser sheet is approximately 1 mm thick. A fluorescent dye is added to the fluid and the laser sheet is made to pass through it. The dye absorbs the energy at some range of wavelengths and emits light at a different range. For our experiments, Rhodamine 6G is used in one of the layers, which has the absorption maximum of 530 nm that is very close to wavelength of the incident laser and its emission range is 555 nm to 585 nm with a maximum at 566 nm (Clark, 2011). A filter is used in front of the camera lens that blocks the wavelength corresponding to the incident beam, which means that the intensity of light from any point reaching the camera is then proportional to the concentration of the dye at that point, which in turn is used in quantifying the scalar field at that point in time. This is useful in studying the evolution of the interface. The camera used is a Dalsa Falcon2 4MP camera. For the experiments with a vertical laser sheet, the camera lens was used with a scheimpflug adapter in order to correct for the variation in refractive index due to the curvature of the

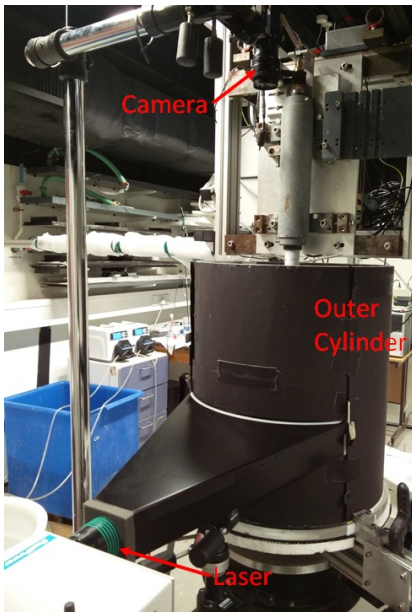


(a)

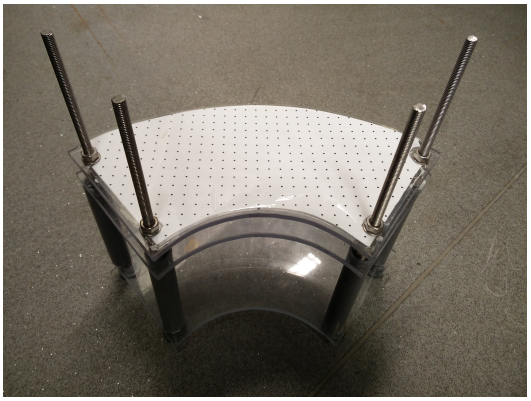

(b)

Fig. 3.3 $(a)$ Picture of the actual setup used for PIV, with a horizontal laser sheet at the interface. The outer cylinder was wrapped around with black card to stop reflections of laser light off surfaces from coming out. $(b)$ Picture of the calibration grid fixed to the stand. Each point on this calibration grid was exactly 10 mm apart from its neighbouring points in both directions.

outer cylinder. A schematic and a typical image from the experiment are shown in figure 3.2. Note that the images are recorded in grayscale.

### 3.2.2 Particle Image Velocimetery (PIV)

PIV is an experimental technique that is used to obtain the velocity field through analysing the images of the flow field. The flow is seeded with small tracer particles ($\approx 20\,\mu$m) with low Stokes number (which is the ratio of the relaxation time scale of the particle suspended in the flow to the characteristic time scale of the flow), such that these particles cause negligible disturbance to the flow and follow the flow. A laser sheet, produced as explained in the previous section, is passed through the flow containing tracer particles. The particles scatter the incident light and a camera is used to record the flow. The recorded image is broken into a number of small regions ('interrogation windows') and cross correlating the intensities of scattered light for the same window in two respective images gives us the average distance travelled by particles in that window. Now, knowing the time difference between different frames, the velocity field is calculated. A detailed explanation of the PIV technique is given in Prasad (2000). All the PIV analysis done for this PhD work is done

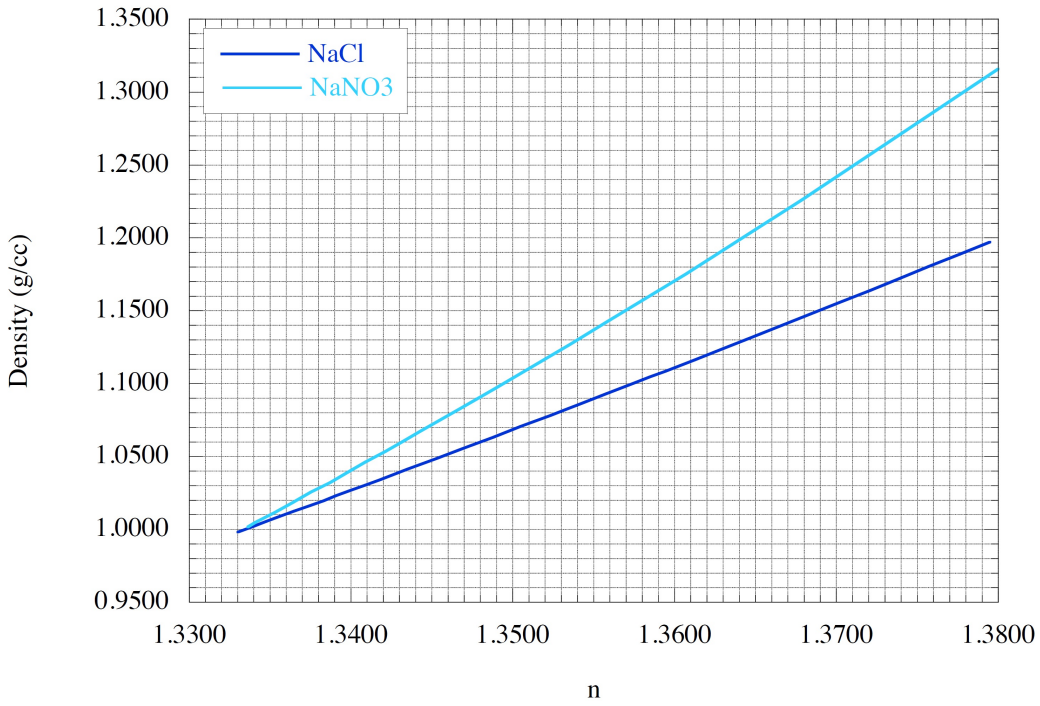


Fig. 3.4 Plot showing variation of refractive index (n) with density of both NaCl and $NaNO_3$ solutions. Figure courtesy: Dr. Mark Hallworth, Senior Technical Officer, DAMTP, University of Cambridge.

using DigiFlow$^{tm}$ (Dalziel Researchers Partners), which is a software developed by Prof. Stuart Dalziel (DAMTP, University of Cambridge). For our experiments, the camera is made to record at 100 fps synchronised with the laser. During experiments with simultaneous LIF and PIV, a filter is used in front of the PIV camera to block spurious light from dye fluorescence. The outer cylinder is covered with black card sheet on the outside, with a slit to allow the laser sheet to pass through. A black card is also placed on the top with a region taken out for the camera to view the flow field. This is done in order to ensure, alongside safety of the laboratory users, that there is no leakage of outside light, allowing a better contrast for camera viewing. An actual picture of the setup used can be seen in figure 3.3a. Figure 3.3b shows the picture of the stand with a calibration grid (with a dotted pattern of exact known dimensions on it). The height of the stand could be adjusted to vary the height of the laser sheet.

### 3.2.3 Refractive Index matching

For the salt stratified experiments, the stratification is created by adding common salt (sodium chloride, NaCl) to fresh water. The common salt, on addition to water, changes its optical

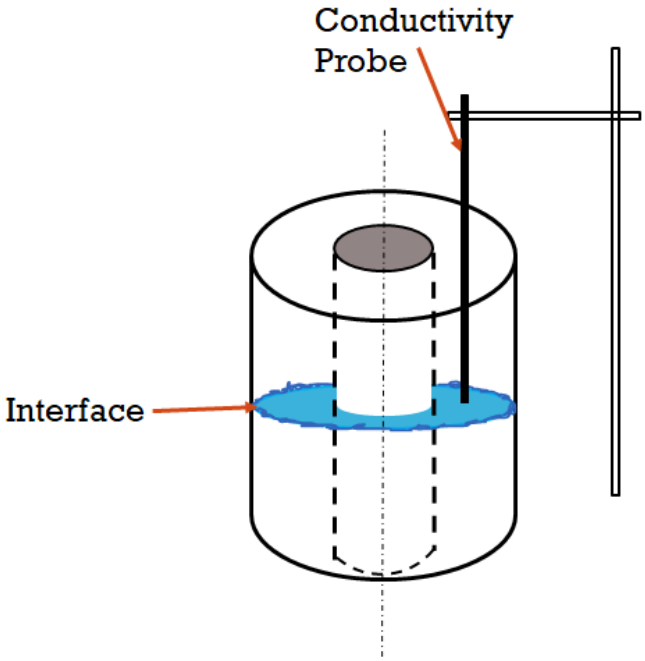


Fig. 3.5 Schematic of two-layer STC experiment with probe fixed at the interface.

density and hence the refractive index of the fluid changes. This means that a light ray will now follow a different deflected path than if it was just fresh water. During the PIV or LIF measurements, the camera will now see some blurred regions due to some refractive index variations, which in turn will give spurious velocity or scalar field data respectively. In order to minimize the effect of refractive index variation across a stratified layer, we use a solution of sodium nitrate ($NaNO_3$) in water. Sodium nitrate is a good choice as it is cheaply available and its solution has similar diffusivity to that to sodium chloride solution (Olsthoorn, 2017). The refractive index of sodium nitrates solution scales differently with concentration compared to that for a sodium chloride solution, as can be seen in figure 3.4. It can also be seen that for different values of refractive index, the difference in density of the two solutions is also different. We exploit this phenomenon to produce stratified layers of different densities, but having the same refractive index. Before the start of an experiment, the refractive indices were checked using a hand held refractometer (using a hand-held white light with a green film in front such that it was similar to the light of the laser) and appropriate changes to concentration of each of the solutions is made to ensure a refractive index match.

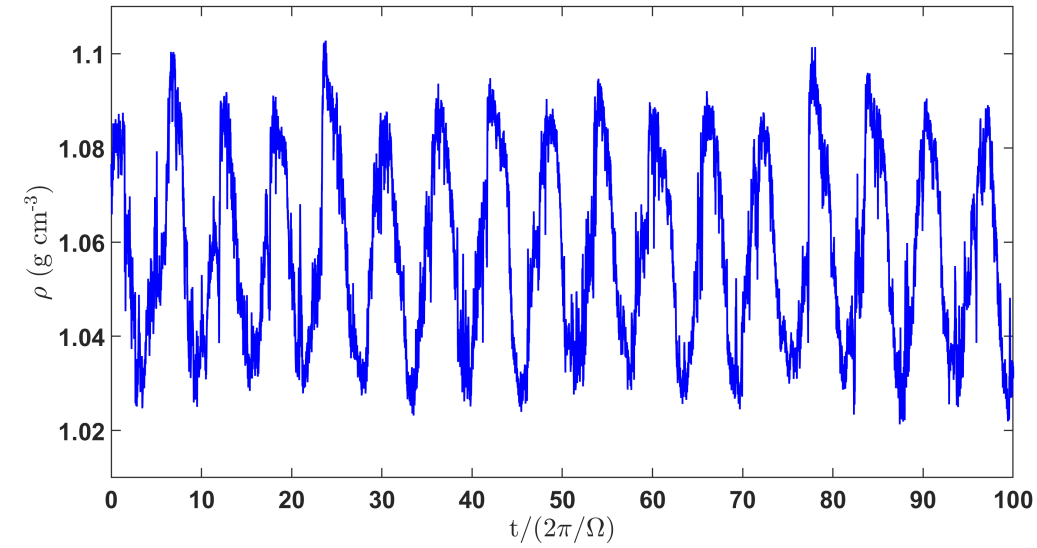


(a)

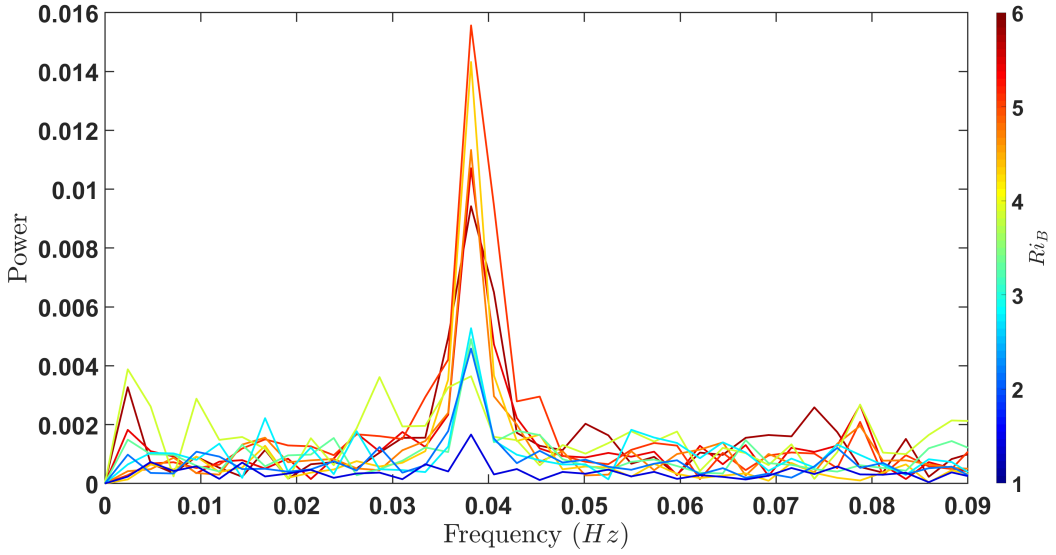


(b)

Fig. 3.6 $(a)$ Plot showing recorded density data from a two-layer stratified Taylor-Couette flow experiment, with the conductivity probe being kept fixed at the interface. $(b)$ Plot showing the frequency spectrum from fast Fourier transform on the various density data-sets. Each curve is a spectrum of a separate 100 rotation period density data-set with different $Ri_B$.

## 3.3 Observations

### 3.3.1 Density evolution at the interface

Oglethorpe (2014) believed that the periodic mixing mode was the dominant mixing mechanism. She hypothesised continuous ejections of fluid parcels from the inner cylinder boundary layer which are then entrained in the periodic structure somewhere in the middle of the annulus. Hence, in order to understand the structure of this mixing mode, we performed two-layer STC experiments with the conductivity probe fixed at the interface at two different radial locations in the annular gap, close to the inner cylinder ($\sim 1.5\,\mathrm{cm}$ from the inner cylinder) and approximately in the middle of the annular gap. The density at those points on the interface is measured continuously over time. The schematic of the setup can be seen in figure 3.5. The Reynolds number for these experiments is $Re = 21000$ ($R_1 = 10\,\mathrm{cm}$ and $\Omega = 1.5\,\mathrm{rad\,s^{-1}}$) with a starting bulk Richardson number, $Ri_B \approx 12$. In each experiment, the probe is traversed vertically through the fluid in order to find the interface and then made to stay in the middle of the interface for 100 rotation periods of the inner cylinder, and the data was recorded. After 100 rotation periods, to correct for the change in position of the interface due to fluid siphoning by the conductivity probe, the probe is traversed again to locate the new position of the interface. This process is repeated until the fluid is completely mixed. A typical variation of density recorded at a point on the interface can be seen in figure 3.6a. Such data-sets recorded over time are analysed using the fast Fourier transform (FFT). Figure 3.6b shows the frequency spectrum for a data-set recorded at equal time intervals apart. Each colour represents the frequency spectra of a separate data-set evolving over time (or reducing $Ri_B$). $Ri_B$ is calculated using $\Delta\rho$ from the vertical traverse of the probe before each experiment. The blue curve is for the highest $Ri_B \approx 12$, while the the red one is at the lowest $Ri_B \approx 4$. A consistent peak in the frequency spectra is observed for all $Ri_B$, throughout the experiment. The time period is calculated, $T \approx 24\,\mathrm{s}$, which is consistent with the scaling (refer to equation 3.2) given by Oglethorpe (2014).

It can also be seen in figure 3.6b that there is a sudden drop of power of the mixing mode at some critical $Ri_B$. Figure 3.7a and 3.7b show the power of the most energetic mode (mixing mode) plotted against $Ri_B$ with the conductivity probe being placed near the inner cylinder and in the middle of the annular gap respectively. Data from three separate experiments at each of the probe locations are shown. A sudden drop in power is seen in all the experiments. Analysing figure 3.7, it can be seen the critical $Ri_B$ for drop of power of the mixing mode is $Ri_B \approx 7$. This is consistent with the point on the flux curve below which the buoyancy flux starts to increase rapidly (figure 2.10). We believe that there is some change in

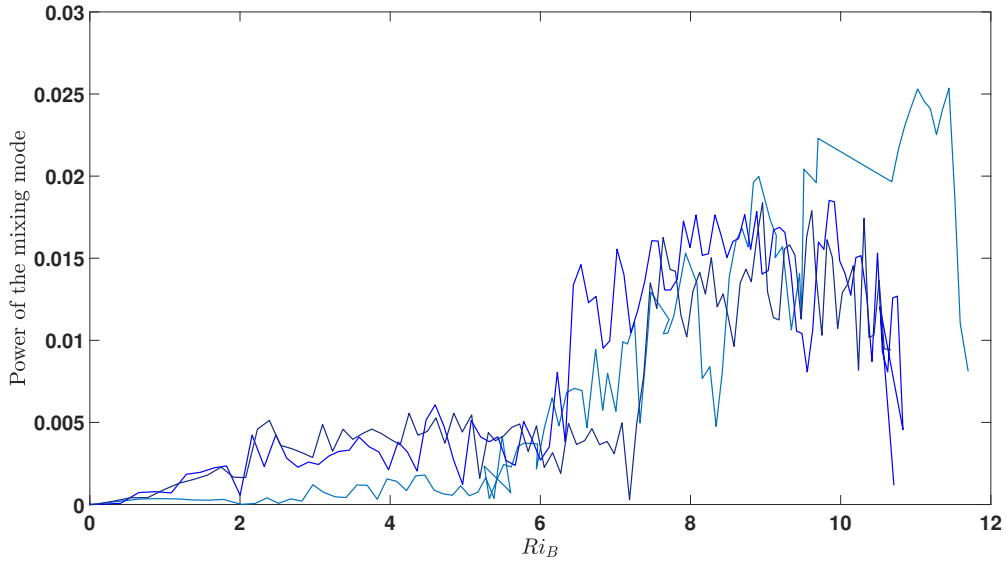


(a)

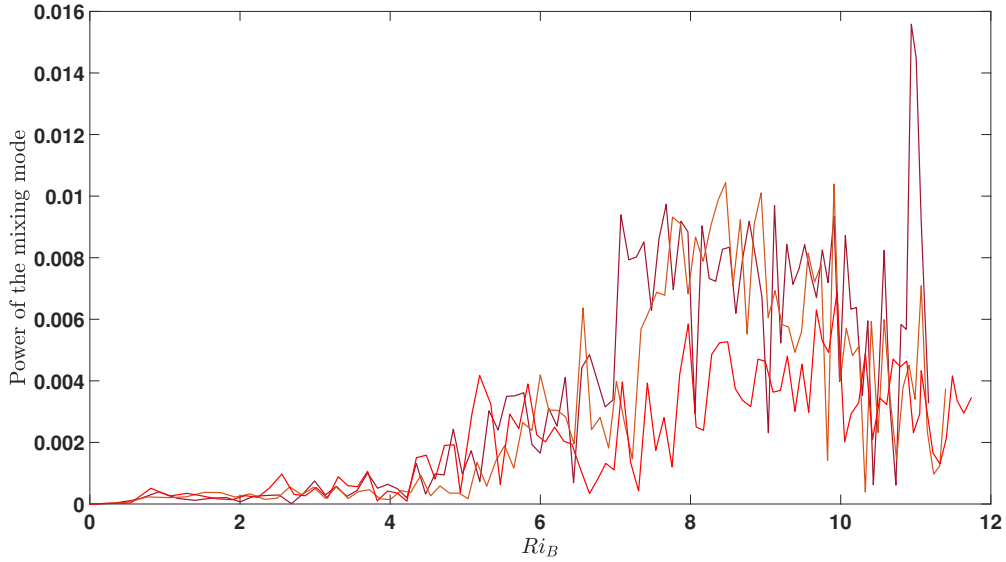


(b)

Fig. 3.7 The plot showing the power of the periodic mixing mode from the frequency spectrum plotted against Bulk Richardson number, $Ri_B$, with the conductivity probe being placed $(a)$ close to the inner cylinder ($\sim 1.5$ cm away from the inner cylinder) and $(b)$ approximately in the middle of the annular gap. Each curve is produced after analysing data from a separate experiment.

the nature of the instability at $Ri_B = 7$ that results in an enhanced flux. This will be discussed further in subsequent sections.

It seems, from the above mentioned results, that the mixing instability is different from that hypothesised by Oglethorpe (2014) for these following reasons. Oglethorpe (2014) believed that there is a continuous ejection of fluid parcels from the boundary layer of the inner cylinder, which then get entrained by the periodic structure in the annulus. Now it can be seen in figure 3.7 that the flow periodicity and its behaviour (sudden drop in power at the same point) is exactly the same both at the inner cylinder and in the middle of the annulus, which is contrary to Oglethorpe's hypothesis. Also, it can be seen that the power of the mixing mode at the high $Ri_B$ for experiments with the probe placed near the inner cylinder is almost double compared to that for experiments with probe in the middle. This strongly suggests that the periodic structure of the mixing mechanism is more associated with the boundaries. This again is contradictory to Oglethorpe's proposed mixing mechanism.

### 3.3.2 LIF visualisations in a vertical plane

As discussed in the previous section, the periodic mixing mechanism seems to have a differential radial structure, with it being more prominent near the cylinder boundary than in the annulus. Hence, in order to investigate the vertical structure of the instability, we performed a LIF experiment with the laser sheet being in the $r-z$ plane ($r =$ radial, $z =$ axial). The experiment was performed at $Re = 14000$ ($R_1 = 10\,\text{cm}$ and $\Omega = 1\,\text{rad}\,\text{s}^{-1}$) and a starting $Ri_B \sim 6.7$, just around the point where the buoyancy flux starts to increase rapidly (refer to figure 2.10). Refractive indices of fluids in the two layers is matched (refer section 3.2.3) and the fluorescent dye (Rhodamine 6G) is added in the bottom denser layer. Although the refractive indices of the two fluids are matched, the laser sheet being passed through the side of the tank sees a gradient at the sharp interface that results in distortions in the image. In order to check for that, the line laser was mounted at the top of the cylinder, producing a sheet along a radial line. In this case, the refractive index gradients in the path of the light sheet are reduced, hence reducing distortions.

It is observed that the flow periodically goes through a series of events. The snapshots of these events and their corresponding schematic of the observation is shown in figure 3.8. The colour in the snapshots is the virtual colour added to the images representing the relative concentration of the dye (closely proportional to the fluid density), with pink representing maximum concentration while red being zero concentration. The observed series of events are the following.

a) The flow starts with a base state where the interface is of almost constant thickness, approximately 1 cm, as seen in figure 3.8a. This is consistent with observations of Oglethorpe *et al.* (2013); Woods *et al.* (2010). It is observed that there are continuous

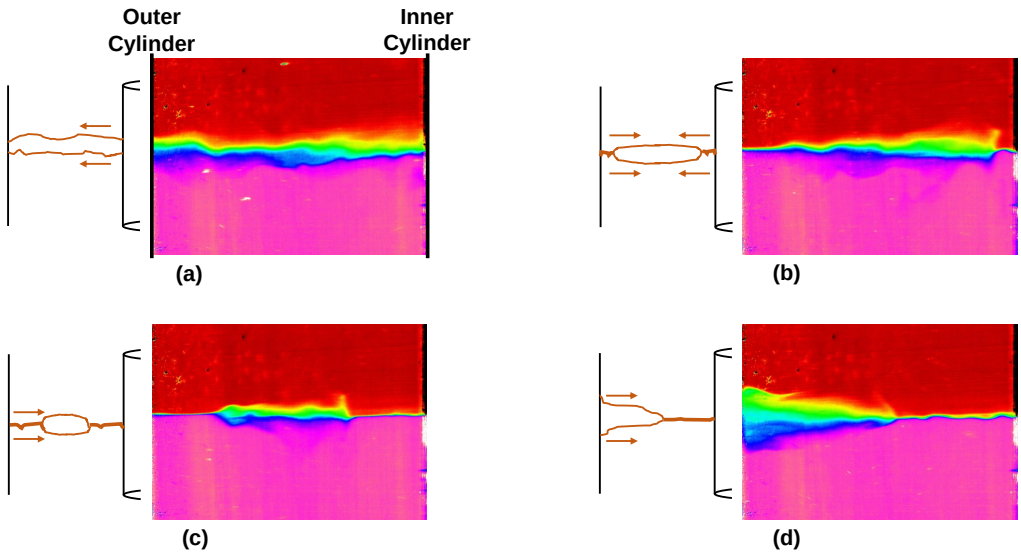


Fig. 3.8 $(a-d)$ Snapshots of series of events observed in a LIF experiment with vertical laser sheet. The schematic of the interface is also shown next to the snapshot image (on the left of the image). Colour represents the relative concentration of the dye present, where pink is the highest while red is the lowest. Colourbar is kept the same for all the snapshot images.

ejections of fluid parcels from the inner cylinder towards the outer cylinder occurring at the interface, resulting in wave-like distortions of the interface. The interface mostly stays sharp with some mixing because of 'scouring' by the turbulent eddies in each layer.

b) An instability then develops on the interface at the boundary of the inner and the outer cylinder, pushing the mixed fluid from both boundaries towards the centre of the annular region (figure 3.8b). The instability results in a formation of a very sharp interface, $\sim 1$ mm, near the cylinder boundaries. The extent of these sharp interfaces continues to grow, pushing the mixed fluid further towards the centre, forming a hydraulic jump-like formation starting from each boundary (figure 3.8c).

c) The ejection of fluid parcels from the inner cylinder still continues, and is even more obvious from the wave-like disturbances travelling on the very sharp interface towards the outer cylinder. The fluid parcels are continually entrained into the mixed fluid region in the centre. The enhanced momentum of the mixed fluid region then pushes it outward toward the outer cylinder.

d) The mixed fluid region continues to move outward, and splashes onto the outer cylinder, which caused vertical motion of the fluid at the cylinder boundary (figure 3.8d). This splashing is followed by homogenisation of the mixed fluid in the layers by turbulent eddies present in each layer. This process results in the dominant part of the mixing. This splashing is observed as a mixing event in the shadowgraph time series (figure 1.5), as it reduces the density gradients which are being visualised by the technique. The stable stratification present then starts to act and produces a buoyancy force to suppress the vertical motion of the mixed fluid. This pushes the mixed fluid region back towards the inner cylinder as a gravity current on the interface. Once the current reaches the inner cylinder boundary, the interface achieves the constant thickness again, as seen in figure 3.8a. This process continues periodically throughout.

As mixing happens, the observed period for these serious of events stays the same throughout irrespective of $Ri_B$, and is consistent with that observed by Oglethorpe (2014) (section 3.2). Note that it is this periodic splashing instability which goes around the annulus with azimuthal mode, $m = 1$ (section 3.1). The subsequent growth and then collapse of the formation of sharp interfaces also points towards its wave-like nature.

A similar experiment is also performed with linear stratification in the middle third of the tank and unstratified layers at the top and bottom (in order to have no end wall effects). Time-series of a vertical line from the LIF data at three different locations (5 cm from inner cylinder, middle of the annular gap and 5 cm from the outer cylinder) is shown in figure 3.9. The same mixing phenomenon and the period is observed at each of the interfaces as that in the above shown two-layer case. The presence of coupling between adjacent interfaces is also observed, similar to that observed in a shadowgraph experiment (figure 1.5). This strongly suggests that the mixing mechanism is the same in a linear STC as well. It is worth noting here that this observed mixing phenomenon is very different from that hypothesised by Oglethorpe.

### 3.3.3 Quantitative measurements of STC mixing mode

It has been discussed in the previous section that the structure of the periodic mixing mechanism is more complex than that hypothesised by Oglethorpe (2014). The instability results in formation of a very thin interface at both the cylinders, unlike mixed fluid parcels building up near the inner cylinder as suggested by Oglethorpe. Now, referring to figure 3.8, the interface thickness in figure 3.8a is approximately the same as the thickness of the mixed fluid region in figure 3.8c when the instability wave (forming a very sharp interface) is at its maximum amplitude at both cylinder boundaries. This means that when the extremely sharp

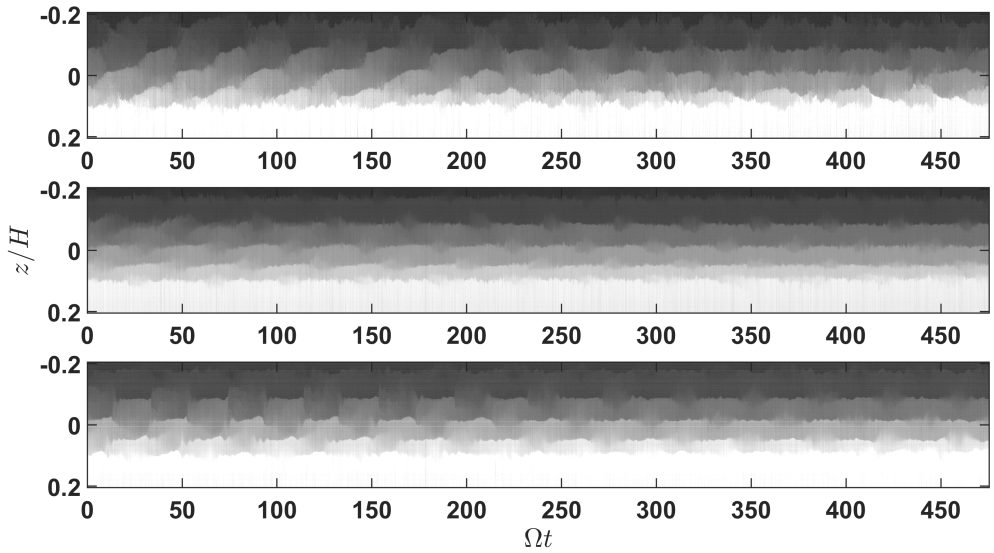


Fig. 3.9 Time series of a vertical line from the LIF data at 5 cm from the inner cylinder (top), at the middle of the annulus gap (middle), and at 5 cm from the outer cylinder (bottom), for a linear STC experiment with unstratified layers at the top and bottom. Periodic mixing process is observed at the interfaces, consistent with that on an individual interface in a two-layer stratified STC experiment (refer to figure 1.5, 3.1 and 3.8).

interface is formed, the mixed fluid from near the cylinder boundaries is being pushed in the azimuthal direction, which suggests a three dimensional nature to this mixing instability. We look into this using simultaneous LIF and PIV. The setup used is shown in figure 3.3.

The experiment is a two-layer STC performed at $Re = 14000$ ($R_1 = 10\,\text{cm}$ and $\Omega = 1\,\text{rad}\,\text{s}^{-1}$) and a starting $Ri_B \approx 7.5$. Refractive indices of the fluids in the two layers are matched. The laser sheet is made to pass horizontally at the interface and two cameras are mounted above the tank and positioned to look at the plane of the laser sheet through the acrylic lid. After taking the calibration image in the plane of the laser sheet, the experiment is started. Various LIF and PIV measurements are performed at different $Ri_B$ over time.

### Mean flow properties

The experiments shown above are all for fully turbulent flows. The observed instability requires a sharp interface, which is only achieved by scouring by turbulent eddies in the well-mixed layers (Woods *et al.*, 2010). For a low *Re* flow, diffusion will dominate and will make the interface thicker. This is consistent with the observations of Crapper & Linden (1974) who looked at the structure of density interface in a two-layer grid-generated turbulence experiment. They found that the structure of the interface is a function of Péclet number, *Pe*

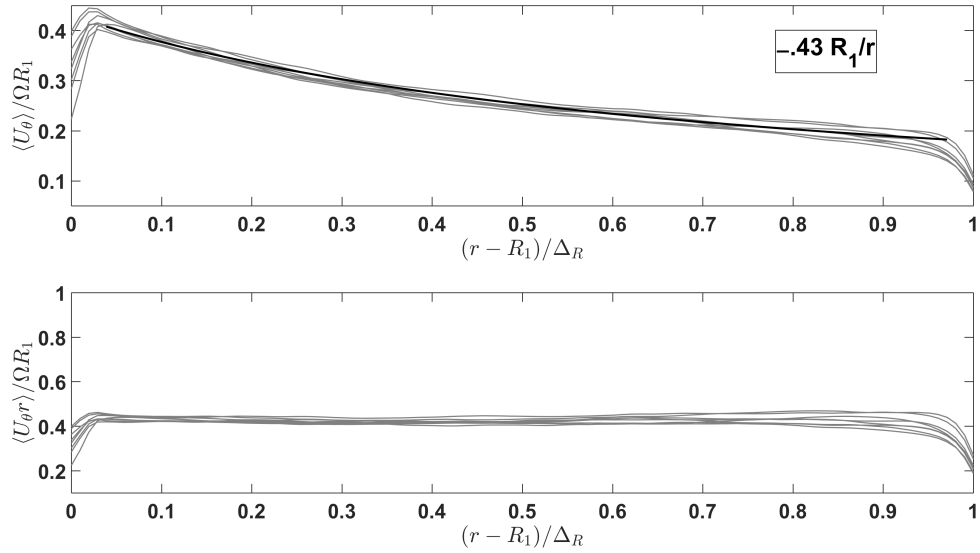


Fig. 3.10 Plot showing variation of mean azimuthal velocity (top plot) and mean angular momentum (bottom plot) along the annular gap. Each grey line represents a different PIV experiments. The black line is best-fit plot to the data. It can be seen that angular velocity goes as the inverse of radius and the angular momentum is constant in the bulk of the flow which shows the flow is turbulent.

($= Re \times Sc$). Hence, in order to understand the above observed instability, it is important to make sure that the flow is turbulent.

The mean azimuthal velocity, $U_\theta$ in a turbulent Taylor-Couette flow is known to be a function of radius, $r$ (Lewis & Swinney, 1999; Oglethorpe, 2014; Woods *et al.*, 2010) and is given as

$$U_\theta(r) = \frac{A\Omega R_1^2}{r} \tag{3.3}$$

where $A$ is a constant and is specific to the cylinder. Oglethorpe (2014) empirically found that $A \approx 0.48 \pm 0.021$ for the smooth inner cylinders, which was similar to that in previous studies (Lewis & Swinney, 1999; Smith & Townsend, 1982). For rough cylinders, she found $A \approx 0.57 \pm 0.024$.

In order to check for the turbulent flow, eight different PIV experiments are performed with reducing $Ri_B$. The laser sheet for these experiments was placed $\sim 6$ mm below the actual interface. Figure 3.10 show the mean angular velocity and mean angular momentum along one radial line for these eight experiments. It is seen that mean azimuthal velocity in the bulk of the annulus goes as the inverse of radial distance from the inner cylinder, which can be

also verified from the fact that angular momentum for these experiments in constant in the annular gap. The black line in figure 3.10 is the best-fit line to the mean angular velocity data. We find the constant $A = 0.43$, which is very close to that given by Oglethorpe (2014), indicating that the flow is turbulent.

### Velocity measurements at the interface

In this section, we look into the variation in radial and azimuthal velocities at the interface to get further insights into the three dimensional structure of the mixing instability. The experiments are performed at $Re = 14000$ with a starting $Ri_B \approx 7$. The laser sheet for these experiments is placed at the interface. Figure 3.11a and figure 3.11b show the time-series of the radial velocity and the azimuthal velocity respectively, after subtracting the respective time averaged mean along a radial line. A periodic signal is observed in all three plots. There is a periodic enhancement of the radial velocity near the inner cylinder (figure 3.11a). We believe that this is because of the instability, which results in the formation of a very sharp interface, passing by and pushing the fluid into the annulus. High frequency waves are also seen to be riding on this periodic structure, representing the continuous ejection of fluid parcels from the inner cylinder. There is no obvious periodicity in the radial velocity signal near the outer cylinder. This is most likely because of low mean velocity, meaning perturbations there are much smaller compared to those near the inner cylinder. A high frequency signal near the inner cylinder is also observed for the azimuthal velocity, as can been seen in figure 3.11b. The extent of this high frequency region into the annulus is exactly the same as that observed for radial velocity, which we believe represents the extent of the sharp interface into the annulus. Now, the lack of any high frequency data near the outer cylinder means that the ejected fluid parcels from the inner cylinder do not reach the outer cylinder and are entrained within the mixed fluid blob in the centre of the annulus. This causes the mixed fluid blob to move out towards the outer cylinder as observed in figure 3.8.

Beyond the extent of the high frequency region, a periodic enhancement of the azimuthal velocity is observed. This is consistent from the point of view of conservation of energy. As the sharp interface is formed, the mixed fluid parcels near the inner cylinder, containing a lot of energy, are pushed out towards the middle of the annulus. Now, since the thickness of the mixed fluid region does not increase, these energetic fluid parcels are pushed further in the azimuthal direction, resulting in an increase of azimuthal velocity. Also to note this periodic increase in azimuthal velocity near the outer cylinder happens in a pair of two separate enhancements. The splashing fluid on the outer cylinder forms a gravity current and spreads in both the mixed layers. The presence of stable stratification pushes this gravity current back towards the interface. This causes the formation of the observed second increase

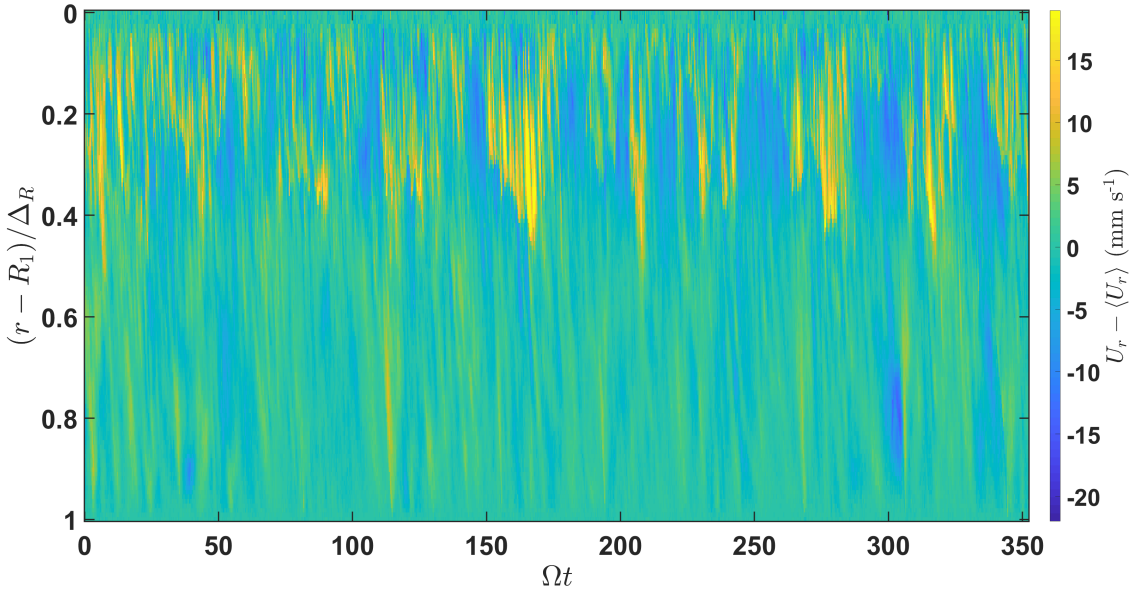


(a)

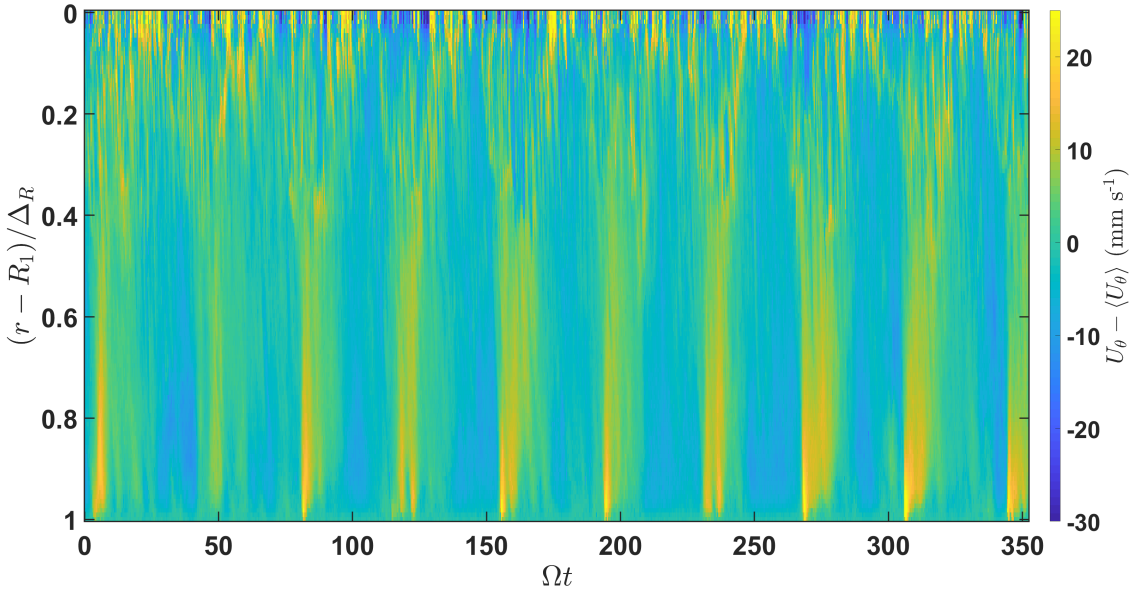


(b)

Fig. 3.11 Plot showing time-series, along one radial line in the annulus, of $(a)$ radial velocity after removing the mean, and $(b)$ azimuthal velocity after removing the mean. The mean azimuthal velocity near the inner cylinder is $\approx 41\,\mathrm{mm\,s^{-1}}$ (figure 3.10).

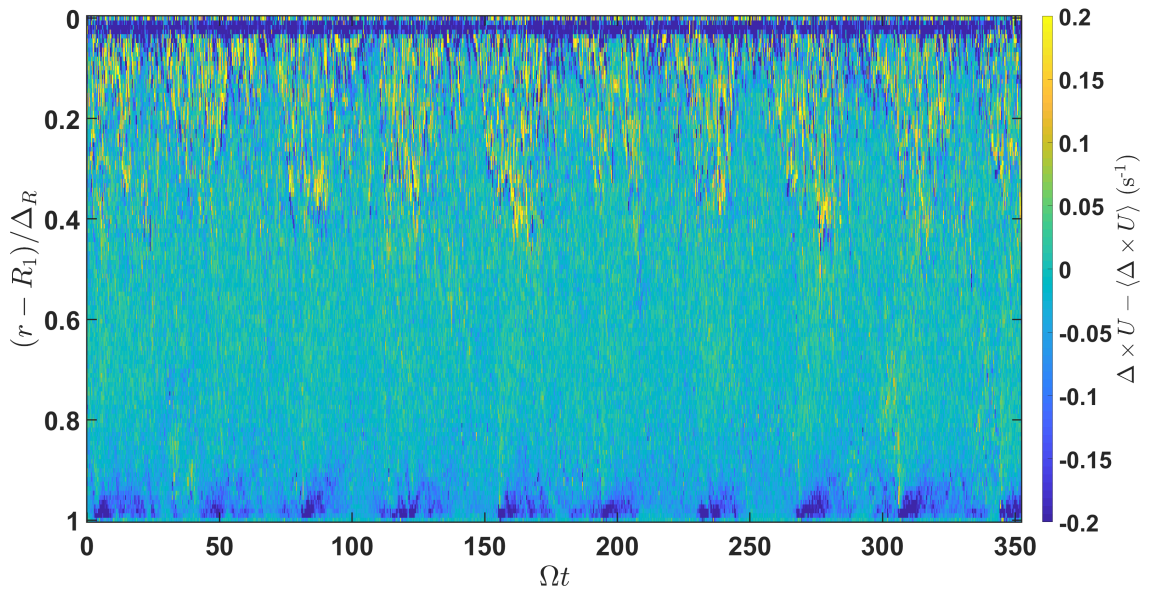


(c)

Fig. 3.11 $(c)$ Plot showing time-series of observed vertical vorticity in the flow, along one radial line in the annulus.

of azimuthal velocity. Figure 3.11c shows the vertical vorticity along the same radial line plotted over time. A periodic increase of vertical vorticity at the inner cylinder and a periodic decrease at the outer cylinder is observed, representing the fluid from both boundaries being pushed towards the annulus, while an extremely sharp interface is being formed. This points towards the presence of an in-phase wave-like structure at both cylinder boundaries.

We further look into evolution of the above velocity data at different radial locations using the fast Fourier transform. Figure 3.12 shows the frequency spectrum of the radial velocity, azimuthal velocity, total velocity and vorticity data (same as shown in figure 3.11). Each curve represents a different radial location. The blue colour represents the spectrum for a location near the inner cylinder boundary while the red shows the location near the outer cylinder boundary. The dashed black line is the expected period of the mixing mode calculated using equation 3.2. A strong peak at the mixing mode frequency is observed for the FFT of radial velocity perturbations data near the inner cylinder, which is consistent with our previous observations. A peak is also observed in the FFT of vorticity data, both near the inner and the outer cylinder boundaries, indicating the possibility of this instability being associated with waves at each of the cylinder boundary.

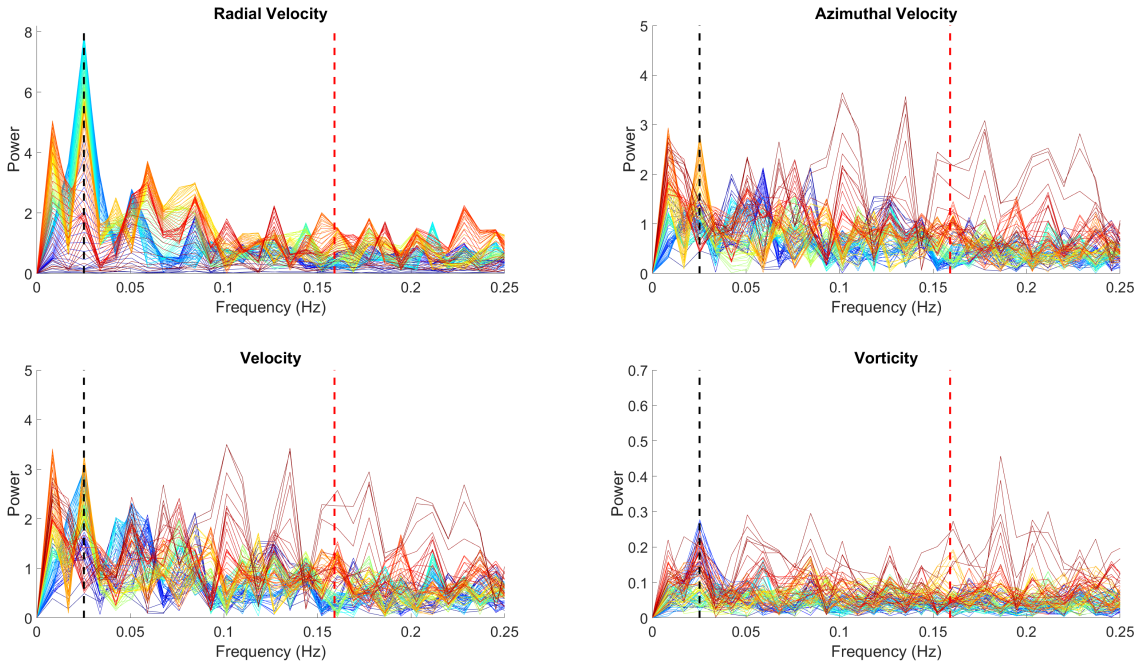


Fig. 3.12 Plot showing frequency spectra of fluctuations in radial velocity, azimuthal velocity, total velocity and vorticity respectively. The blue colour represents the spectrum for a location near the inner cylinder boundary while the red shows the location near the outer cylinder boundary. The dashed black line represents the frequency of the periodic mixing mode observed by Oglethorpe (2014) and the dashed red line represents the rotation frequency. The dashed red line is period of inner cylinder rotation.

### Simultaneous LIF and PIV at the interface

In the previous sections, we looked into the vertical scalar structure of the mixing instability and the velocity field in a horizontal plane. Analysing the data, we hypothesised an interaction between the density and velocity fields. In this section, we look into the evolution of density and velocity information in the horizontal plane simultaneously. The experiment is performed at $Re = 14000$ and starting $Ri_B \approx 7$ and with two cameras mounted at the top of the tank, one for LIF and the other for PIV. The fluorescent dye is added in the lower (denser) layer. Although we tried to ensure that the laser sheet is at the interface, owing to the structure of the instability, a very sharp interface is formed, approximately 1 mm thick, and the laser sheet ended up being either above or below the interface.

The results from the above experiment are shown in figure 3.13. Figure 3.13a shows the evolution of azimuthal velocity perturbations along a radial line, while figure 3.13b shows the evolution of density information along the same radial line. A high frequency zone near the

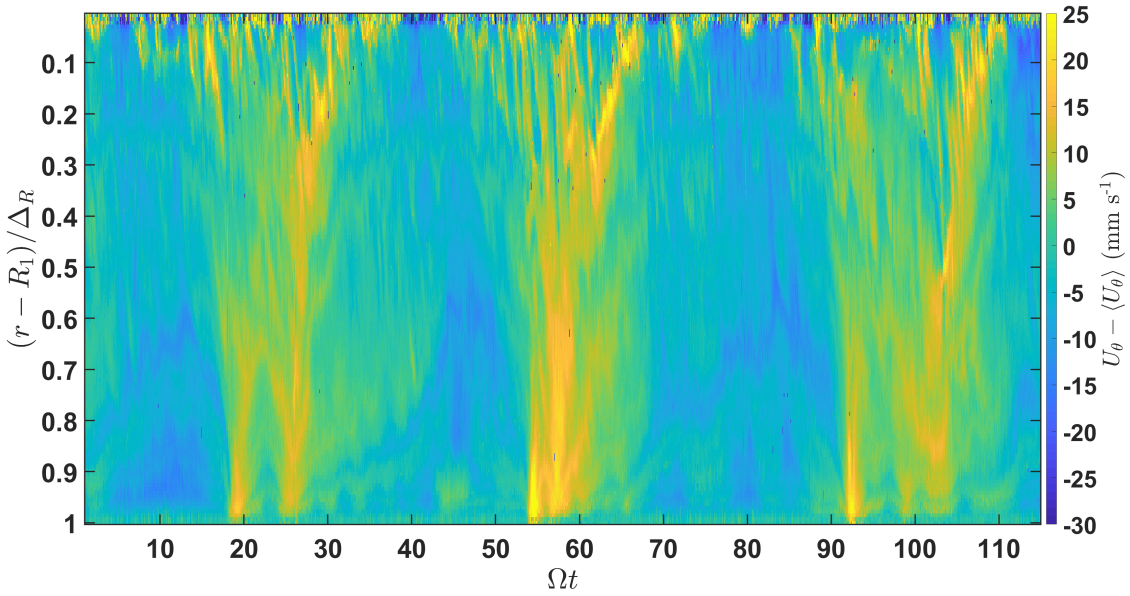


(a)

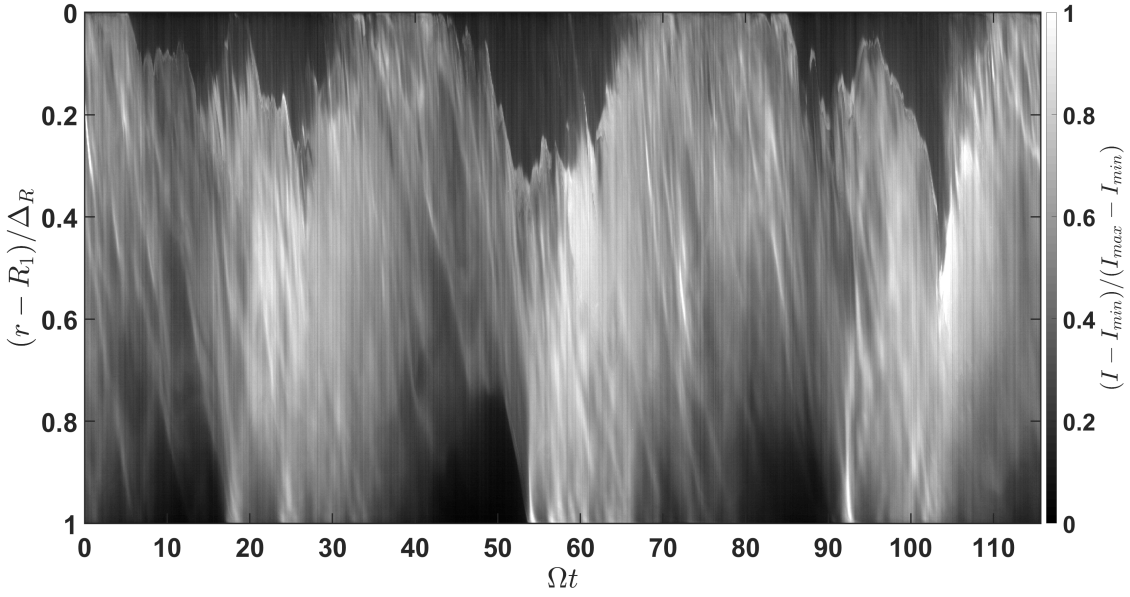


(b)

Fig. 3.13 Plot showing the simultaneous evolution of ($a$) azimuthal velocity and ($b$) scalar field, along one radial line, over time. Two boundary trapped waves, in phase with each other are observed. Colourbar for $(a)$ is same as that used in figure 3.11b.

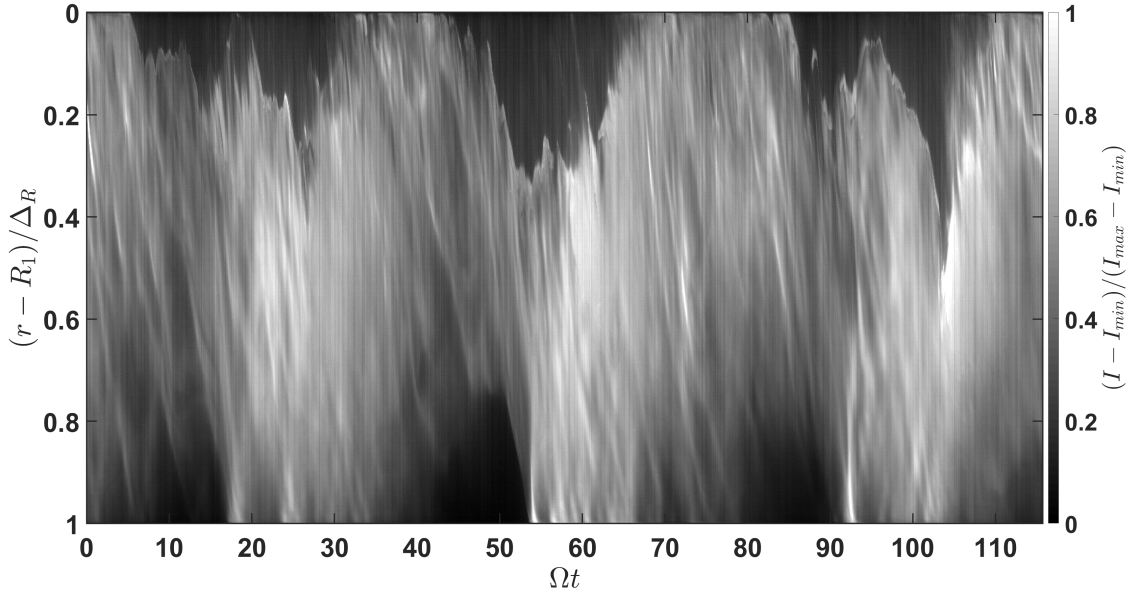


(a)

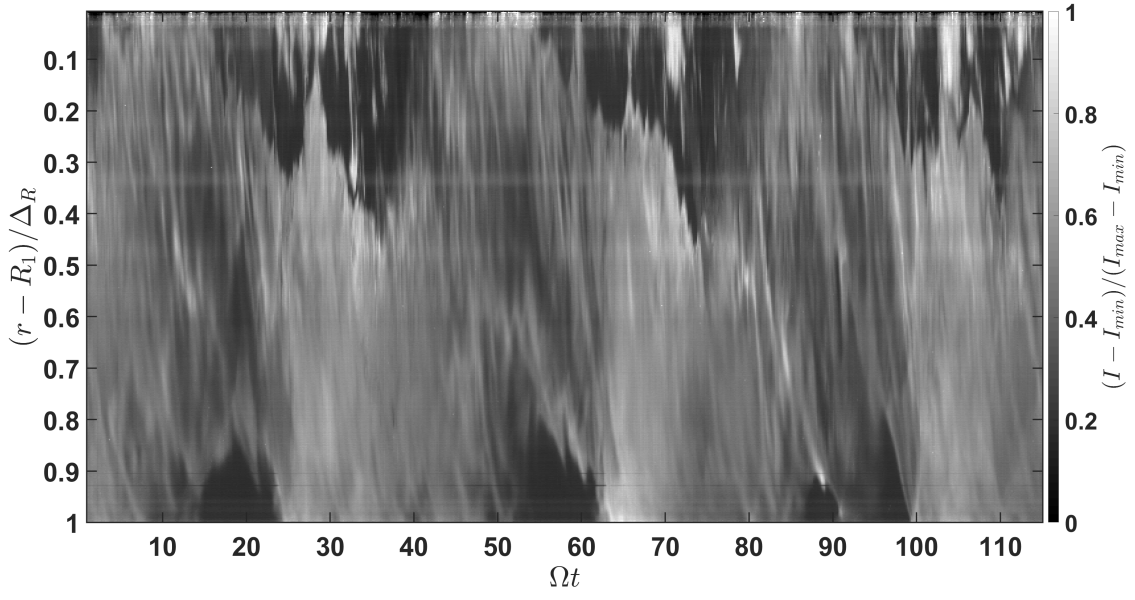


(b)

Fig. 3.14 Plot showing LIF time series along a radial line over time, over time for an experiment $(a)$ same as figure 3.13b with horizontal laser sheet, and $(b)$ same as figure 3.8 with vertical laser sheet. Note that for the experiment shown in $(a)$ the fluorescent dye was added in the lower layer, while that for experiment in $(b)$, it was added in the upper layer.

inner cylinder and a periodic increase of azimuthal velocity beyond that is observed, similar to figure 3.11b. In the LIF time-series, a periodic occurrence of dark zones is observed. This formation of dark zones occur because the laser sheet ends up being in the upper layer (without the dye) when the instability results in an extremely sharp interface. As mentioned in the previous section, the extent of the high frequency zone is the same as the extent of the extremely sharp interface near the inner cylinder into the annulus. Similarly, the extent of the dark zone near the outer cylinder represents the extent of the extremely sharp interface into the annulus. It is also seen that the dark zones at the outer cylinder are suppressed suddenly by the mixed fluid blob moving towards the outer boundary. More importantly, figure 3.13b gives clear evidence of the presence of waves, one at each boundary, which aids in mixing across the interface. Also, these waves have azimuthal mode, $m = 1$ throughout.

To validate our results, we also looked at another experiment with a vertical laser sheet, similar to that in figure 3.8. This experiment is performed at the same parameters as above, $Re = 14000$ and starting $Ri_B \approx 7$. The laser sheet was passed from the side, and the fluorescent dye was added in the upper layer. Figure 3.14b show the time-series of LIF data along a radial line and is compared to the time series from the experiment with a horizontal laser sheet. It is seen that the flow mechanism and the period in both the experiments is consistent. Also, note that the radial line from the vertical LIF to plot the time series shown in figure 3.14b is chosen to be just below the very sharp interface, and since it is the upper layer where dye is present, the dark zones represents fluid from the denser layer, unlike that in figure 3.14a. The fact that figures 3.14a and 3.14b match so well, it demonstrates the symmetric nature of this instability across the interface.

## 3.4 Analysis

In the previous section, we looked into the structure of the $m = 1$ mixing instability. A schematic to show the structure of the observed $m = 1$ instability on the density interface is shown in figure 3.15. We find the presence of two $m = 1$ boundary trapped waves (blue region in figure 3.15) which create an extremely sharp interface and resulting flow behaviour causes mixing. In this chapter, we look into the mixing behaviour and its evolution as $Ri_B$ reduces.

As observed and discussed in the previous section, there are two processes that result from the instability that cause mixing. They are the following:

1. The flow in each of the well-mixed layers is turbulent. The presence of large scale eddies scour the interface and cause mixing. This is also the process behind sharpening of the initially diffused layer when the experiment is started (discussed in section 2.3).

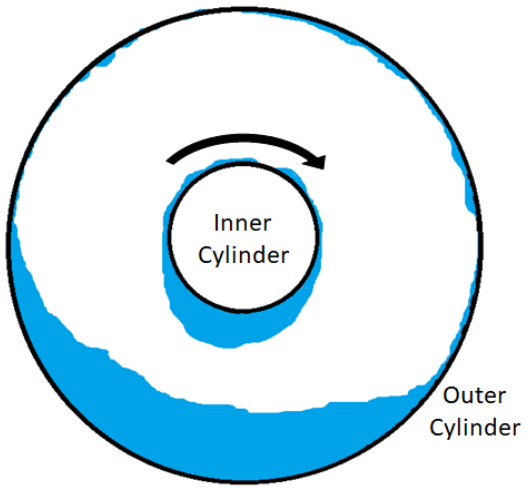


Fig. 3.15 Schematic on the observed $m = 1$ instability with two in-phase boundary trapped waves at each cylinder boundary on the density interface. The blue region represents the extremely sharp interface region formed as a result of these waves which moves around the annulus at a constant period.

While the tank is being filled, diffusion causes the interface to thicken, which means there are regions on the interface (top and bottom of the interface) where the local *Ri* is relatively low. The turbulence generated when the cylinder is rotated overturns those areas and results in mixing. During the experiment, although the stable stratification resists vertical motion of the fluid, the non-linear effects of turbulence in the mixed layer results in vertical perturbations to the fluid parcels (as seen in figure 3.17a). This causes reduction in local *Ri* around those fluid parcels which are then mixed by the flow in the layers. This process continues throughout the experiment. It is useful to note here that although there are waves causing vertical motion on the extremely sharp interface as the instability waves are passing by, the local *Ri* is extremely high and there is negligible mixing happening across those regions, consistent with our observations in LIF experiments (figure 3.17b).

2. Because of high momentum at the inner cylinder, the fluid parcels are constantly being ejected into the annulus, riding on the interface. These fluid parcels are entrained by the mixed fluid blob in the middle of the annulus, formed as a result of the instability (figure 3.8). This pushes the blob outwards which then splashes onto the outer cylinder. Qualitatively, this splash is relatively violent and appears to cause a lot of mixing.

We believe that the mixing due to the latter mechanism is the dominant one. Now in order to find the dominant mixing process among these, we plot the time-series of a vertical line in the recorded LIF data at three different locations, at 5cm from inner cylinder, in the middle of the annular gap and at 5 cm from the outer cylinder. These time-series are shown in figure 3.16. The data from the experiment shown in figure 3.8 is used. This gives us a good idea of the thickness of the interface at all times. Periodic peaks are seen both near the inner and the outer cylinder, representing the presence of mixed fluid layer and a very sharp interface intermittently. The time-series from the centre of the annulus always shows a presence of a mixed layer meaning that the the extent of the sharp interface does not extend till the middle of the annulus at that $Ri_B$ ($Ri_B \approx 6.4$). Similar behaviour is also seen in figure 3.9 on the interfaces formed in a an initially linearly STC flow experiment, where $Ri_B$ across each interface is significantly lower compared to that in the above experiment. Because of splashing at the outer cylinder, the height of the peak at the outer cylinder is higher than that at the inner cylinder. It is also seen that the peak at the inner cylinder lags behind that at the outer cylinder, as it is the stratification acting on the splashing fluid that pushes the mixed fluid back towards the inner cylinder. More importantly, it is interesting to note that the overall region covered by peaks is smaller compared to when the interface is very sharp. This means that there is a sharp interface present throughout a significant chunk of the instability period. This means that the region of the interface available for scouring is much reduced. This is consistent with our assumption that splashing causes the dominant mixing. This is discussed further in the next subsection.

### 3.4.1 Flux due to scouring with reducing $Ri_B$

As the mixing progresses, the mixing instability for a two-layer STC has always mode, $m = 1$. At the same time, we also know that the buoyancy flux increases with reducing $Ri_B$ and more rapidly below $Ri_B = 7$. In this section, we analyse the results from the PIV and LIF experiments shown in the previous section at different *RiB*, to get further insights into the mixing process. Before every experiment, fluid from each of the layers is taken out and its measured density is used to calculate $Ri_B$.

Figure 3.17a shows the snapshot of the interface at five different $Ri_B$, just before the formation of a very sharp interface at the inner cylinder boundary. The clearest image from the five images before the start of the instability (formation of the sharp interface) at the inner cylinder is chosen for figure 3.17a. The images taken are recorded at 5 fps. It is observed that the interface thickness in the base state increases with reducing $Ri_B$. This can also be seen for density profiles with reducing $Ri_B$ in figure 2.7b. This increase in interface thickness means an enhanced reduction in the density gradient at the interface, which means that the

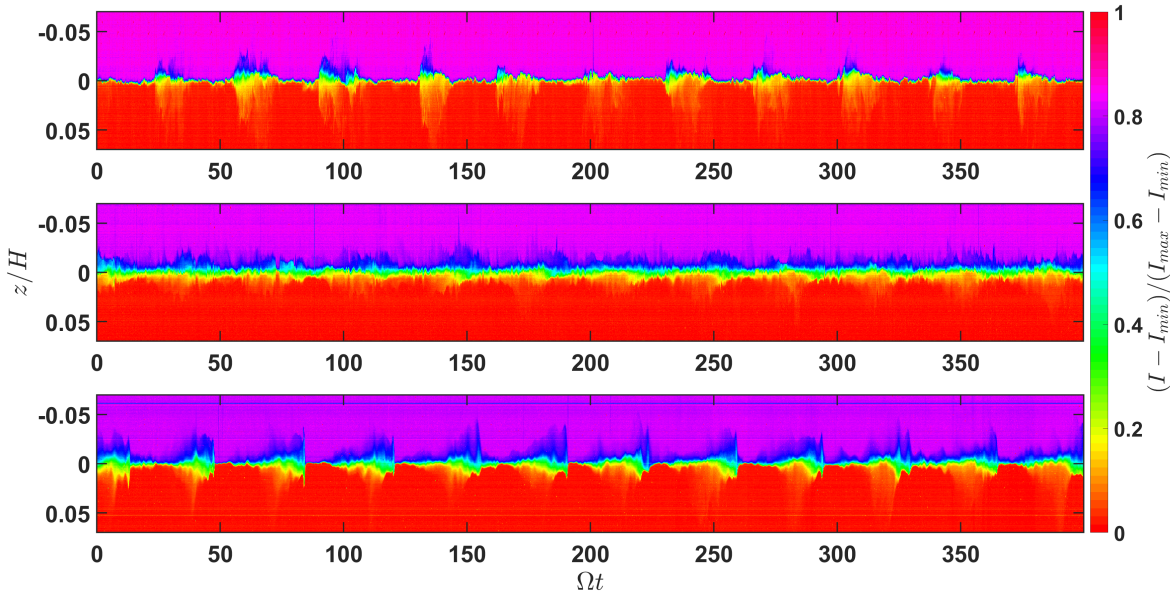


Fig. 3.16 Time series of a vertical line from the LIF data at 5 cm from the inner cylinder (top), at the middle of the annulus gap (middle), and at 5 cm from the outer cylinder (bottom). $Ri_B \approx 6.4$.

fluid parcels need less energy to overcome resistance to the vertical motion (as the local $Ri$ at the interface reduces more than if it was just because of a reduction in the density difference). This results in enhanced transport across the interface due to 'scouring'. This is also seen in figure 3.17a where there are more ejections of fluid parcels into the layers with reducing $Ri_B$. But this is only true when the instability wave is not passing by. As seen in figure 3.16, the interface forms an extremely sharp interface near the cylinder boundaries for most of the instability period, across which there is negligible transport. Figure 3.17b shows the interface when the instability waves at both cylinders are at their maximum amplitude (beyond this point the mixed fluid blob starts to move towards the outer cylinder). It is seen that the amplitude of the instability waves is much larger at lower $Ri_B$ compared to that at high $Ri_B$. This means as the $Ri_B$ reduces, there is less surface area available for mixing to occur. We believe that, with reducing $Ri_B$, the enhanced flux resulting from enhanced vertical motion of the fluid (due to a reduced density gradient at the interface) is balanced by the reduction in the surface area available for flux transport itself, and enhanced 'scouring' is possibly is not the reason behind the observed rapid increase of buoyancy flux beyond $Ri_B = 7$.

It is worth noting here that the enhanced area with an extremely sharp interface would also mean enhanced flux due to diffusion. Figure 3.18 shows the time-series of the recorded LIF data for a radial line just above the extremely sharp interface with varying $Ri_B$. The dark

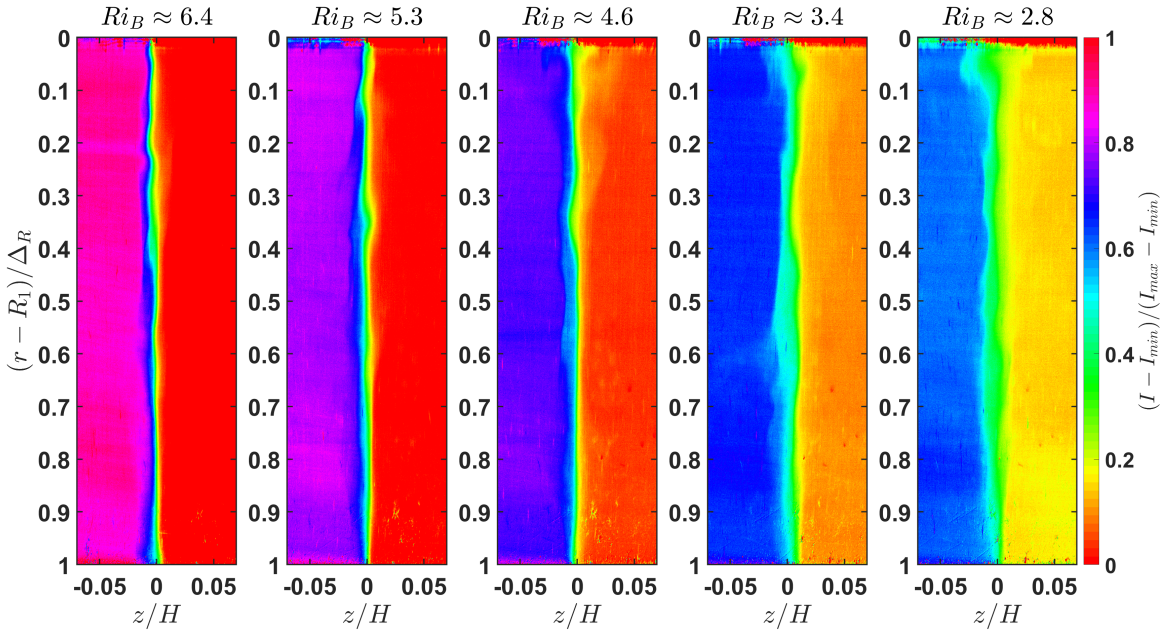


(a)

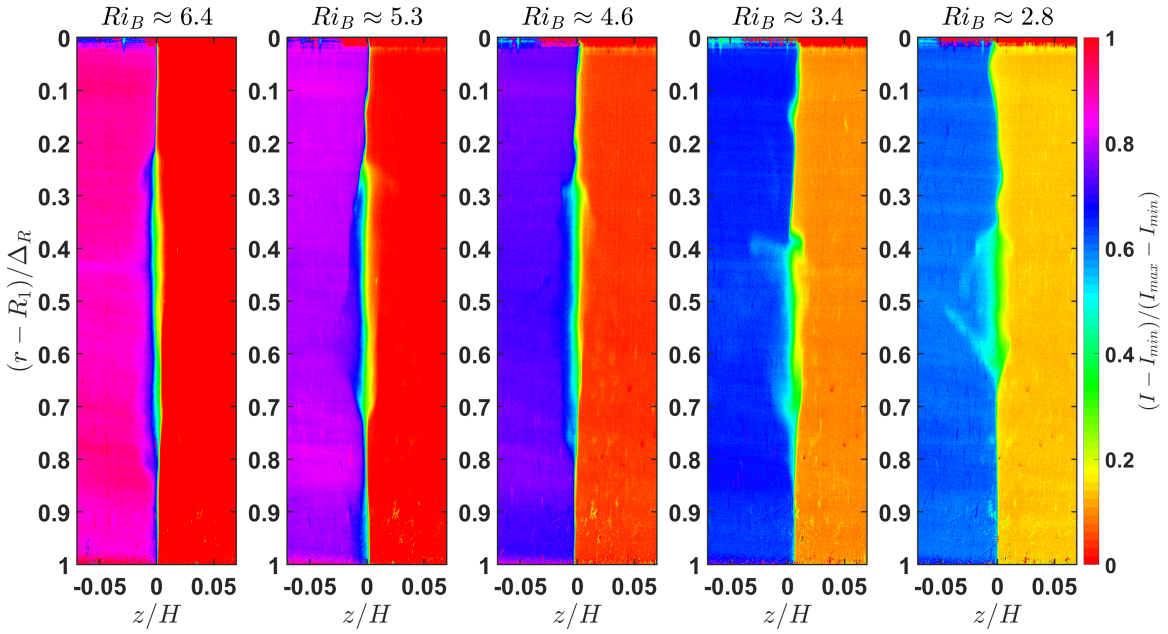


(b)

Fig. 3.17 Structure of the interface at the instance $(a)$ when the instability waves have gone past i.e. the interfaces has approximately constant thickness throughout, and $(b)$ when there is peak amplitude for the instability waves at both cylinder boundaries, with varying $Ri_B$.

zones represents the interface being extremely sharp. Looking at figure 3.18, although we can get the gist of the average area with sharp interface increasing with reducing $Ri_B$, it is

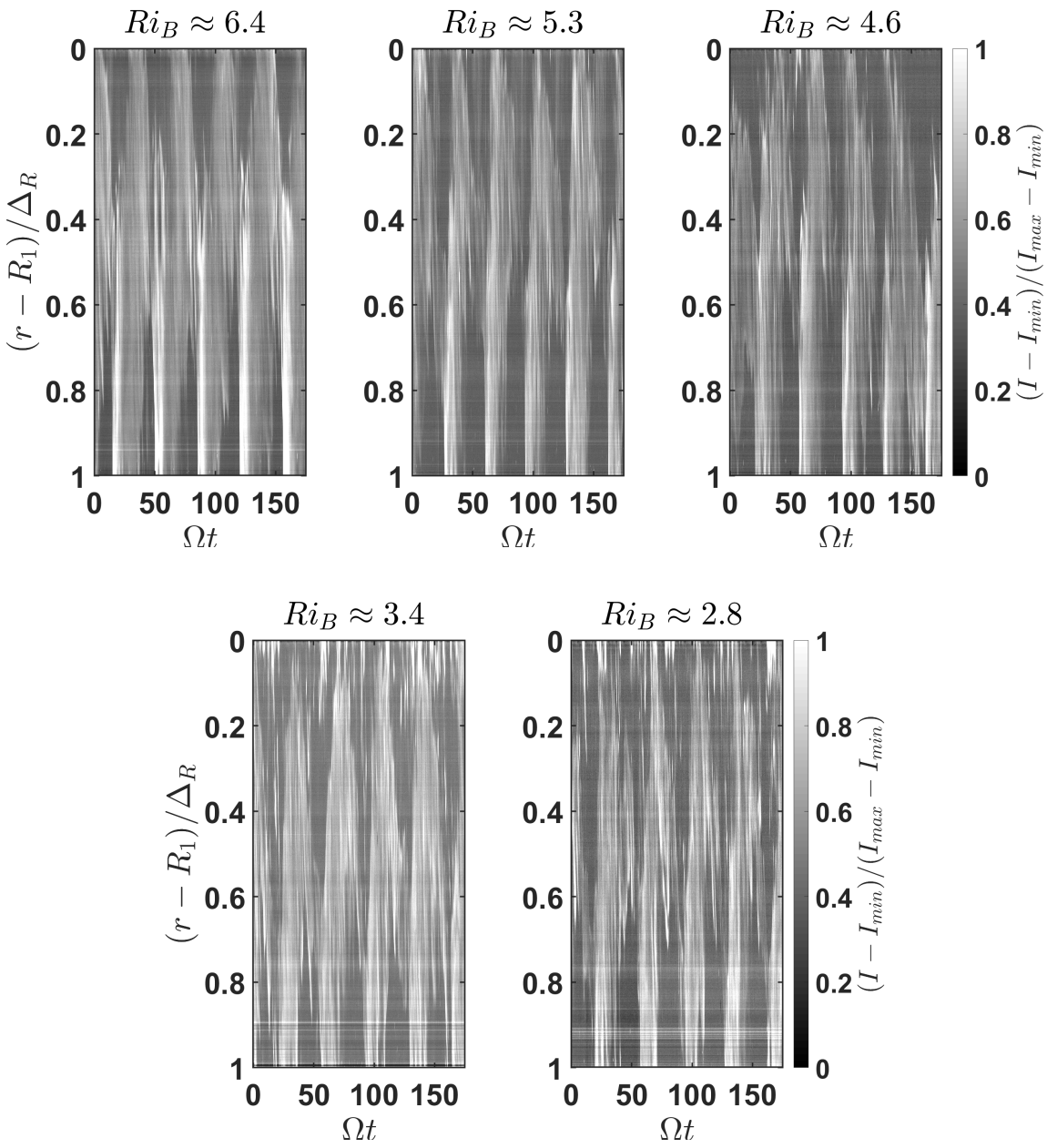


Fig. 3.18 Plot showing time series of the recorded LIF data along a radial line just above the extremely sharp interface, for 5 instability periods, with varying $Ri_B$. The experiment was performed at $Re = 14000$ with the fluorescent dye added in the lower layer. Colourbar is arbitrarily decided for each plot ($I_{min}$ and $I_{max}$ are decided for each plot separately).

very difficult to accurately quantify it with the present limited data, owing to the extremely turbulent nature of the flow, especially at lower $Ri_B$. In a nutshell, it can be seen that although area with extremely sharp interface is increasing, the rate of increase is lower with reducing

$Ri_B$. Now since diffusive flux across the sharp interface is proportional to the surface area, the observed significantly enhanced flux at lower $Ri_B$ can not be explained by the enhanced diffusive flux here.

### 3.4.2 Flux due to splashing with reducing $Ri_B$

We look into mixing caused due to splashing of the mixed fluid blob at the outer cylinder with reducing $Ri_B$. Soon after the instability waves on both boundaries have reached their maximum amplitude for that $Ri_B$, the mixed fluid blob starts to move outwards and splashes onto the boundary. As discussed in section 3.3.3, there are continuous ejections of fluid parcels (which can be seen on the sharp interface in figure 3.19b) from the boundary layer of the inner cylinder which are entrained into the mixed fluid blob in the annulus. These fluid parcels do not reach the outer cylinder. Figure 3.19a show the time series of phase averaged azimuthal velocity perturbation along one radial line. The data from the experiments shown in figure 3.11 are used. An FFT is performed on the data near the outer cylinder to get the exact observed period. This period is used to get the phase averaged data. It is observed that the extent of the instability wave at the inner cylinder (high frequency region) goes much further into the annulus with reducing $Ri_B$. It is also seen that the intensity of periodic increase in azimuthal velocity reduces with reducing $Ri_B$, which points towards enhanced vertical velocity during the splashing. Figure 3.19b shows the snapshots of the interface at five different $Ri_B$ just before the mixed fluid blob is to splash at the interface. The spread of the mixed fluid blob is much smaller at lower $Ri_B$, which means less resistance to the high energy fluid parcels to reach the outer cylinder. This means that there is a stronger splash at lower $Ri_B$ resulting in higher vertical velocities, and in turn, more mixing. We believe that it is this enhanced splashing which is causing increased flux at lower $Ri_B$.

The enhancement of splashing can also be looked at using energy arguments. These arguments were originally proposed by Oglethorpe (2014), but are used in a different context here. The stronger mixing in the inner boundary layer causes the formation of a region of mixed fluid near the interface. Assuming that the vertical extent of this region is $h$, we expect $h$ to be proportional to $1/\Delta\rho$, since potential energy is proportional to $\Delta\rho$. Now the work done on the fluid by mixing to raise it to the height $h$ is stored in the mixed fluid region as potential energy, which is given as

$$W \propto (\frac{g\Delta\rho}{\rho_0})h \tag{3.4}$$

where W is the work done per unit mass. As proposed by Boubnov *et al.* (1995), the work is required to be done against the radial pressure gradient for the fluid parcel to move towards

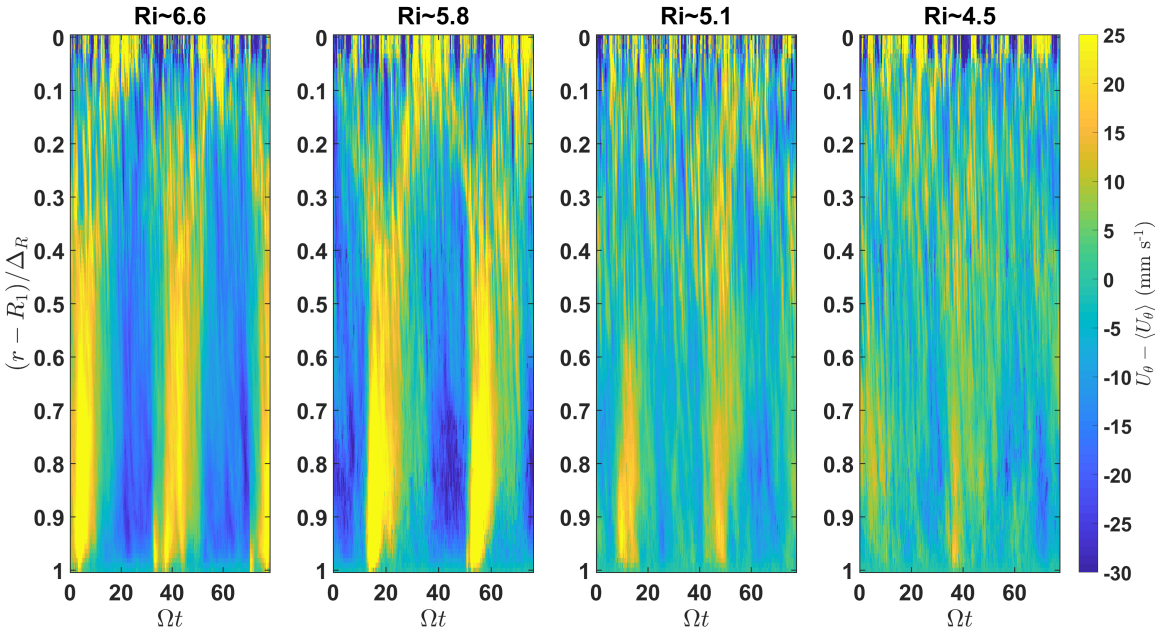


(a)

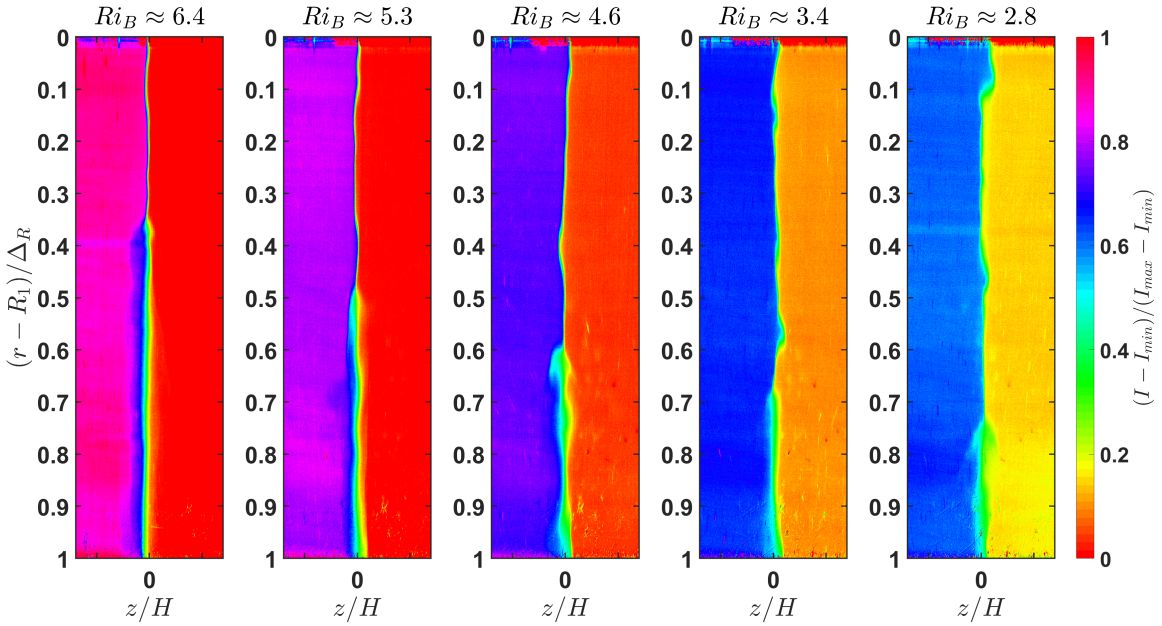


(b)

Fig. 3.19 $(a)$ Phase averaged azimuthal velocity perturbation time-series along a radial line with different reducing $Ri_B$. $(b)$ Snapshots at the instant just before the splashing at different reducing $Ri_B$.

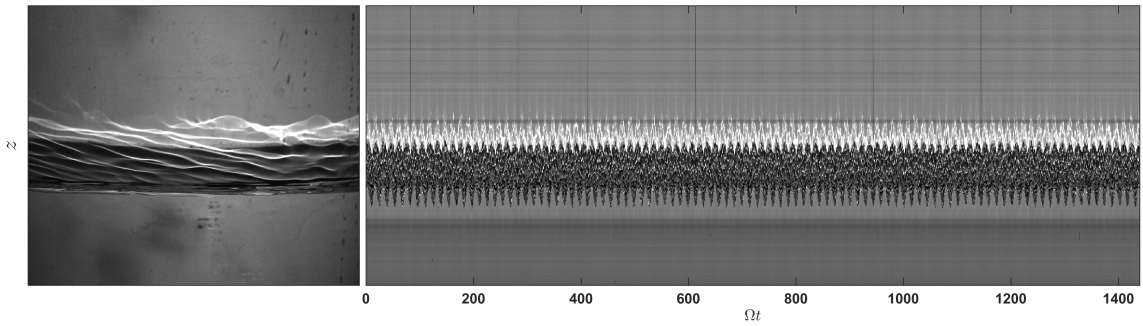


Fig. 3.20 Left: An actual recorded shadowgraph image. Right: Time-series of a vertical line from the recorded images. Parameters for the experiment shown are $Ri_B \sim 8$ and $Re = 18000$.

the outer cylinder. This suggests that for the fluid there is a critical height to which the mixed fluid in the inner boundary layer has to grow for it to have enough energy to work against the radial pressure gradient. Once it has gained enough energy, it moves out towards the outer cylinder by converting its potential energy into kinetic energy. It moves out on the interface as an intrusive gravity current with radial velocity $v \sim \sqrt{(g\Delta\rho/\rho_0)h}$. This velocity should be constant since $h \sim 1/\Delta\rho$. It is these parcels of fluid that are observed to be continuously being ejected from the inner boundary layer on the extremely sharp interface. Now with reducing $Ri_B$, the height $h$ for these parcels increases as $\Delta\rho$ reduces. Since the thickness of the boundary layer remains constant, this means that the overall volume of the fluid parcel being ejected increases with reducing $Ri_B$. This is consistent with our observations as well and can be seen in figure 3.19b where the parcels (represented by protrusions of mixed fluid) on the interface at lower $Ri_B$ are much bigger. These parcels are formed by mixing the fluid from the two layers, which means the density of these fluid parcels are the mean density of fluid in the layers (assuming layers are of equal height). This, in turn, means that the mass flux out from the inner boundary layer in the form of these parcels increases with reducing $Ri_B$ which are being entrained by the mixed fluid region in the middle of the annulus. This suggests that the overall energy ($\sim \frac{1}{2}\dot{m}v^2$, where $\dot{m}$ is the mass flux) being imparted into the mixed fluid region also increases with reducing $Ri_B$, which, in turn, means stronger splashing. We believe that it is this enhanced energy splashing that results in enhanced flux observed at low $Ri_B$.

## 3.5 STC with immiscible fluids

In this section, we look into instability for an STC experiment with immiscible fluids. The idea behind this experiment is to get a clearer picture of the above observed instability,

which will give us insights on the origin of this instability. The use of immiscible fluids meant higher interfacial surface tension at the interface. Since kelvin modes do exist with reduced amplitude in high interfacial surface tension flows (Vallis, 2017), we expect to see the periodic mixing mode as observed above for these experiments as well.

The two fluids used are Paraffin oil and glycerol (interfacial surface tension = 56 $\mathrm{mN\,m^{-1}}$). Glycerol is mixed with some water in order to make a solution with the same viscosity as that of Paraffin oil. The experiments are performed at four different speeds, $Re$ = 4500, 9000, 13500, 18000 and $Ri_B \sim 8$. The parameters are comparable to those used in the above experiments with miscible fluids ($Re = 14000$ and $Ri_B \sim 3-7$). The shadowgraph technique is used to visualise the instability (refer to section 5.2.1 for details), if any. Figure 3.20 shows one of the actual recorded images (left) and a time series of a vertical line from those recorded images, for the experiment with $Re = 18000$. The white line closely represents the interface, while the black zone is produced because of the bending of light due to the large density difference across the interface. The waves on the interface as seen in the left image in figure 3.20 shows that the flow is turbulent. There are peaks observed in the shadowgraph time-series. These peaks represent the rotation period of the inner cylinder.

The observed peaks are because of the higher pressure variations as the cylinder is made to run at high speed to achieve similar $Re$ and $Ri_B$ to the miscible experiments. No trace of the previously observed mixing mode is observed, which indicates that mixing is an important requirement of this instability to occur. This means that the non-linear interactions of the fluids as a result of mixing is a prerequisite condition for this instability to be observed.

## 3.6 Discussion

In this chapter, we have looked at the structure of the periodic mixing event that was observed by Oglethorpe (2014). We performed two-layer STC flow experiments with the conductivity probe measuring density at the interface at two different radial locations, one near the outer cylinder boundary and the other in the middle of the annulus. By using a FFT of the recorded density signal, we observed that the power of the mixing mode frequency is higher at the boundary than in the middle of the annulus, suggesting the previously observed periodic mixing event is associated with the boundaries, contradicting the mixing hypotheses provided by Oglethorpe (2014). We then looked at the structure of this observed mixing event on the interface using LIF in the $(r,z)$ plane. We find that the interface goes periodically through a series of events. The series of events can be seen in figure 3.8. It starts with an interface of constant thickness throughout the radial gap. An instability then develops and causes the formation of an extremely sharp interface with thickness $\sim 1\,\mathrm{mm}$, at both the cylinder

boundaries with a mixed fluid region in the middle. The extent of the sharp interface then grows further into the annulus at both cylinders. At the same time, constant ejections of fluid parcels from the inner cylinder boundary are observed to be travelling on the interface as a gravity current and are entrained in the mixed fluid in the middle of the annulus. This results in increased momentum injection into the mixed region which then starts to move outwards towards the outer cylinder boundary, resulting in a splash and forming a gravity current extending into both the layers. The vertical motions produced here result in most of the mixing. The stratification now starts to act and pushes the gravity current towards the interfaces which then travels on the interface towards the inner cylinder boundary, forming an interface of constant thickness again.

Further, we discuss the results of the simultaneous LIF and PIV experiments with a horizontal laser sheet at the interface. We observe a clear signal of presence of two azimuthal mode $m = 1$ boundary waves, one at each cylinder boundary, going around the annulus. It is this wave which causes the formation of the sharp interface at the boundaries and results in the above mentioned mixing process. From the PIV results, we find a periodic enhancement of azimuthal velocity during the splash.

Finally, we discuss the changing nature of the above observed instability with reducing $Ri_B$ and provide an interpretation of the enhanced flux observed at low $Ri_B$ (refer to figure 2.10). We find that with reducing $Ri_B$, the extent of the extremely sharp interface goes increasingly further into the annulus, resulting in a much smaller mixed fluid region. At the same time, the strength of the periodic enhancement of azimuthal velocity during the splashing process decreases with decreasing $Ri_B$. Further analysing the LIF and PIV data, we find that there are two phenomena that cause the vertical mixing. One is 'scouring', where the large scale turbulent eddies in each of the layers mix and homogenise any vertical fluid perturbation on the interface and the second is the 'splashing', which produces turbulent vertical fluid movement at the outer cylinder boundary. We have discussed the effects of reducing $Ri_B$ an both these mechanisms.

We observe that the interface thickness increases with reducing $Ri_B$ (see figure 3.17a). This means that the density gradient at the interface would reduce further than if it was just because of the reduction of $\Delta\rho$ across the interface with reducing $Ri_B$. This, in turn, means that the fluid parcels would now feel reduced resistance to the vertical motion. This results in enhanced flux due to scouring with reducing $Ri_B$. However, the extent of the extremely sharp interface extends further into the annulus with reducing $Ri_B$. Due to the extremely sharp density gradient, no mixing is observed due to scouring across the extremely sharp interface. Since, the extremely sharp interface exists through most of the mixing cycle, this means that significantly lesser area of the interface, on average, is available for scouring to

occur with reducing $Ri_B$. So here, the enhanced scouring flux due to reduced density gradient is balanced by the reduction of the surface area available for scouring to occur. This suggests that the enhanced buoyancy flux observed at low $Ri_B$ is possibly not because of 'scouring' flux.

As discussed above, the extent of the extremely sharp interface increases and the size of the mixed fluid region reduces, with reducing $Ri_B$. There are continuous ejections of high momentum fluid parcels from the inner boundary layer that are entrained into the the mixed fluid region. This pushes the mixed fluid region towards the outer cylinder and we observe a splash. With the reduced size of the mixed fluid region with reducing $Ri_B$, this would mean less resistance to high energy fluid parcels to reach the outer cylinder and cause a much stronger splash. This is also consistent with the observation of azimuthal velocity at reducing $Ri_B$. It is observed that the strength of the periodic enhancement of azimuthal velocity during the splashing process decreases with decreasing $Ri_B$. This suggests that most of the energy is used in producing vertical motion of fluid. We also looked at the energy arguments from the fluid parcels being ejected from the inner boundary layer, originally proposed by Oglethorpe (2014), and providing another interpretation of enhanced splashing at the outer cylinder with reducing $Ri_B$. We believe it is the enhanced splashing that results in enhanced flux observed at low $Ri_B$.

Lastly, we performed two-layer STC flow experiments with immiscible fluids and were not able to observe any trace of the above observed periodic instability, which suggests that either it is the high interfacial surface tension that suppresses the instability, or the mixing is important for this instability to exist. We believe it is the latter as instabilities have been previously observed in high interfacial surface tension flows.

# Chapter 4

# Linear Stability Analysis

## 4.1 Introduction

In this chapter, we look into the linear stability analysis of a two-layer stratified Taylor Couette flow.

As discussed earlier in chapter 1, there have been a few previous numerical studies who looked into the formation of layers and interfaces in a linearly stratified environment. Posmentier (1977) and later Barenblatt *et al.* (1993) numerically integrated the one dimensional diffusion equation for buoyancy and found that layers and interfaces develop in their simulations. They suggested a flux-$Ri_B$ relationship in which $R_f$ increases up to a maximum as $Ri_B$ increases from zero, then $R_f$ decreases towards zero as $Ri_B$ increases further, which was consistent with previous experiments. But later, Balmforth *et al.* (1998) found an issue with their simulations, in that their models allow the interface to sharpen indefinitely, leading to nonphysical discontinuities. They proposed a flux-$Ri_B$ relation in which $R_f$ increases with $Ri_B$ as $Ri_B$ increases from zero, then $R_f$ decreases with increasing $Ri_B$ down to a minimum, then $R_f$ increases again with further increase in $Ri_B$. Oglethorpe (2014) found this flux-$Ri_B$ relation to be inconsistent with her empirical observations. She used Balmforth *et al.*'s model and modelled the evolution of buoyancy using her empirical flux observations. She was able to observe layer formation and layer coarsening over time i.e. reduction in number of layers. But she observed layer coarsening by merger of interfaces, unlike that in experiments where the interfaces overturn, get mixed with the layers and disappears. Moreover, none of these studies were able to find empirically the observed layer heights.

There have also been some previous numerical studies on linearly stratified Taylor-Couette (STC) flow specifically. Yavneh *et al.* (2001) and Molemaker *et al.* (2001) were the first to discover a non-axisymmetric instability outside the domain of centrifugal instability set by Rayleigh's criterion (Rayleigh, 1917), which was later named as strato-rotational

instability (SRI) by Dubrulle *et al.* (2005). SRI was found to form as a result of resonance of two boundary trapped helicoidal modes. It was again confirmed in the numerical works of Rüdiger & Shalybkov (2009); Shalybkov & Rüdiger (2005). Park & Billant (2013) using linear stability and WKB asymptotic analysis came to a striking conclusion that the STC flow is always linearly unstable, the only exception being the case of solid body rotation. More recently, Leclercq *et al.* (2016*a*); Park *et al.* (2017) have performed linear stability analysis looking at the connection between centrifugal and strato-rotational instabilities in both centrifugally stable and unstable regimes. They found that the two instabilities can co-exist in the centrifugally stable domain region. Park *et al.* (2018) confirmed the same using both stability analysis and experiments. For all these studies, even when the *Re* was set high enough, the base flow used was a laminar Taylor-Couette flow profile which is not a correct representation of the actual empirical flow.

There have been only two other numerical studies studies on centrifugally unstable linear STC flow with a fixed outer cylinder (according to our knowledge). These studies have direct relevance to the experiments discussed in chapter 2 and chapter 3. Hua *et al.* (1997) reproduced the experiments of Boubnov *et al.* (1995) (who was the first one to experimentally visualise a non-axisymmetric instability in a turbulent STC with fixed outer cylinder) and found the primary instability to be axisymmetric and suggested that the observed instability is because of stable stratification suppressing the Taylor-rolls. Our experimental observations show a non-axisymmetric behaviour contradicting their result. Recently, Leclercq *et al.* (2016*b*) analysed the STC flow using linear analysis and direct numerical simulation. They suggested that the observed coherent structures were resulting from interactions between two helical modes of opposite handedness. Although they suggested that they have observed similar layer depths as empirically observed by Oglethorpe (2014), their observed azimuthal wavenumber was always greater than one, unlike that for our experiments. They, as well, used a laminar velocity profile for their linear stability analysis.

As discussed in chapter 3, we observe an instability on the interface in two-layer STC in the form of two boundary trapped waves moving around the annulus with azimuthal mode, $m = 1$. The observed time period for this instability depends only on the rotation speed of the inner cylinder and is independent of the density difference across the layers and height of fluid in the tank. The observations also strongly suggest that it is the flow phenomenon arising as a result of this instability that causes the dominant part of the mixing across the interface. The same instability is also observed on each of the interfaces formed in an initially linearly stratified STC flow as well. The fact that the instability is observed in a two-layer STC flow suggests that this instability does not require a linear gradient to form, and requires sharp density gradients for it to exist. We believe that there is another instability that forms

the sharp density gradients in an initially linearly stratified STC flow, on which the observed boundary trapped wave instability rides. It is possibly this instability that sets the layer height.

Furthermore, as discussed in section 3.5, no instability is observed for a two-layer STC experiments with immiscible fluids, which suggests that either $(a)$ it is the high interfacial surface tension that completely suppresses the instability, or $(b)$ it is because mixing is important for this instability to occur. If the latter scenario is true, it would mean that non-linear interactions in the flow ($\mathbf{u}.\nabla\mathbf{u}$ term of Navier-Stokes equation) are important prerequisite for this instability.

In this chapter, we look into linear stability analysis of a STC with a high density gradient interface and using the empirically observed mean velocity profile as the base flow. This is done in order to check if using linearised flow interactions, $\mathbf{u}.\nabla\mathbf{u}$ could give us more insights on the origin of the above observed instability. However, we are aware that using an empirical mean profile that is arising from a clearly turbulent flow, there is no reason for the instability predictions from the stability analysis to be relevant to what is experimentally observed. However, it would be very interesting if the predictions from such a turbulent mean flow do indeed agree with the observations.

## 4.2 Linear stability formulation

In this section, we drive the eigenvalue problem in order to look into the linear stability of the experimentally observed flow, from the governing equations.

In experiments shown in previous chapters, the annular region is filled with fluid to a finite height $H$, and the fluid is contained by the end-plates, both at the top and the bottom end at $z = \pm H/2$. There are two non-dimensional parameters that describe the apparatus geometry. They are the radius ratio $\eta$ and the aspect ratio $\Gamma$, and are defined as

$$\eta = \frac{R_1}{R_2} \qquad \text{and} \qquad \Gamma = \frac{H}{\Delta_R}, \tag{4.1}$$

where $R_1$ and $R_2$ are the radii of the inner and outer cylinder respectively and $\Delta_R = R_2 - R_1$ is the annular gap width. The inner cylinder is made to rotate at rotation speed $\Omega$ while the outer cylinder is stationary and the radial shear is characterised by a Reynolds number $Re$, given by

$$Re = \frac{\Omega R_1 \Delta_R}{\nu} \tag{4.2}$$

where $\nu$ is the kinematic viscosity of the fluid. The density stratification in the two layer experiments is initially set up with a sharp interface in the middle. The strength of the forcing due to this stratification is characterised by a bulk Richardson number $Ri_B$, defined as

$$Ri_B = \frac{g\Delta\rho}{\rho_0}\frac{R_2}{(\Omega R_1)^2} \tag{4.3}$$

where $g$ is the acceleration due to gravity, $\rho_0$ is the reference density and $\Delta\rho$ is

$$\Delta\rho = \bar{\rho}(z - H/2) - \bar{\rho}(z + H/2)$$

where $\bar{\rho}$ is the density profile at time, $t = 0$. The relative diffusion of the scalar field compared to the molecular diffusion is characterised by a Schmidt number, defined as

$$Sc = \frac{\nu}{\kappa} \tag{4.4}$$

where $\kappa$ is the coefficient of diffusion of the scalar, which is salt in our experiments.

We use the incompressible Navier-Stokes equations under the Boussinesq approximation to model the above empirical flow. The governing equations for velocity, $\mathbf{u} = u_r\ \mathbf{e_r} + u_\theta\ \mathbf{e}_\theta + u_z\ \mathbf{e_z}$, in their non-dimensional form are the following,

$$\nabla\ .\ \mathbf{u} = 0\ , \tag{4.5a}$$

$$\partial_t \mathbf{u} + \mathbf{u}\ .\ \nabla\mathbf{u} = -\nabla p + \frac{1}{Re}\nabla^2\mathbf{u} - Ri^*\ \rho'\mathbf{e_z}\ , \tag{4.5b}$$

$$\partial_t \rho + \mathbf{u}\ .\ \nabla\rho + w\ \partial_z\bar{\rho} = \frac{1}{Re\ Sc}\nabla^2\rho\ , \tag{4.5c}$$

where $\rho'$ is the perturbation density, $p$ is the pressure and

$$Ri^* = \frac{1-\eta}{2}Ri_B\ .$$

Here the chosen length scale, velocity scale and density scale for non-dimensionalisation are $\Delta_R$, $\Omega R_1$ and $\Delta\rho/2$ respectively.

We assume the base flow to be purely azimuthal $\bar{\mathbf{U}} = V(r)\ \mathbf{e}_\theta$ and the base density to be varying only in the axial direction, $\bar{\rho} = \bar{\rho}(z)$. To note here that the base flow being used here corresponds to the empirical mean of the turbulent flow. This is consistent with our experimental observations. It is worth noting here that the base velocity profile is a function of $r$ and the base density profile is a function of $z$. Having base flow dependence on both $r$ and $z$ makes this stability problem extremely challenging.

Now we superimpose infinitesimal perturbations on the base flow quantities and insert those to (4.5) and linearise the equations. Following are the linearised Boussinesq Navier-Stokes equations, where $u', v', w', p', \rho'$ are the radial velocity, azimuthal velocity, axial velocity, pressure and density perturbation respectively:

$$\partial_t u' + \frac{1}{r}\bar{V}\partial_\theta u' - \frac{2}{r}\bar{V}v' = -\partial_r p' + \frac{1}{Re}(\nabla^2 u' - \frac{u'}{r^2} - \frac{2}{r^2}\partial_\theta v') \ , \tag{4.6}$$

$$\partial_t v' + \frac{1}{r}\bar{V}\partial_\theta v' + \frac{u'}{r}\partial_r(r\bar{V}) = -\frac{1}{r}\partial_\theta p' + \frac{1}{Re}(\nabla^2 v' - \frac{v'}{r^2} + \frac{2}{r^2}\partial_\theta u') \ , \tag{4.7}$$

$$\partial_t w' + \frac{1}{r}\bar{V}\partial_\theta w' = -\partial_z p' + \frac{1}{Re}\nabla^2 w' - Ri^*\rho' \ , \tag{4.8}$$

$$\partial_t \rho' + \frac{1}{r}\bar{V}\partial_\theta \rho' + w'\partial_z\bar{\rho} = \frac{1}{Re\,Sc}\nabla^2\rho' \ , \tag{4.9}$$

$$\frac{1}{r}\partial_r(ru') + \frac{1}{r}\partial_\theta v' + \partial_z w' = 0 \ . \tag{4.10}$$

Now, upon taking $[\frac{1}{r}\partial_r(r\,4.6) + \frac{1}{r}\partial_\theta(4.7) + \partial_z(4.8)]$, the temporal and viscous terms go to zero using (4.10), and we get

$$\begin{aligned}
-\nabla^2 p' - Ri^*\partial_z\rho' &= \frac{1}{r}\partial_r(\bar{V}\partial_\theta u' - 2\bar{V}v') + \frac{1}{r}\partial_\theta(\frac{1}{r}\bar{V}\partial_\theta v' + u'\partial_r\bar{V} + \frac{\bar{V}u'}{r}) + \partial_z(\frac{1}{r}\bar{V}\partial_\theta w') \\
&= \frac{1}{r}\bar{V}\partial_{r\theta}u' + \frac{1}{r}\partial_r\bar{V}\partial_\theta u' - \frac{2}{r}\bar{V}\partial_r v' - \frac{2}{r}v'\partial_r\bar{V} + \frac{1}{r^2}\bar{V}\partial_{\theta\theta}v' + \frac{1}{r}\partial_r\bar{V}\partial_\theta u' \\
&\quad + \frac{\bar{V}}{r^2}\partial_\theta u' + \frac{1}{r}\bar{V}\partial_{\theta z}w' \\
&= \frac{1}{r}\bar{V}\partial_\theta(-\frac{u'}{r}) + \frac{1}{r}\partial_r\bar{V}\partial_\theta u' - \frac{2}{r}\partial_r(\bar{V}v') + \frac{1}{r}\partial_r\bar{V}\partial_\theta u' + \frac{\bar{V}}{r^2}\partial_\theta u' \\
&= \frac{2}{r}(\partial_r\bar{V}\partial_\theta u' - \partial_r(\bar{V}v')) \ .
\end{aligned} \tag{4.11}$$

Now, taking the Laplacian of (4.6) and then using (4.11) to remove $p'$, we get

$$\begin{aligned}\partial_t(\nabla^2 u' - \frac{u'}{r^2} - \frac{2}{r^2}\partial_\theta v') = & -\frac{\bar{V}}{r}\nabla^2(\partial_\theta u') + \frac{2}{r^2}\bar{V}\partial_{r\theta}u' + \frac{2}{r^3}\bar{V}\partial_\theta u' + \frac{1}{r}(\partial_{rr}\bar{V} + \frac{\partial_r\bar{V}}{r})\partial_\theta u' \\ & + \frac{2}{r}\bar{V}(\partial_{zz}v' + \frac{2}{r^2}\partial_{\theta\theta}v') \\ & + Ri^*\partial_{rz}\rho' \\ & + \frac{1}{Re}(\nabla^4 u' - \frac{2}{r^2}\partial_{zz}u' - \frac{2}{r^2}\partial_{rr}u' - \frac{6}{r^4}\partial_{\theta\theta}u' + \frac{2}{r^3}\partial_r u' - \frac{3}{r^4}u' \\ & - \frac{4}{r^2}\partial_{rr\theta}v' - \frac{4}{r^2}\partial_{\theta zz}v' + \frac{4}{r^3}\partial_{r\theta}v' - \frac{4}{r^4}\partial_{\theta\theta\theta}v' - \frac{4}{r^4}\partial_\theta v') \ .\end{aligned} \tag{4.12}$$

Similarly, taking the Laplacian of (4.8) and again using (4.11) to remove $p'$, we get

$$\begin{aligned}\partial_t(\nabla^2 w') = & -\frac{\bar{V}}{r}\nabla^2\partial_\theta w' + \frac{2}{r^2}\bar{V}\partial_{r\theta}w' - \frac{2}{r}\partial_r\bar{V}\partial_{r\theta}w' - \frac{\bar{V}}{r^3}\partial_\theta w' - \frac{1}{r}(\partial_{rr}\bar{V} - \frac{\partial_r\bar{V}}{r})\partial_\theta w' \\ & + \frac{2}{r}(\partial_r\bar{V}\partial_{\theta z}u' - \bar{V}\partial_{rz}v' - \partial_r\bar{V}\partial_z v') \\ & + Ri^*(\partial_{zz}\rho' - \nabla^2\rho') \\ & + \frac{1}{Re}\nabla^4 w' \ .\end{aligned} \tag{4.13}$$

Note here

$$\begin{aligned}\nabla^2 \equiv & \ \partial_{rr} + \frac{1}{r}\partial_r + \frac{1}{r^2}\partial_{\theta\theta} + \partial_{zz} \ , \text{and} \\ \nabla^4 \equiv & \ \partial_{rrrr} + \frac{1}{r^4}\partial_{\theta\theta\theta\theta} + \partial_{zzzz} + 2\partial_{rrzz} + \frac{2}{r^2}\partial_{rr\theta\theta} + \frac{2}{r^2}\partial_{\theta\theta zz} + \frac{2}{r}\partial_{rrr} + \frac{2}{r}\partial rzz - \frac{2}{r^3}\partial_{r\theta\theta} \\ & - \frac{1}{r^2}\partial_{rr} + \frac{4}{r^4}\partial_{\theta\theta} + \frac{1}{r^3}\partial_r \ .\end{aligned}$$

Now we assume that each perturbation variable has a wavelike behaviour in the azimuthal direction, and can be written as

$$(u', v', w', \rho') = [u(r,z), v(r,z), w(r,z), \rho(r,z)]e^{im\theta+\sigma t} \ . \tag{4.14}$$

Now from (4.10),

$$v = \frac{ir}{m}(\partial_r u + \frac{u}{r} + \partial_z w) \ . \tag{4.15}$$

Inserting (4.14) and (4.15) in (4.12), we obtain

$$\begin{aligned}\sigma[(\nabla^2+\frac{2}{r}\partial_r+\frac{1}{r^2})u+\frac{2}{r}\partial_z w] = [&\frac{im}{r}\bar{V}(-\nabla^2+\frac{2}{r}\partial_r+\frac{2}{r^2})+\frac{im}{r}(\partial_{rr}\bar{V}+\frac{\partial_r\bar{V}}{r})]u\\ &+\frac{2i}{m}\bar{V}(\partial_{zzr}+\frac{1}{r}\partial_{zz}-\frac{2m^2}{r^2}\partial_r-\frac{2m^2}{r^3})u\\ &+\frac{2i}{m}\bar{V}(\partial_{zzz}-\frac{2m^2}{r^2}\partial_z)w\\ &+Ri^*\partial_{rz}\rho\\ &+\frac{1}{Re}[(\nabla^4-\frac{2}{r^2}\partial_{zz}-\frac{2}{r^2}\partial_{rr}+\frac{6m^2}{r^4}+\frac{2}{r^3}\partial_r-\frac{3}{r^4})u\\ &+\frac{4}{r}(\partial_{rrr}+\partial_{rzz}+\frac{1}{r}\partial_{zz}-\frac{2+m^2}{r^2}\partial_r+\frac{4-m^2}{r^3})u\\ &+\frac{4}{r}(\partial_{zzz}+\partial_{rrz}-\frac{1}{r}\partial_{rz}-\frac{m^2-1}{r^2}\partial_z)w]\ .\end{aligned} \tag{4.16}$$

Similarly, inserting (4.14) and (4.15) in (4.13),

$$\begin{aligned}\sigma\nabla^2 w = [&\frac{im}{r}\bar{V}(-\nabla^2+\frac{2}{r}\partial_r-\frac{1}{r^2})+\frac{im}{r}(\frac{\partial_r\bar{V}}{r}-2\partial_r\bar{V}\partial_r-\partial_{rr}\bar{V})-\frac{2i}{m}\bar{V}(\partial_{rzz}+\frac{1}{r}\partial zz)\\ &-\frac{2i}{m}\partial_r\bar{V}\partial_{zz}]w\\ &+[-\frac{2i}{m}\bar{V}(\partial_{rrz}+\frac{2}{r}\partial_{rz})-\frac{2i}{m}(\partial_r\bar{V}\partial_{rz}-\frac{m^2-1}{r}\partial_r\bar{V}\partial_z)]u\\ &+Ri^*(\partial_{zz}-\nabla^2)\rho\\ &+\frac{1}{Re}\nabla^4 w\ .\end{aligned} \tag{4.17}$$

Here we have removed $p'$ and $v'$ from (4.6) - (4.10), and have reduced those equations to the following eigenvalue problem for the vector $[u,w,\rho]^T$:

$$\sigma\begin{bmatrix}A_U & A_{UW} & \\ & A_W & \\ & & A_{Rho}\end{bmatrix}\begin{bmatrix}u\\w\\\rho\end{bmatrix}=\begin{bmatrix}B_U & B_{UW} & B_{URho}\\ B_{WU} & B_W & B_{WRho}\\ & B_{RhoW} & B_{Rho}\end{bmatrix}\begin{bmatrix}u\\w\\\rho\end{bmatrix} \tag{4.18}$$

where

$$A_U := \nabla^2 + \frac{2}{r}\partial_r + \frac{1}{r^2} \tag{4.19a}$$

$$A_{UW} := \frac{2}{r}\partial_z \tag{4.19b}$$

$$A_W := \nabla^2 \tag{4.19c}$$

$$A_{Rho} := \mathscr{I} \tag{4.19d}$$

$$\begin{aligned} B_U := {} & \frac{im}{r}\bar{V}(-\nabla^2 + \frac{2}{r}\partial_r + \frac{2}{r^2}) + \frac{im}{r}(\partial_{rr}\bar{V} + \frac{\partial_r \bar{V}}{r}) \\ & + \frac{2i}{m}\bar{V}(\partial_{zzr} + \frac{1}{r}\partial_{zz} - \frac{2m^2}{r^2}\partial_r - \frac{2m^2}{r^3}) \\ & + \frac{1}{Re}[(\nabla^4 - \frac{2}{r^2}\partial_{zz} - \frac{2}{r^2}\partial_{rr} + \frac{6m^2}{r^4} + \frac{2}{r^3}\partial_r - \frac{3}{r^4}) \\ & + \frac{4}{r}(\partial_{rrr} + \partial_{rzz} + \frac{1}{r}\partial_{zz} - \frac{2+m^2}{r^2}\partial_r + \frac{4-m^2}{r^3})] \end{aligned} \tag{4.19e}$$

$$\begin{aligned} B_{UW} := {} & \frac{2i}{m}\bar{V}(\partial_{zzz} - \frac{2m^2}{r^2}\partial_z) \\ & + \frac{1}{Re}\frac{4}{r}(\partial_{zzz} + \partial_{rrz} - \frac{1}{r}\partial_{rz} - \frac{m^2-1}{r^2}\partial_z) \end{aligned} \tag{4.19f}$$

$$B_{URho} := Ri^*\partial_{rz} \tag{4.19g}$$

$$B_{WU} := -\frac{2i}{m}\bar{V}(\partial_{rrz} + \frac{2}{r}\partial_{rz}) - \frac{2i}{m}(\partial_r\bar{V}\partial_{rz} - \frac{m^2-1}{r}\partial_r\bar{V}\partial_z) \tag{4.19h}$$

$$\begin{aligned} B_W := {} & \frac{im}{r}\bar{V}(-\nabla^2 + \frac{2}{r}\partial_r - \frac{1}{r^2}) + \frac{im}{r}(\frac{\partial_r\bar{V}}{r} - 2\partial_r\bar{V}\partial_r - \partial_{rr}\bar{V}) \\ & - \frac{2i}{m}\bar{V}(\partial_{rzz} + \frac{1}{r}\partial_{zz}) - \frac{2i}{m}\partial_r\bar{V}\partial_{zz} + \frac{1}{Re}\nabla^4 w \end{aligned} \tag{4.19i}$$

$$B_{WRho} := Ri^*(\partial_{zz} - \nabla^2) \tag{4.19j}$$

$$B_{RhoW} := -\partial_z\bar{\rho} \tag{4.19k}$$

$$B_{Rho} := -\frac{im}{r}\bar{V} + \frac{1}{Re\,Pr}\nabla^2 \tag{4.19l}$$

Here $\mathscr{I}$ is the identity matrix.

We tackle this temporal stability problem by specifying the azimuthal wavenumber $m > 0 \in \mathbb{I}$ and solve (4.18) using MATLAB eig function to find the growth rate $\sigma \in \mathbb{C}$ and

eigenfunctions $[u, w, \rho] \in \mathbb{C}$. $Re(\sigma) > 0$ gives the unstable modes and their $Im(\sigma)$ corresponds to the frequency of the perturbation for those respective modes. The eigenfunction for $v$ is calculated using (4.15).

### 4.2.1 Boundary Conditions

The $(r,z)$ domain for solving (4.18) is discretised using Chebyshev collocation points in both the radial $r$ and axial direction $z$. We created the Chebyshev differentiation matrices, as explained in Trefethen (2000) to solve (4.18). We impose the no-slip boundary conditions on these matrices for velocity perturbation, $u = w = 0$ at $r,z = \pm 1$ representing the rigid and impermeable cylinder boundaries and the top and bottom end walls in the experiment. In order to also impose $v = 0$ at $r,z = \pm 1$, (4.15) requires us to to further impose $\partial_r u = 0$ at $r = \pm 1$ and $\partial_z w = 0$ at $z = \pm 1$. These clamped boundary conditions (both Neumann and Dirichlet boundary conditions) are imposed using methods also explained in Trefethen (2000).

In experiments, there is no salt flux out of the system. Hence a no-flux boundary condition for density perturbations is imposed i.e. $\partial_r \rho = 0$ at $r = \pm 1$ and $\partial_z \rho = 0$ at $z = \pm 1$. Now, the no-slip boundary condition is implemented by truncating the end rows and columns of the differentiation matrix, reducing the overall size of the matrix. In order to implement boundary conditions on the density perturbations and have a reduced size of the differentiation matrix as well (for it to be consistent with the differentiation matrices for the velocity perturbation), the technique explained by Dr. Ĵerôme Hoepffner in Hoepffner (2007) is used. A resolution of $M \times N$ requires solving a $(3 \times ((M-2) \times (N-2))^2)^2$ eigenvalue problem, making it quite computationally expensive.

### 4.2.2 Initial Conditions

The experiments on a two-layer STC flow, discussed in chapter 3, were performed at $Re = 14000$ with a starting $Ri_B \sim 7$. The high $Re$ ensured that the flow was turbulent which in the mean azimuthal flow profile can be seen in figure 3.10 where the angular momentum is constant in the bulk of the annulus (consistent with Lewis & Swinney (1999)). For all these experiments, the tank was filled to a height such that aspect ratio is $\Gamma = 3$.

Now for the linear stability analysis, we perform the calculations at $Re = 1000$, 3000, 5000 and at varying $Ri_B$. The Taylor-Couette flow is in the regime of turbulent Taylor vorticies at these $Re$ (Grossmann *et al.*, 2016). With present available computational resources, it was not feasible for us to increase $Re$ any further. This will be discussed in more detail in

subsequent sections. The $Sc$ for all calculations is set to $Sc = 700$, consistent with that of salt solution which was used in our experiments.

We assumed the base flow for our calculations to be purely azimuthal $\bar{\mathbf{U}} = V(r)\,\mathbf{e}_\theta$, even with the presence of end-plates. Ideally, to be completely consistent with the experiment, it would require us to have the base flow with dependence on both $r$ and $z$, but getting the exact base flow in $(r,z)$ plane is beyond the scope of the present experimental setup. At the same time, we believe that the assumption is justified for the following reasons. We have performed experiments with varying $\Gamma$ (discussed in the next chapter), and the observed instability seems to be the same for all cases. This is also observed in the works of Oglethorpe (2014). This means that for an experiment with large $\Gamma$, the effect of the end-wall that is felt near the interface would be negligible and the mean flow near the interface would be purely azimuthal. Moreover, in an initially linearly stratified STC flow, the interfaces are spontaneously formed with fully turbulent well-mixed layers around each interface. This would mean that each so-formed interface, on which the mode $m = 1$ instability exists, sees a purely azimuthal flow in both layers around it, consistent with our assumption. Furthermore, it is also interesting to note that each of the adjacent interfaces, to a good approximation, acts as a wall for the velocity perturbations, again consistent with the present geometry for our stability analysis.

As discussed in the previous section, solving the eigenvalue problem (4.15) is very computationally expensive. So in order to save on computation cost, most of the present stability calculations are performed for $\Gamma = 1$, while it being $\Gamma = 3$ for experiments shown so far which we are trying to model. However, as also discussed above, the aspect ratio $\Gamma$ does not seem to have an effect on the origin of this instability. This is consistent with the fact that the well-mixed layer height around the interface, formed in an initially linearly stratified STC flow case, is small, yet the $m = 1$ instability sill exists on those interfaces.

From the discussions in the previous two paragraphs, it seems like our present stability analysis is a good representation of analysis of the interfaces formed in a linear STC. However, we also did perform a few calculations for $\Gamma = 2$ as well. The results for those will also be discussed in subsequent sections.

Figure 4.1a shows the turbulent velocity profiles that are used as the base flow in the present stability analysis. The yellow profile is the best-fit to the mean azimuthal flow profiles from our experiments (refer to figure 3.10), with boundary layers drawn to it. These experiments were performed with an apparatus of $\eta = 0.417$. The blue profile is the azimuthal flow profile from the highly resolved PIV experiments on unstratified Taylor-Couette flow by Huisman *et al.* (2013). Their experiments were performed at a much higher $Re$ compared to our experiments, $Re \sim 10^6$ and at $\eta = 0.7$ and describe the boundary layer profile as

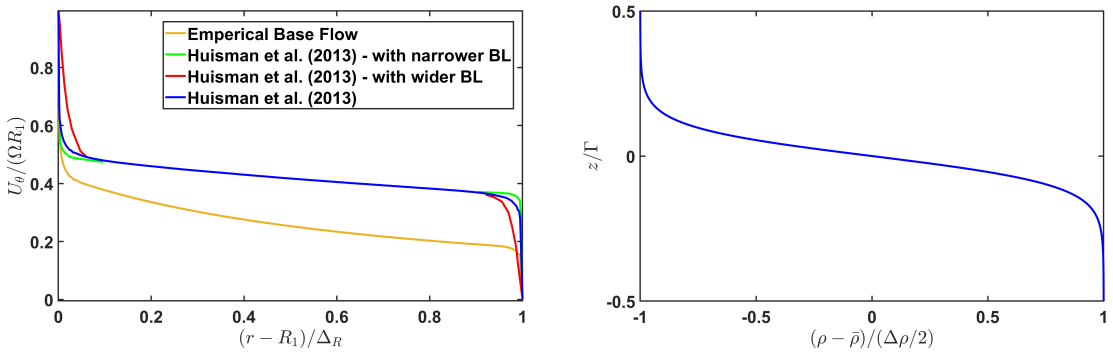


(a) (b)

Fig. 4.1 $(a)$ Plot showing the azimuthal velocity profiles that were used as the base flow in the linear stability analysis. The yellow curve is the mean azimuthal velocity profile from our PIV experiments (figure 3.10) with arbitrary smooth boundary layer profiles added to it. The blue curve shows the mean azimuthal profile observed in experiments of Huisman *et al.* (2013) at $Re \sim 10^6$. The red and green curves are same as the blue curve but with different boundary layer thickness. $(b)$ Plot shows the density profile that is used as the base density in the stability analysis.

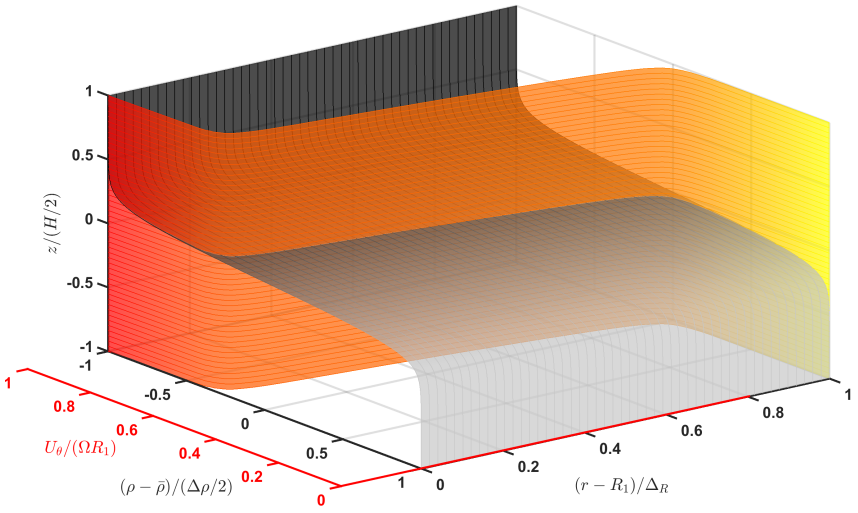


Fig. 4.2 Three dimensional visualisation of the base density profile and empirical base velocity profile over the complete $r-z$ grid.

well. The profile is discretised from figure 2 of their paper. These profiles were taken in experiments with specific radial geometry (i.e. specific $\eta$). The non-dimensional flow profiles would remain the same in the major bulk of the flow as $\eta$ is changed (Oglethorpe, 2014) but the non-dimensional thickness of the boundary layers would vary. The red and green profiles are exactly the same as the blue profile in the middle bulk of the flow, but with wider and narrower boundary layer to it respectively. Since we do not have the exact boundary layer profiles at different $\eta$, we use the same empirical base flow profile to study the stability for all $\eta$. In order to understand the consequences of using the same flow profile at different $\eta$, we analyse the stability at a specific $\eta$ for base profiles with varying arbitrary boundary layers (red and green curve in figure 4.1a) and compare it to the results for the profile with known boundary layers at that $\eta$ (blue curve in figure 4.1a). We find that varying the boundary layer thickness has negligible effect on the stability of the flow, and will be discussed in more detail in section 4.3.

Figure 4.1b shows the density profile that is used in the analysis. The same base density profile is imposed at all radial locations. The interface here is thicker than that observed in the experiments. This is done in order to have a check on the computational cost. The Chebyshev collocation points are finely spaced near the end-walls but quite sparsely spaced near the middle where the interface was present. In order to resolve the shown density profile, the resolution used in the axial direction was four times that in the radial direction. The interface being any sharper would have required even higher resolution to be able to resolve the interface and it is beyond the scope of present available computational resources.

### 4.2.3 Validation

The author was able to find two previous linear stability studies on Taylor-Couette flow with end walls. But we were not able to use either of these to validate our code, as discussed below. Avila *et al.* (2008) look at the stability of the flow in an unstratified Taylor-Couette flow with both cylinders rotating at same speed and stationary end-walls. Another work by Leclercq *et al.* (2016*c*) looked at the stability of centrifugally unstable Taylor-Couette flow with linearly stratified layers at the top and bottom third of tank and unstratified layer in the middle. They found that the presence of these stratified layers can mitigate the end-wall effects that are felt in the middle unstratified layer. In any case, for both of these stability studies, they performed DNS of the flow as well and used the flow profile obtained from DNS (varying in both radial and axial direction) as their base flow. We derive our equations with an assumption that flow is purely azimuthal. Hence, the results from solving the eigenvalue problem (4.18) could not be validated with those from the above studies.

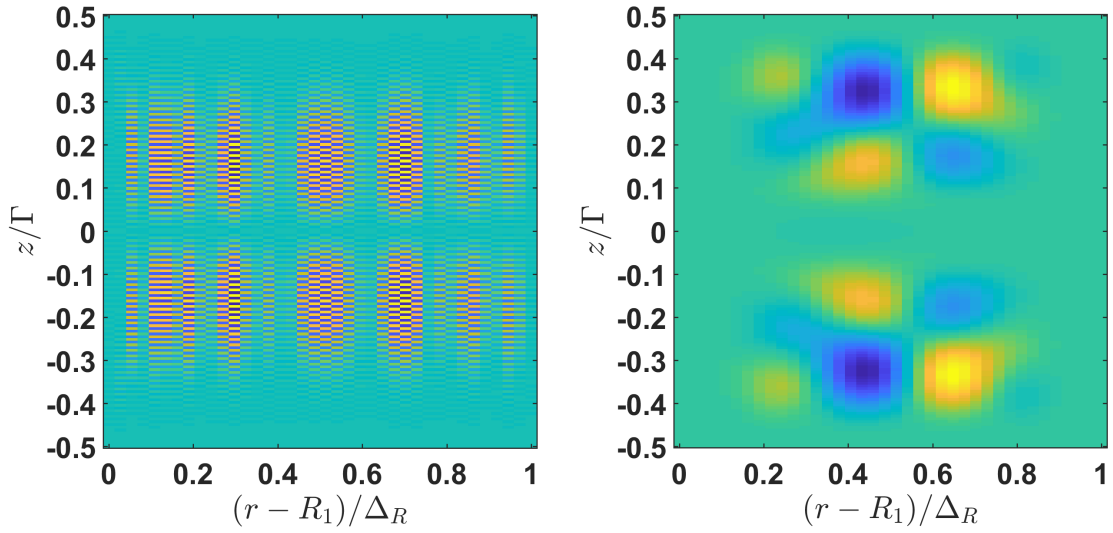


Fig. 4.3 Plot showing comparison of real part of radial velocity perturbation eigenfunction for a spurious (left) and a non-spurious (right) mode. The spurious modes have a high frequency oscillation and can be easily identified.

Now in order to ensure that the code is working, we ensure that the solution is fully converged and the eigenfunctions follow the boundary conditions. We still did find some spurious modes, but those were easy to identify by looking at the eigenfunctions. Figure 4.3 shows the real part of radial velocity eigenfuction for a spurious and a non-spurious mode. Clear high frequency oscillations are seen on a spurious eigenfunctions and those modes are ignored. The number of spurious modes decrease with increasing resolution.

Next we perform our calculations at resolutions where the solution has completely converged. To check this, we plotted the spectrum of non-spurious eigenvalues, $\sigma$ obtained with increasing resolution at three different Reynolds number, $Re$ = 1000, 3000 and 5000, as can be seen in figure 4.4. The calculations were made at $\eta = 0.9$ and $\eta = 0.417$ (same as in our experiments) and keeping $m = 1$. For $Re = 1000$, the eigenvalues seem to be converged at a radial resolution of 35 for both $\eta$. Axial resolution for all stability calculations is kept to be four times that in the radial direction. Similarly, for $Re = 3000$, the solution seem to be well converged at the radial resolution of 45. For $Re = 5000$, the solution seems to be converging at a radial resolution of 50, but due to time limitations, we were not able to run it at even higher resolution. It is useful to note here that, although not completely converged (as

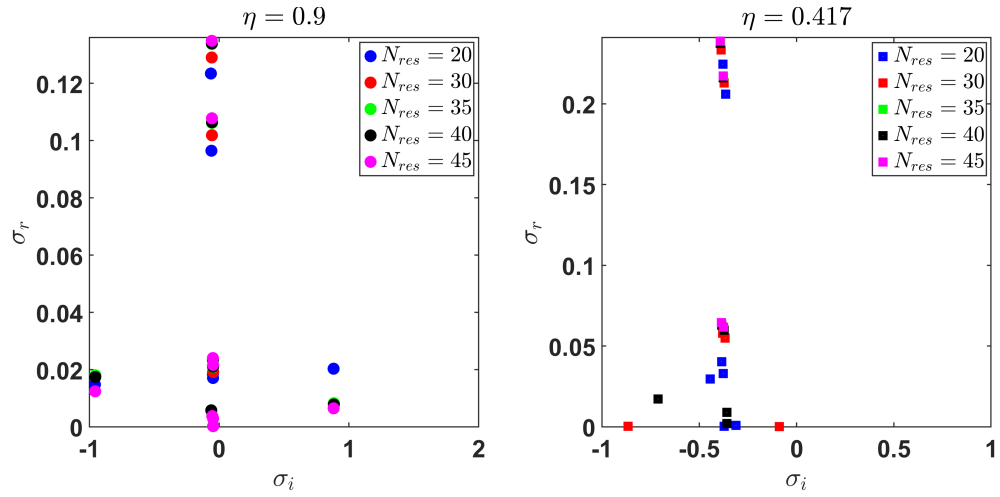


(a)

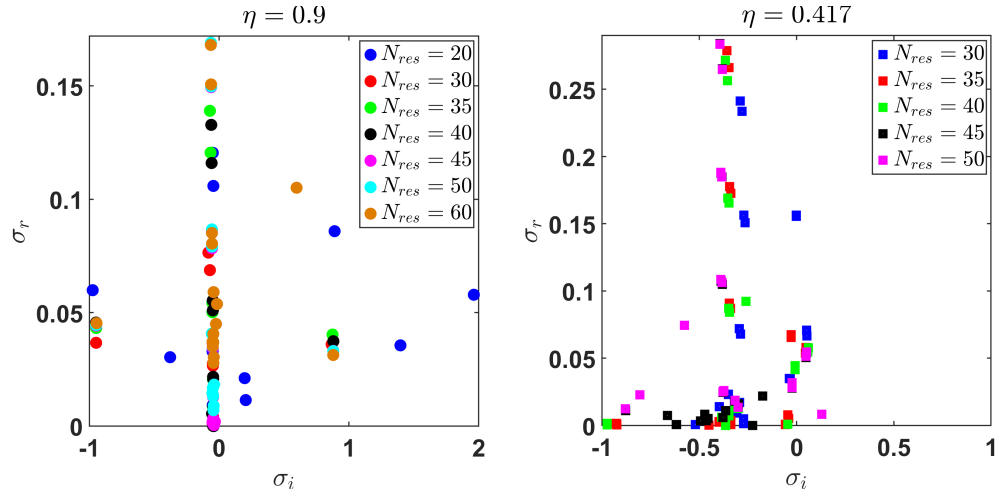


(b)

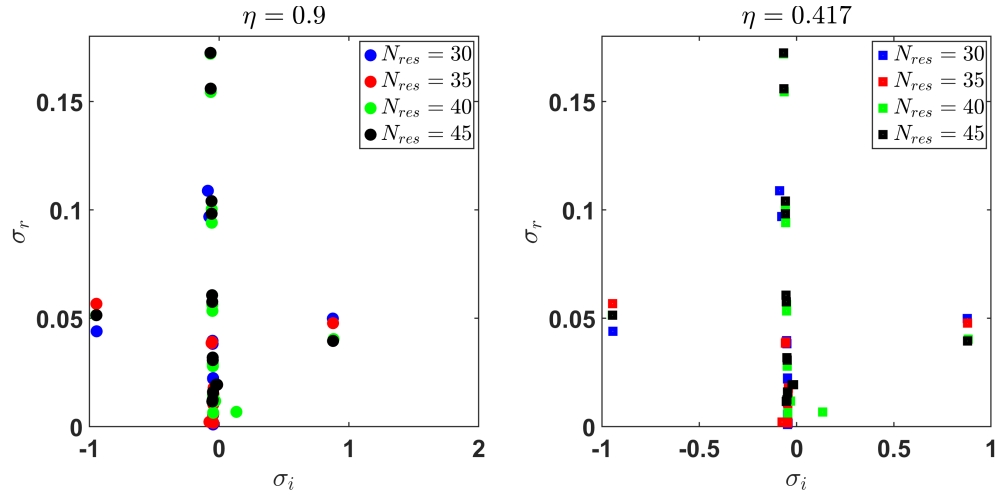


(c)

Fig. 4.4 Spectrum of all the unstable eigenvalues for $\eta = 0.9$ (left) and $\eta = 0.417$ (right) at different resolutions for $(a)$ $Re = 1000$, $(b)$ $Re = 3000$ and $(c)$ $Re = 5000$.

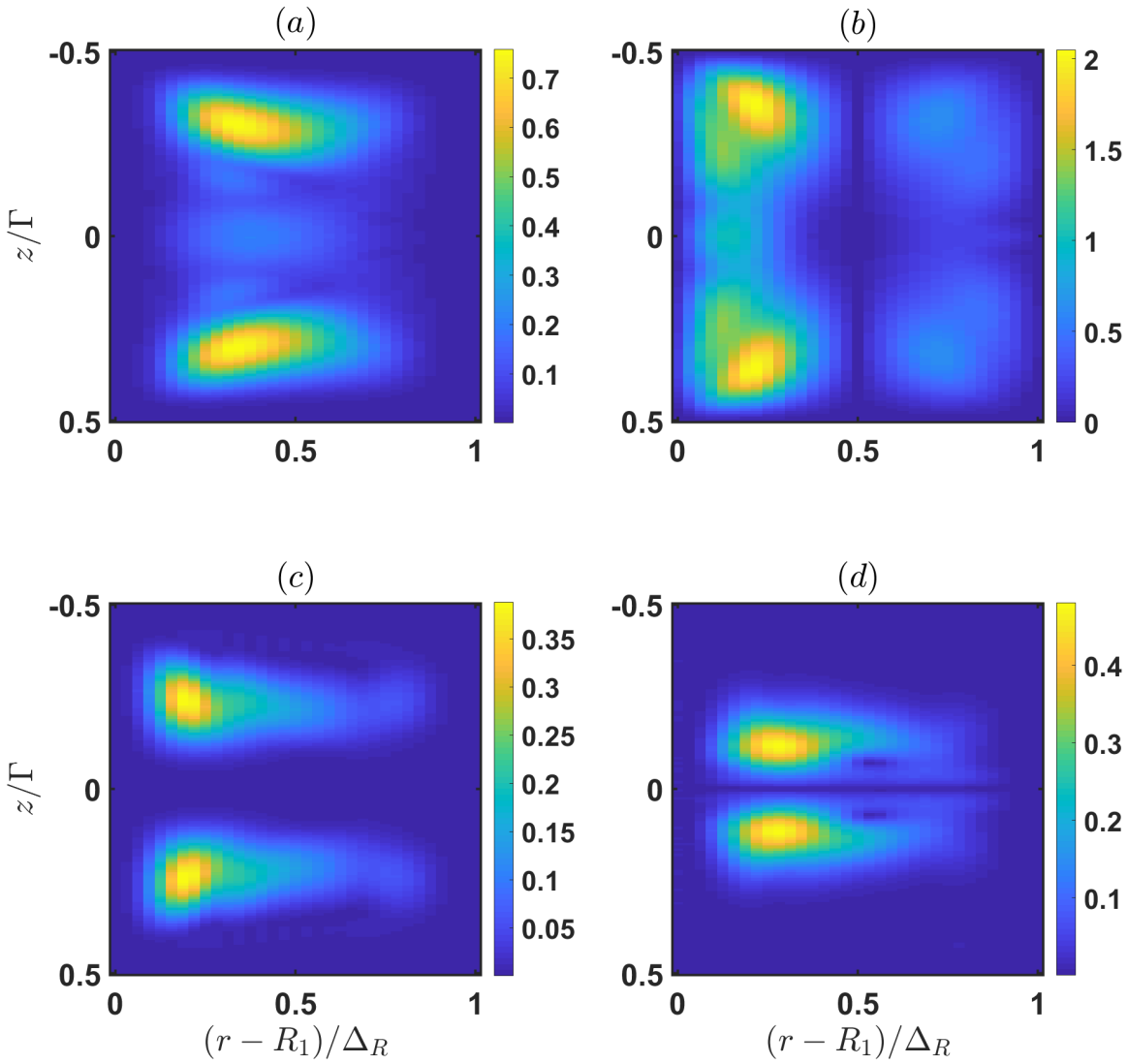


Fig. 4.5 Plot showing the absolute value of eigenfunctions of the most unstable mode at $m = 1$, for $(a)$ radial velocity perturbation, $(b)$ azimuthal velocity perturbation, $(c)$ axial velocity perturbation and $(d)$ density perturbation, solved at $Re = 1000$, $Ri_B = 6$ and $\eta = 0.4$ using the empirical base flow.

the eigenvalues do not completely overlap), we choose the radial resolution of 45 to perform analysis at $Re = 5000$ as it is very computationally and time expensive for higher resolution. Note that from here onward in this chapter, the stability calculation at $Re = 1000$, 3000 or 5000 is performed at radial resolution of 35, 45 and 45, unless specified otherwise.

Figure 4.5 show absolute value of the radial velocity perturbation ($u$), azimuthal velocity perturbation ($v$), axial velocity perturbation ($w$) and density perturbation ($\rho$) eigenfunctions for stability analysis at $Re = 1000$, $Ri_B = 6$ and $\eta = 0.417$. The azimuthal velocity eigenfunction is calculated using (4.15). It can be seen that the no-slip and boundary conditions are well satisfied for all velocities and density perturbation eigenfunctions (no-slip and no-penetration for $u$ and $w$, no-slip for $v$, and no-flux for $\rho$). It is worth noting that the eigenfunctions at higher $Re$, keeping all other parameters the same, look very similar but have different growth rates. Hence, in subsequent sections, unless comparing eigenfunctions with different parameters, we plot only the eigenfunctions at $Re = 1000$. Another reason for this is the fact that we are able to achieve full convergence of eigenvalue with no spurious modes at the resolution we perform our calculations for $Re = 1000$.

## 4.3 Observations and Analysis

### 4.3.1 Laminar vs Turbulent base flow

As discussed in section 4.1, the previous stability studies on stratified Taylor-Couette (TC) have assumed a laminar Taylor-Couette flow profile (refer to equation 5.1) as their base flow. As observed in our experiments, the turbulent flow profile in a TC flow is very different from its laminar counterpart. The mean angular momentum is close to constant in the bulk of the flow, except for the boundary layers, in a turbulent TC flow while it is a function of $r$ in the laminar case. Hence, we believe that using a laminar base flow to understand an instability that exists in a turbulent flow can cause an issue and give non-physical results. In order to check this, we perform the stability analysis at $\eta = 0.417$ (same as our experiments), $Re = 1000$ and $Ri_B = 6$, and using both the laminar flow profile and our empirical flow profile as the base flow. The eigenfunctions of the most unstable mode at $m = 1$ for the two cases are shown in figure 4.6. It can be clearly seen that the eigenfunctions for the laminar and the turbulent case are considerably different. The velocity perturbations in the turbulent case are restricted to each of the two layers (consistent with experiments) unlike that for the laminar case. Moreover, the calculated value of growth rate, $\sigma$ for the laminar and turbulent base flow case is $\sigma = 0.2393 - i0.2362$ and $\sigma = 0.1393 - i0.2711$ respectively. The observed growth rate and the wave period is also different in both the cases. This confirms that it is important to use the turbulent base flow for studying turbulent STC, as the laminar base flow will lead to non-physical results.

### 4.3.2 Varying boundary layer thickness

As shown in chapter 3, we performed our PIV experiments in an apparatus with $\eta = 0.417$. The mean azimuthal flow profile can be seen in figure 3.10. The scattering of light from the cylinder boundaries was too strong for us to be able to resolve velocities in the boundary layer. So we draw an arbitrary smooth boundary layer to our empirically observed profile (yellow curve in figure 4.1a) to be used as a base flow for the present stability analysis. Also, the non-dimensional boundary layer thickness would be different for apparatuses with different $\eta$. Since we do not have the exact boundary layer (BL) profiles for various $\eta$ that are used for the present analysis, we investigate the effect of varying the BL thickness.

Huisman *et al.* (2013) performed highly resolved PIV measurements for an unstratified TC flow at a $Re = 10^6$ in an apparatus with $\eta = 0.7$. The higher turbulence in their case (their $Re$ being two orders o magnitude higher) possibly makes the flow in the bulk different from that in our observations. Huisman *et al.* did resolve the boundary layers in their study. The blue curve in figure 4.1a is their observed mean azimuthal velocity profile. It was obtained by discretising figure 2 in their paper. We arbitrarily draw a narrower and a wider boundary layer to their observed profile (green and red curve respectively in figure 4.1a) and used that in our stability code to check the effect of $(a)$ varying boundary layer thickness (at different $\eta$) and $(b)$ using a non-exact boundary layer profile in the base flow. We performed the stability analysis at $Re = 1000$ and $Ri_B = 6$ using three different base flow profiles, Huisman *et al.*'s original empirical profile, a profile with narrower BL and a profile with wider BL. The analysis is performed at $\eta = 0.9$ and $0.417$ (same as our experiments). Figure 4.7 shows the absolute part of the $u$ eigenfunction of the most unstable mode for the above analysis. It can be seen that the eigenfunctions look very similar for all three base flows and at both $\eta$. The other eigenfunctions are consistent as well. Table 4.1 shows the values of the growth rate for most unstable mode for each of the above mentioned analyses. The real part is consistent up to the third significant digit while the imaginary part is consistent up to the fourth significant digit. This suggests that it is the bulk of the flow that is resulting in this unstable mode and not the boundary layers. Hence, we believe that it is appropriate to use an arbitrary drawn boundary layer for further analysis.

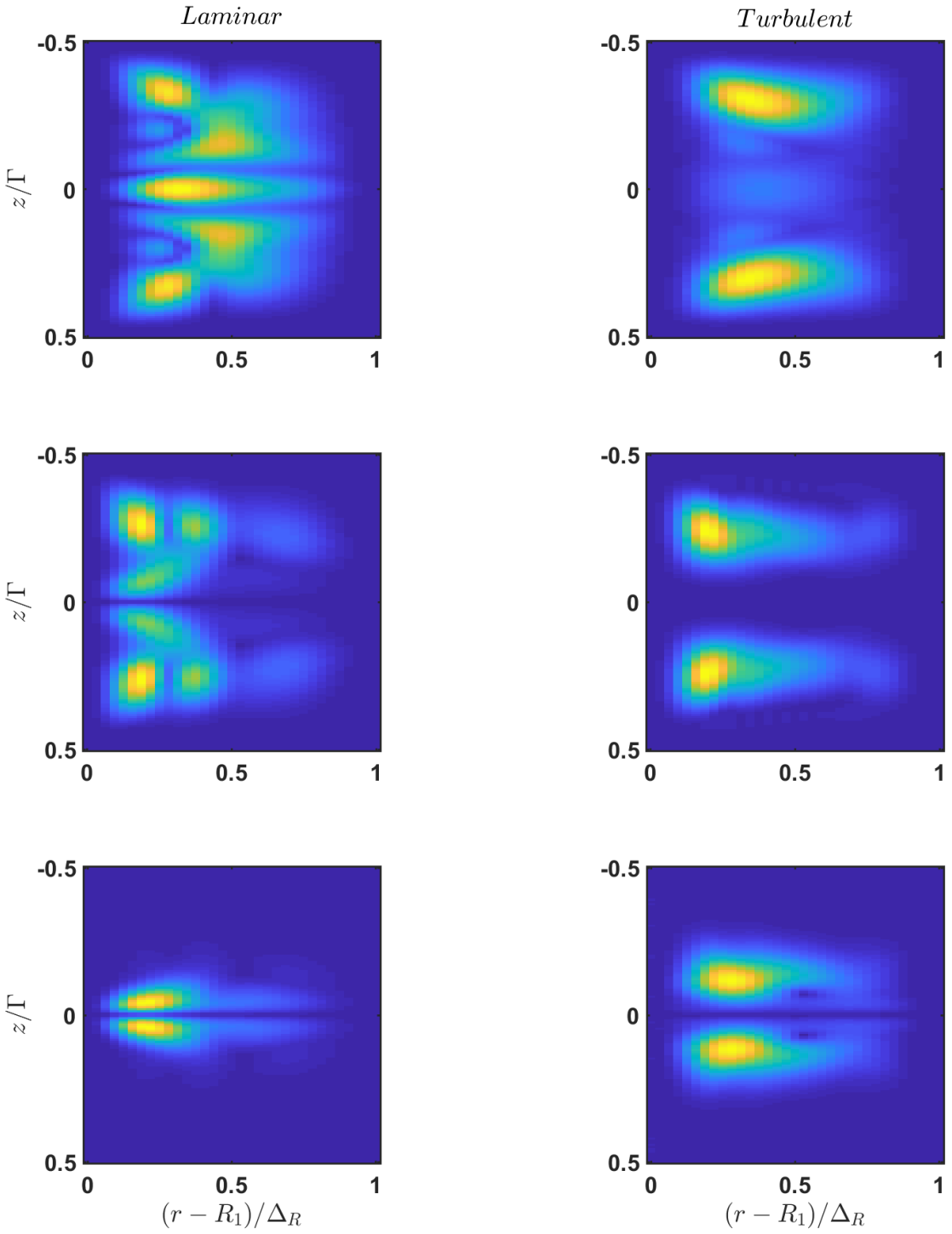


Fig. 4.6 Plot showing the absolute value of eigenfunctions for radial velocity perturbation (top row), axial velocity perturbation (middle row) and density perturbation (bottom row) for laminar base flow (left) and empirical turbulent base flow (right). Parameters: $Re = 1000$, $Ri_B = 6$ and $\eta = 0.417$.

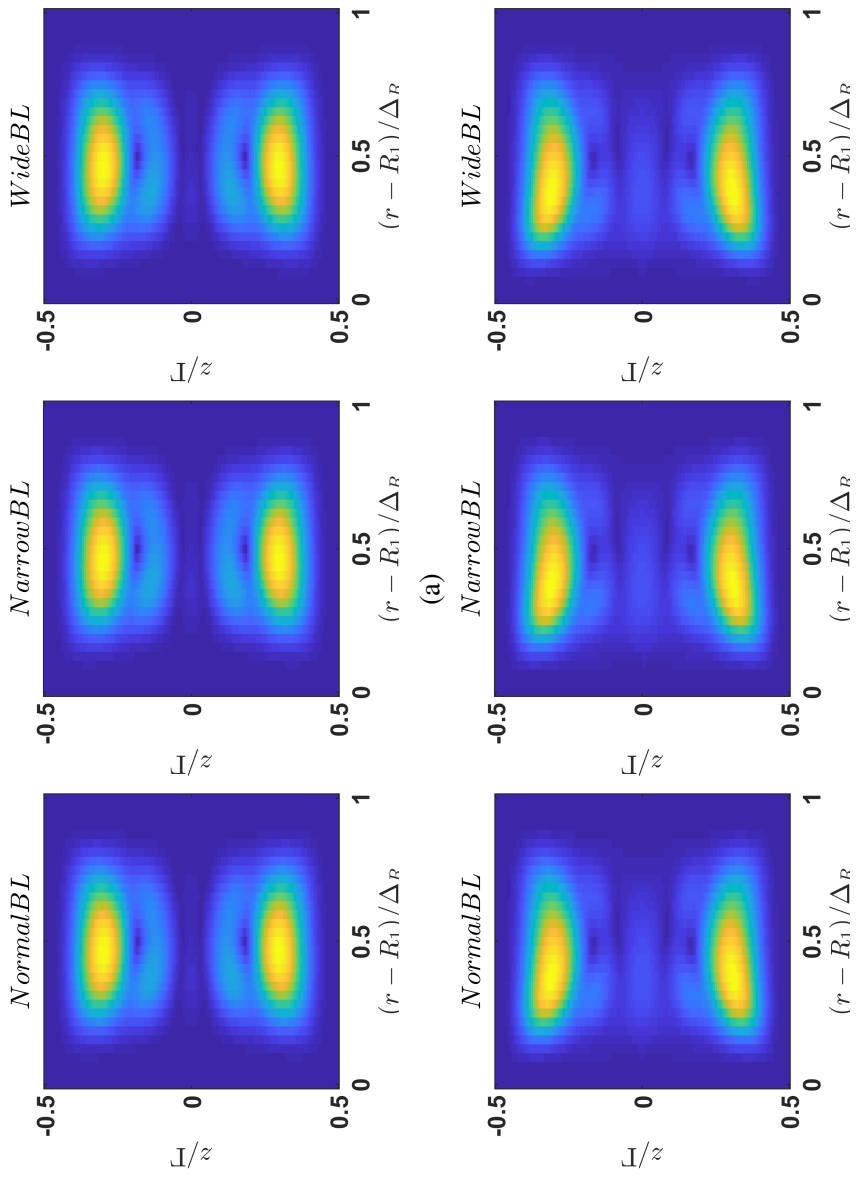


Fig. 4.7 Plot showing absolute magnitude of $u$ eigenfunction of the most unstable mode at $m = 1$ using base flow with different boundary layer (BL) thickness, as shown in figure 4.1a, at $(a)$ $\eta = 0.9$ and $(b)$ $\eta = 0.9$. Other parameters: $Re = 1000$ and $Ri_B = 6$.

| | $\eta = 0.9$ | | $\eta = 0.417$ | |
|---|---|---|---|---|
| | $\sigma_r$ | $\sigma_i$ | $\sigma_r$ | $\sigma_i$ |
| **Normal boundary layer** | 0.1337 | 0.05603 | 0.2375 | 0.39116 |
| **Narrow boundary layer** | 0.1347 | 0.05574 | 0.2389 | 0.39137 |
| **Wide boundary layer** | 0.1351 | 0.05637 | 0.2374 | 0.39366 |

Table 4.1 Table showing the calculated values of real ($\sigma_r$) and imaginary ($\sigma_i$) part of the growth rate of the most unstable mode at $m = 1$ for three different base flows at $\eta = 0.9$ and 0.417 using our stability code.

### 4.3.3 Comparing eigenfunctions to experiments

Here we make an attempt to compare the observed eigenfunctions to our observations in the experiments. In experiments, we find that the instability results in a formation of a very sharp interface near both cylinder boundaries. We perform the stability calculation at the same radius ratio as that in experiments, $\eta = 0.417$. The flow parameters are $Re = 1000$ and $Ri_B = 6$. Figure 4.8 and figure 4.9 show the real and imaginary parts of the observed complex eigenfunctions of $r$ (figure 4.8a), $v$ (figure 4.8b), $w$ (figure 4.9a) and $\rho$ (figure 4.9b), for the most unstable mode at $m = 1$. Analysing the velocity perturbation eigenfunctions, it can be seen the the most unstable mode forms a pair of three-dimensional circulation cells across the interface, near both the inner and the outer cylinder. The strength of the circulation cell is considerably higher at the inner cylinder which we believe is because of higher energy at the inner cylinder being imparted to the flow. The $\rho$ eigenfunction shows the enhanced density in the upper layer and reduced density in the lower layer. This change in density seems to be only in the middle of the annulus, away from the boundaries.

These observations seem to be consistent with our experiments. The experiments show the formation of very sharp interfaces near the boundaries which possibly are because of these circulations cells on both sides of the interface near both cylinder boundaries. This circulation could scour the interface and make it sharp. The density eigenfunction shows mixing only in the middle of the annulus, which is also consistent with our experiments as there is no observed mixing across the very sharp interface and only occurs across the mixed fluid blob in the middle. We believe that this is a very positive indication that the linear stability predictions could explain the origin of observed non-linear structures.

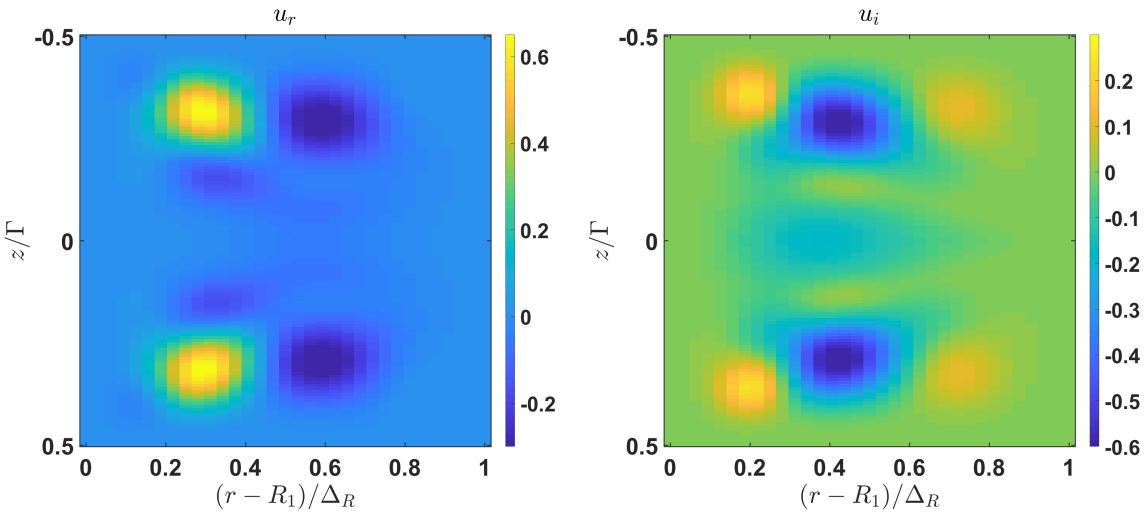


(a)

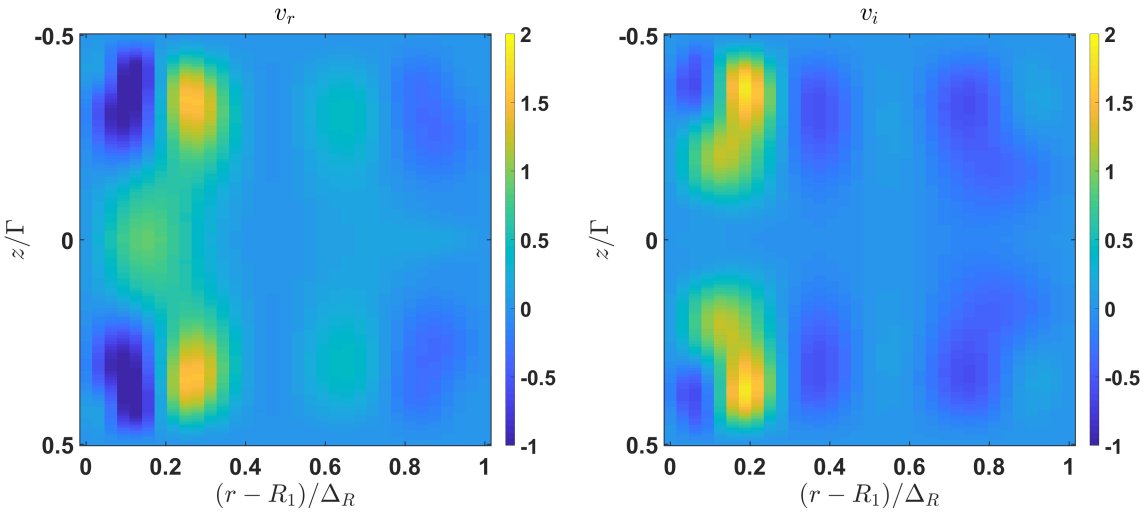


(b)

Fig. 4.8 Plot showing the real and the imaginary part of the eigenfunctions of $(a)$ radial velocity perturbations and $(b)$ azimuthal velocity perturbations, for the most unstable mode. Parameter for stability calculation: $Re = 1000$, $Ri_B = 6$, $\eta = 0.417$, $m = 1$ and using empirical base flow.

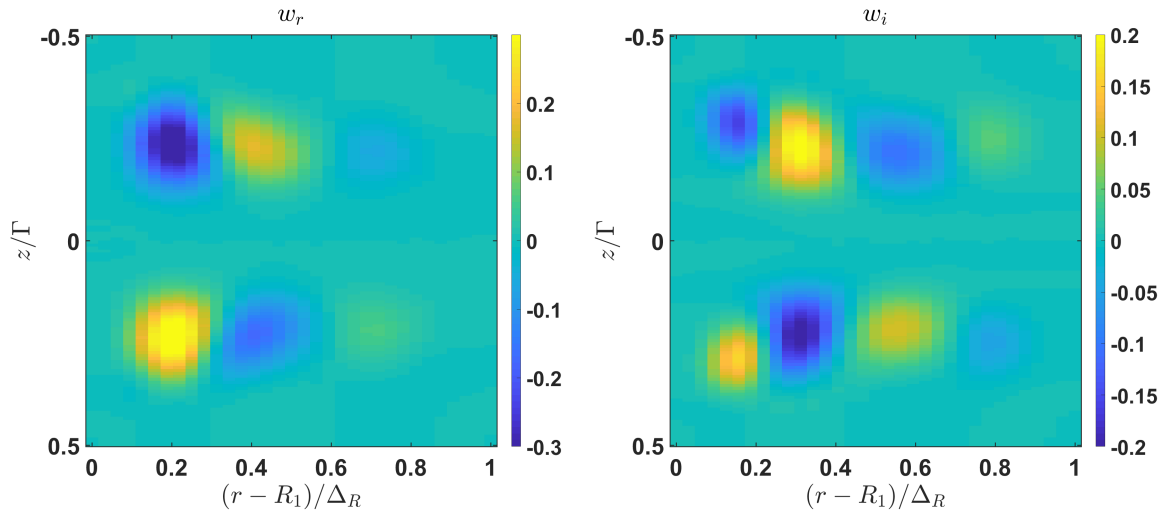


(a)

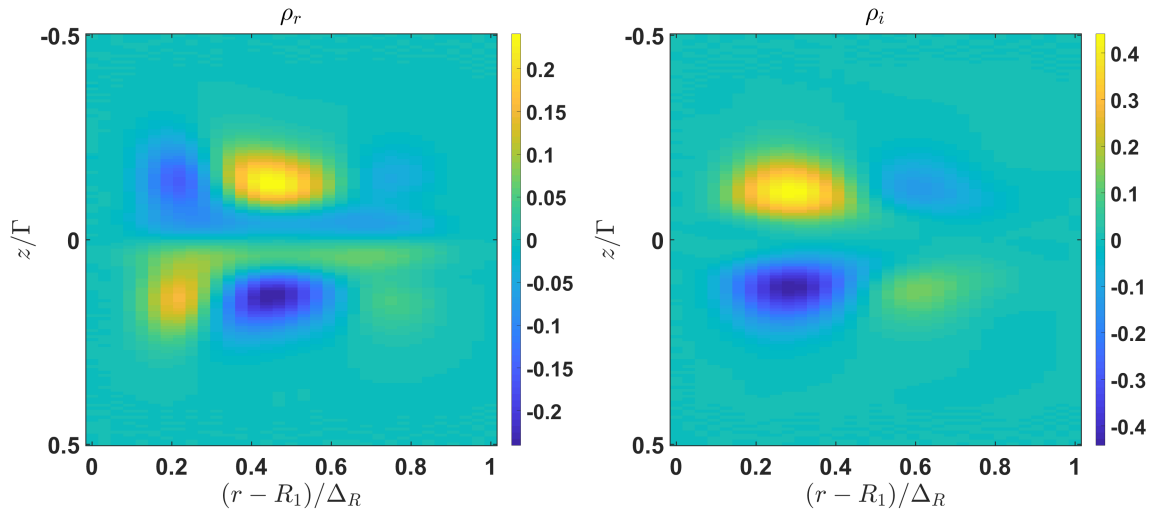


(b)

Fig. 4.9 Plot showing the real and the imaginary part of the eigenfunctions of $(a)$ axial velocity perturbations and $(b)$ density perturbations, for the most unstable mode. Parameter for stability calculation: $Re = 1000$, $Ri_B = 6$, $\eta = 0.417$, $m = 1$ and using empirical base flow.

| | $\mathbf{m=1}$ | $\mathbf{m=2}$ | $\mathbf{m=3}$ | $\mathbf{m=4}$ | $\mathbf{m=5}$ |
|---|---|---|---|---|---|
| $\mathbf{Re=1000, \eta=0.9, N_{res}=35, EBF}$ | 0.0862 | 0.0314 | 0.0015 | -0.0028 | 0.0031 |
| $\mathbf{Re=1000, \eta=0.417, N_{res}=35, EBF}$ | 0.1393 | -0.0026 | -0.0011 | - | - |
| $\mathbf{Re=3000, \eta=0.9, N_{res}=45, EBF}$ | 0.1252 | 0.0788 | 0.0558 | 0.0402 | 0.0281 |
| $\mathbf{Re=1000, \eta=0.9, N_{res}=30, HBF}$ | 0.1290 | 0.0697 | 0.0370 | 0.0151 | -0.0013 |
| $\mathbf{Re=1000, \eta=0.417, N_{res}=30, HBF}$ | 0.2334 | 0.0529 | 0.0061 | - | - |
| $\mathbf{Re=1000, \eta=0.1, N_{res}=35, HBF}$ | 0.1860 | 0.0086 | -0.0025 | -0.0024 | - |
| $\mathbf{Re=1000, \eta=0.417, N_{res}=35, HBF}$ | 0.2375 | 0.0529 | -0.0005 | 0.0010 | - |
| $\mathbf{Re=1000, \eta=0.2, N_{res}=35, HBF}$ | 0.1954 | -0.0007 | -0.0032 | 0.0144 | - |
| $\mathbf{Re=1000, \eta=0.3, N_{res}=35, HBF}$ | 0.2330 | 0.0193 | -0.0003 | -0.0003 | - |
| $\mathbf{Re=3000, \eta=0.9, N_{res}=30, HBF}$ | 0.1682 | 0.1009 | 0.0825 | - | - |
| $\mathbf{Re=3000, \eta=0.9, N_{res}=35, HBF}$ | 0.1390 | 0.1095 | 0.0844 | - | - |
| $\mathbf{Re=3000, \eta=0.417, N_{res}=35, HBF}$ | 0.2787 | 0.1103 | 0.0716 | 0.0216 | - |
| $\mathbf{Re=5000, \eta=0.417, N_{res}=35, HBF}$ | 0.3402 | 0.2188 | 0.0613 | - | - |
| $\mathbf{Re=5000, \eta=0.9, N_{res}=35, HBF}$ | 0.3419 | 0.1645 | 0.0902 | - | - |

Table 4.2 Table showing the growth rate ($\sigma_r$) of the most unstable mode at different azimuthal wavenumbers $m$, calculated using our stability code at above mentioned parameters. $Ri_B = 6$ for all calculations. $N_{res}$ is the resolution used in the radial direction. Resolution in the axial direction is $4 \times N_{res}$. EBF is the empirical turbulent base flow while HBF is the Huisman *et al.*'s base flow profile at higher $Re$. Hyphen means no stability analysis was made at that specific $m$ for the respective flow parameters.

### 4.3.4 Azimuthal mode $m = 1$?

Analysing the eigenfunctions and their comparison with the experimental observations, as discussed in the previous section, indicates that the observed non-linear structure in the experiments might be a linear instability. The most prominent feature of this empirically observed instability is that it has a wave-like structure and its azimuthal wavenumber is always $m = 1$. In this section, we look into results from stability analysis at various different parameters and find the most unstable mode for all those calculations. We perform calculations at various different parameters and vary the azimuthal wavenumber, $m$ for each set of parameters. The $Ri_B$ for all calculations is kept fixed at $Ri_B = 6$, as the instability at this $Ri_B$ is very distinctly observed. Real parts of the eigenvalues of the most unstable mode at different $m$ for all the above mentioned stability calculations are shown in table 4.2. It can be clearly seen that mode

| $Ri_B$ | EBF | HBF |
|---|---|---|
| **2** | 0.0582 - i0.0393 | 0.0915 -i0.0550 |
| **4** | 0.0752 - i0.0393 | 0.1171 - i0.0557 |
| **6** | 0.0862 - i0.0395 | 0.0134 - i0.0560 |
| **8** | 0.0945 - i0.0395 | 0.1415 - i0.0562 |
| **10** | 0.1013 - i0.0394 | 0.1568 - i0.0563 |
| **12** | 0.1070 - i0.0393 | - |

Table 4.3 Table showing eigenvalues of the most unstable mode at different $Ri_B$. The calculations were performed at $Re = 1000$ and $\eta = 0.9$ using both the empirical base flow (EBF) and Huisman *et al.*'s base flow (HBF).

$m = 1$ is always the most dominant mode for calculations using both our empirical base flow and Huisman *et al.*'s flow profile. This is in a very good agreement with our experimental observations. This strongly suggests that the observed instability in our experiments could have its origins from this $m = 1$ linear instability.

### 4.3.5 Instability period with varying $Ri_B$

In the previous section, we observed that the stability analysis of the two-layer turbulent STC flow has a preference for mode $m = 1$, which is consistent with our experimental observations. This further suggests that the instability observed in our experiments could be associated with this linear instability. But knowing that flow is fully turbulent, further validation is required to check that the $m = 1$ dominant mode in the stability analysis being consistent with $m = 1$ non-linear structure observed in experiments is not just a coincidence.

Our experimental observations suggest that the period of the instability is just a function of rotation speed for a specific $\eta$, and is independent of the flow density difference across the interface (i.e. $Ri_B$). This is consistent with observations of Oglethorpe (2014) as well. This is one of the most astonishing features of this instability. Since this instability results in vertical mixing, one would have expected this instability is affected by the density difference in the layers as stronger stratification would provide stronger resistance to vertical motion. Therefore, in order to confirm that the observed instability has its origins in the linear instability, we perform the stability analysis at different $Ri_B$, keeping all other parameters the same ($Re = 1000$ and $\eta = 0.9$) and check the calculated wave period. The imaginary part of the eigenvalue, $\sigma_i$ represents the non-dimensional frequency of the wave and we compare this

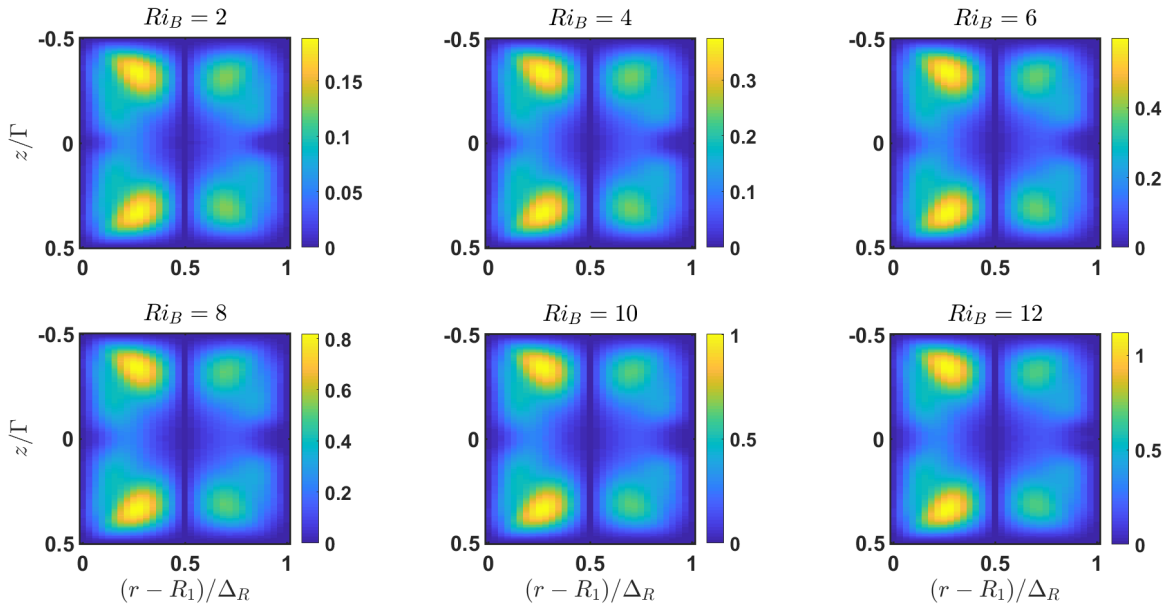


Fig. 4.10 Plot showing the absolute value of the calculated azimuthal velocity perturbation eigenfunction of the most dominant mode at different $Ri_B$, keep all other parameters the same ($Re = 1000$ and $\eta = 0.9$).

at different $Ri_B$. Figure 4.10 shows the absolute value of the calculated azimuthal velocity perturbation eigenfunction of the most unstable mode at different $Ri_B$. The eigenfunctions look consistent, indicating the dominant mode is the same at all $Ri_B$. The strength of the velocity fluctuations is seen to reduce with reducing $Ri_B$. Table 4.3 shows the eigenvalues of the growth rate, $\sigma$ of the most unstable mode at different $Ri_B$ for our empirical base flow (EBF) and Huisman *et al.*'s base flow (HBF). It can be clearly seen that instability frequency is consistent with varying $Ri_B$, which suggests the wave period is independent of $Ri_B$. The strong similarity in the behaviour of the observed experimental non-linear structure and the present linear instability suggest that the former originates as a result of this linear instability.

### 4.3.6 Instability with changing $\eta$

In the previous sections, we have found that the properties of the calculated linear instability match very well with the properties of the observed experimental instability, which strongly indicates that the latter is caused as a result of the linear instability. So far, we have not looked at the properties of this instability with varying $\eta$.

Owing to physical limitations, the experiments are performed only for $\eta = 0.21, 0.417$ and $0.625$. This range of $\eta$ was the same for Oglethorpe (2014). Oglethorpe, analysing her experiments at these three $\eta$, found a scaling for the observed instability time period, given

| $\eta$ | $\mathbf{Re = 1000, EBF}$ | | $\mathbf{Re = 1000, HBF}$ | | $\mathbf{Re = 3000, HBF}$ | | $\mathbf{Re = 5000, HBF}$ | |
|---|---|---|---|---|---|---|---|---|
| | $\sigma_\mathbf{r}$ | $\sigma_\mathbf{i}$ | $\sigma_\mathbf{r}$ | $\sigma_\mathbf{i}$ | $\sigma_\mathbf{r}$ | $\sigma_\mathbf{i}$ | $\sigma_\mathbf{r}$ | $\sigma_\mathbf{i}$ |
| **0.1** | 0.0647 | 0.3996 | 0.1860 | 0.6448 | 0.2378 | 0.6008 | 0.2371 | 0.5848 |
| **0.2** | 0.0748 | 0.4046 | 0.1953 | 0.5669 | 0.2432 | 0.5325 | 0.2432 | 0.5213 |
| **0.3** | 0.1191 | 0.3510 | 0.2330 | 0.5101 | 0.2539 | 0.5009 | 0.2509 | 0.5009 |
| **0.4** | 0.1380 | 0.2824 | 0.2385 | 0.4074 | 0.2386 | 0.4101 | 0.2897 | 0.4108 |
| **0.5** | 0.1407 | 0.2194 | 0.2284 | 0.3177 | 0.2759 | 0.3202 | 0.2825 | 0.3189 |
| **0.6** | 0.1346 | 0.1646 | 0.2117 | 0.2400 | 0.2564 | 0.2444 | 0.2612 | 0.2439 |
| **0.7** | 0.1238 | 0.1172 | 0.1915 | 0.1718 | 0.2328 | 0.1787 | 0.2361 | 0.1802 |
| **0.8** | 0.1085 | 0.0760 | 0.1673 | 0.1109 | 0.2057 | 0.1187 | 0.2086 | 0.1220 |
| **0.9** | 0.0862 | 0.0395 | 0.1348 | 0.0563 | 0.0857 | 0.0553 | 0.1720 | 0.0664 |

Table 4.4 Table showing the growth rate, $\sigma_r$ and the frequency, $\sigma_i$ of the most unstable mode from the stability analysis performed at varying $\eta$. The *Re* and the type of base flow is mentioned in the first row.

as

$$T = C\sqrt{\frac{\Delta_R}{R_1}}\frac{2\pi}{\Omega}\,, \tag{4.20}$$

where $C$ is a constant and was found to be $C \approx 4.82$ for smooth cylinders and $C \approx 3.98$ for rough cylinders. In our experiments, the observed time period matches well with this scaling.

We performed stability analysis with varying $\eta$ for different sets of parameters. Figure 4.11 shows the absolute value of $u$ and $\rho$ eigenfunctions of the most dominant mode at different $\eta$. The eigenfunctions look consistent with reducing strength as $\eta$ reduces. But at $\eta = 0.2$, there seems to be a flow transition. The observed bi-modal peak in the $\rho$ eigenfunction at higher $\eta$ seems to disappear at $\eta = 0.2$ and density fluctuations are observed on the interfaces. The same is true for the $u$ eigenfunction as well, where the flow transitions into a more complex behaviour at $\eta = 0.2$. We perform further analysis and find that this specific transition occurs specifically at $\eta = 0.2$ (i.e. a bi-modal peak is still observed at $\eta = 0.21$). Because of non-availability of apparatus with $\eta = 0.2$, we were not able to validate this behaviour experimentally.

Table 4.4 show the observed values of growth rate, $\sigma_r$ and the wave frequency, $\sigma_i$ of the most dominant mode with varying $\eta$ at specific set of mentioned parameters. The $Ri_B$ is kept to be $Ri_B = 6$ for this analysis. It can be seen the growth rate is maximum at $\eta = 0.5$ for EBF base flow, while it is maximum at $\eta = 0.4$ for HBF base flow. This is possibly the reason for us to observe a strong signal of the instability in our experiments at $\eta = 0.417$, even when the flow is highly non-linear (turbulent).

Now analysing further, we look at the instability time period at different $\eta$. The time scale in our equations is $\Delta_R/(\Omega R_1)$. We use this to calculate the time period from the non-dimensional wave frequency, $\sigma_i$ using the following equation

$$\Omega T_{ins} = 2\pi \frac{1-\eta}{\eta} \frac{1}{\sigma_i} , \tag{4.21}$$

where $T_{ins}$ is the calculated instability time period from the stability analysis. Figure 4.12 shows the variation of the calculated instability time period with $\eta$ and is compared with the time period scaling given by Oglethorpe (2014). The dashed black line represents Oglethorpe's time period scaling for a rough cylinder while the dashed grey line represents the scaling for a smooth cylinder. It can be seen that the instability time period, especially the one calculated using EBF, is in a very good agreement with Oglethorpe's scaling in the range $\eta \in (0.2, 0.65)$, which was the range of her experimental apparatus geometries using data from which she derived the scaling. There are small discrepancies in the calculated time period from the scaling which we believe are a result of the inherently highly non-linear nature of the turbulent flow. We believe that this gives the confirmation that the observed experimental instability originates as a result of a linear instability in a two-layer STC flow. For $\eta < 0.2$, the calculated time period diverges from the Oglethorpe's scaling which could be because of the change in flow behaviour as discussed above.

### 4.3.7 Stability analysis at $\Gamma = 2$

So far, all the stability calculations were performed at $\Gamma = 1$. In this section, we look into how the instability is affected as the end-walls are pushed further out, which will be more consistent representation of our two-layer experiments.

Here we perform the stability analysis at $Re = 1000$, 3000 (using EBF), $Ri_B = 6$, $\eta = 0.9$ and $\Gamma = 2$, to look how the instability compares to the previously observed instability. We perform the analysis at different azimuthal wavenumbers, $m$ and the calculated eigenvalues of the most unstable mode can be seen in table 4.5. No unstable modes are observed at $Re = 1000$ for all $m$. At $Re = 3000$, we observe the unstable modes but with a much lower growth rate in comparison to the analysis at $\Gamma = 1$. Azimuthal mode $m = 1$ is still observed

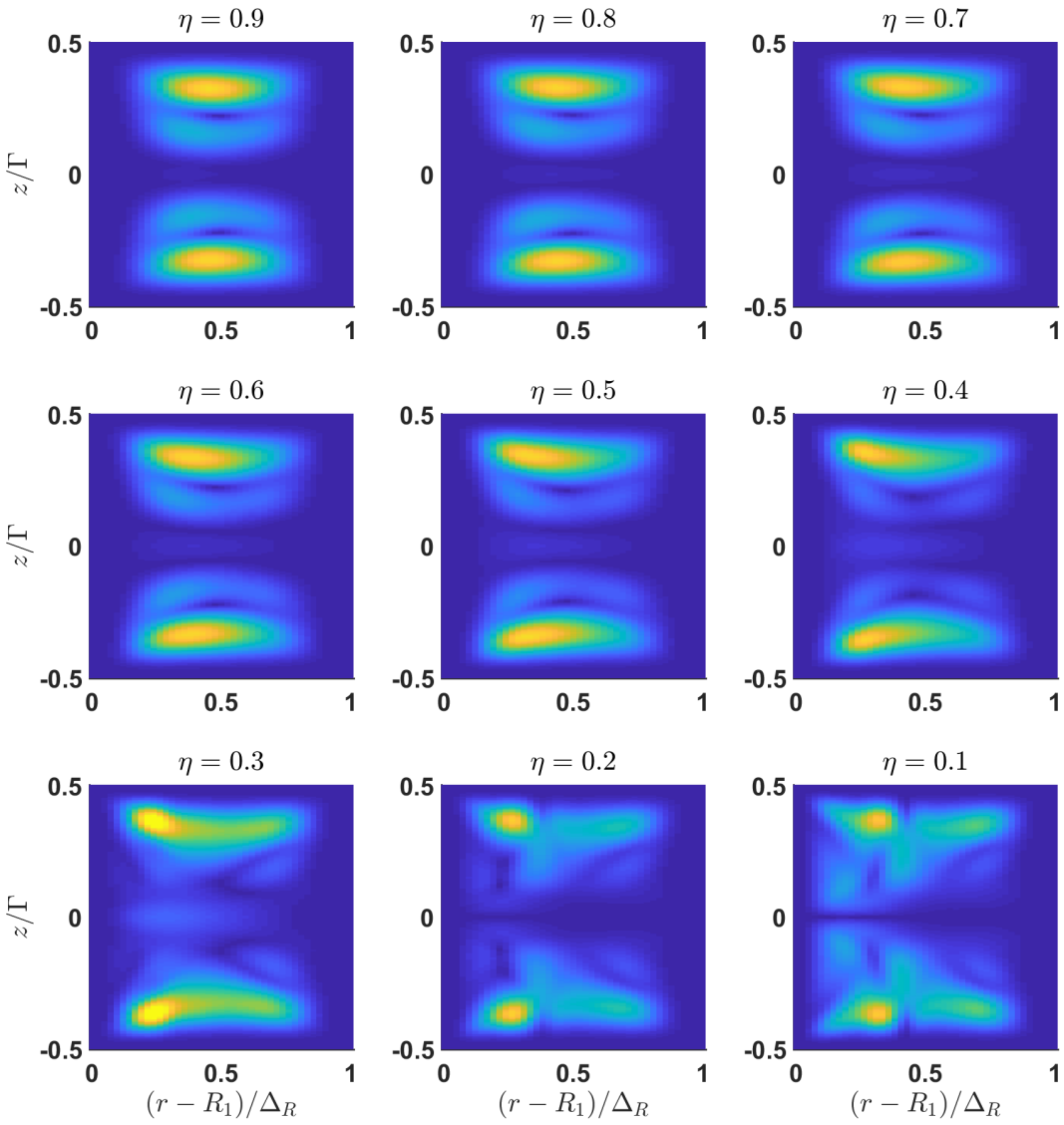


(a)

Fig. 4.11 $(a)$ Plot showing the absolute magnitude of $u$ eigenfunction of the most dominant mode at different $\eta$, keeping all other parameters the same ($Re = 3000$ and $Ri_B = 6$). Colourbar limits are the same for all plots.

to be the most dominant mode. Figure 4.13 shows the $v$ eigenfunction for the most dominant mode alongside that at $\Gamma = 1$. The dominant structure in both the eigenfunctions is the same. At the same time, the observed instability frequency of the most dominant mode is the same as that for $\Gamma = 1$ (refer to table 4.3). This confirms that the most dominant mode is the same

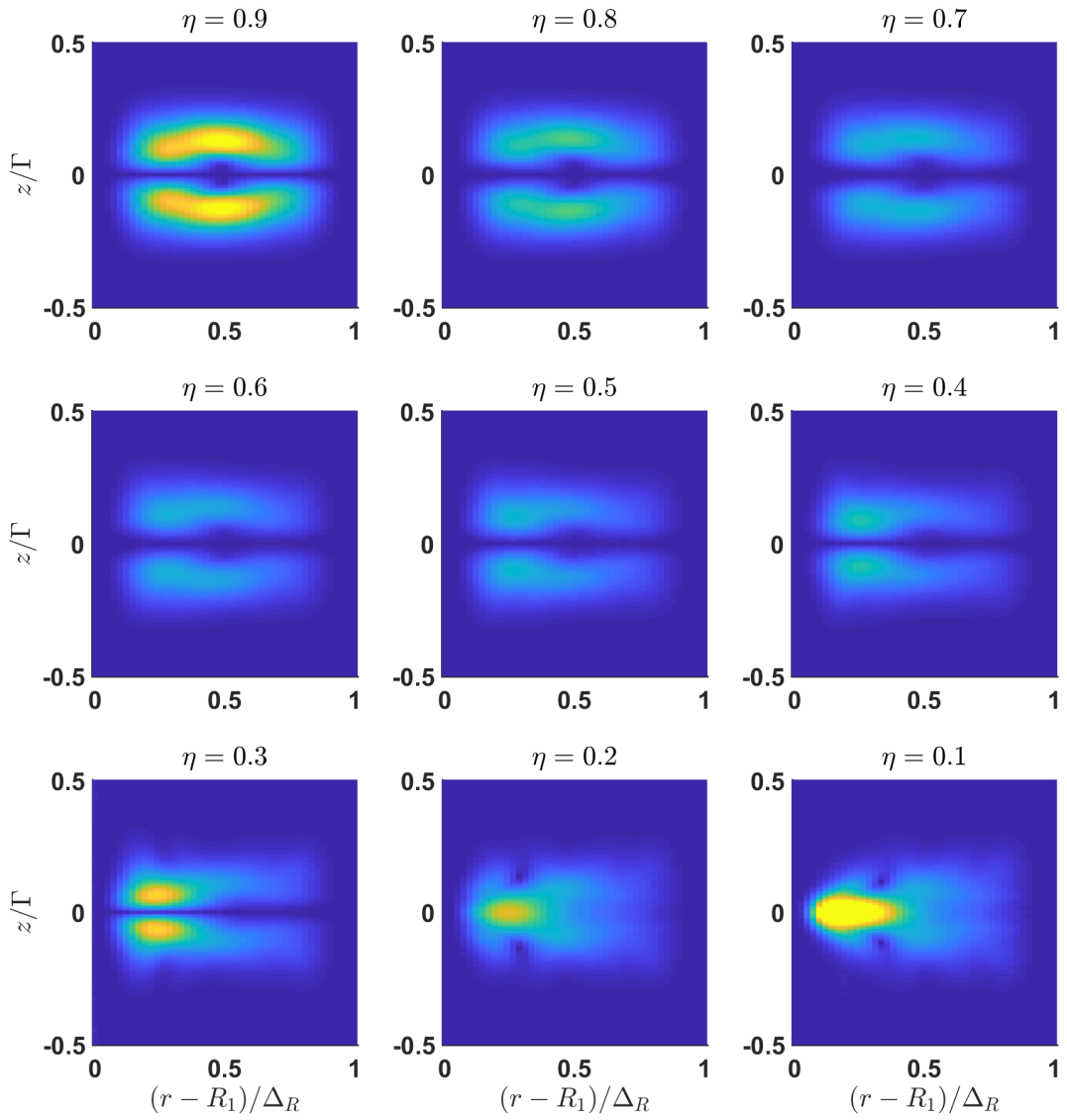


(b)

Fig. 4.11 $(b)$ Plot showing the absolute magnitude of $\rho$ eigenfunction of the most dominant mode at different $\eta$, keeping all other parameters the same ($Re = 3000$ and $Ri_B = 6$). Colourbar limits are the same for all plots.

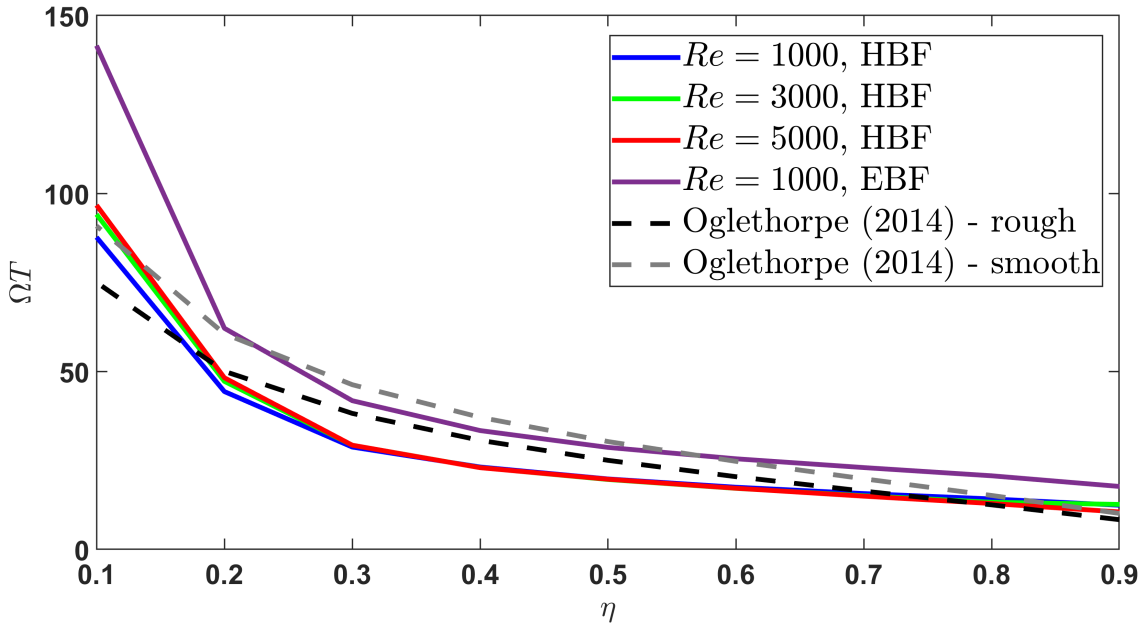


Fig. 4.12 Plot showing variation of the time period of the most dominant mode with $\eta$. Each curve represents the results from stability analysis at a specific set of parameters. The dashed black curve represents the time period scaling given by Oglethorpe (2014) for rough cylinders while the dashed grey curve represents that for smooth cylinders.

| **Parameters** | **m = 1** | | **m = 2** | | **m = 3** | |
|---|---|---|---|---|---|---|
| | $\sigma_r$ | $\sigma_i$ | $\sigma_r$ | $\sigma_i$ | $\sigma_r$ | $\sigma_i$ |
| $\mathbf{Re = 1000, \eta = 0.9, N_{res} = 35}$ | -0.0006 | 0.0094 | -0.0012 | 0.0183 | -0.0019 | 0.0271 |
| $\mathbf{Re = 3000, \eta = 0.9, N_{res} = 47}$ | 0.0359 | 0.0394 | 0.0340 | 0.0676 | 0.0114 | 0.0907 |

Table 4.5 Table showing the complex growth rate values, $\sigma$ of the mode with highest growth rate at different azimuthal wavenumbers $m$, calculated using the stability code at above mentioned parameters and $\Gamma = 2$. $Ri_B = 6$ for all calculations. $N_{res}$ is the resolution used in the radial direction. Resolution in the axial direction is $4 \times N_{res}$. EBF is used for this analysis.

in both cases. But the fact that the growth rate is decreasing with pushing the end-walls away (increasing $\Gamma$) indicates that the presence of these walls is important for this instability to exist. For an initially linearly stratified STC flow, the adjacent interfaces act as a wall for

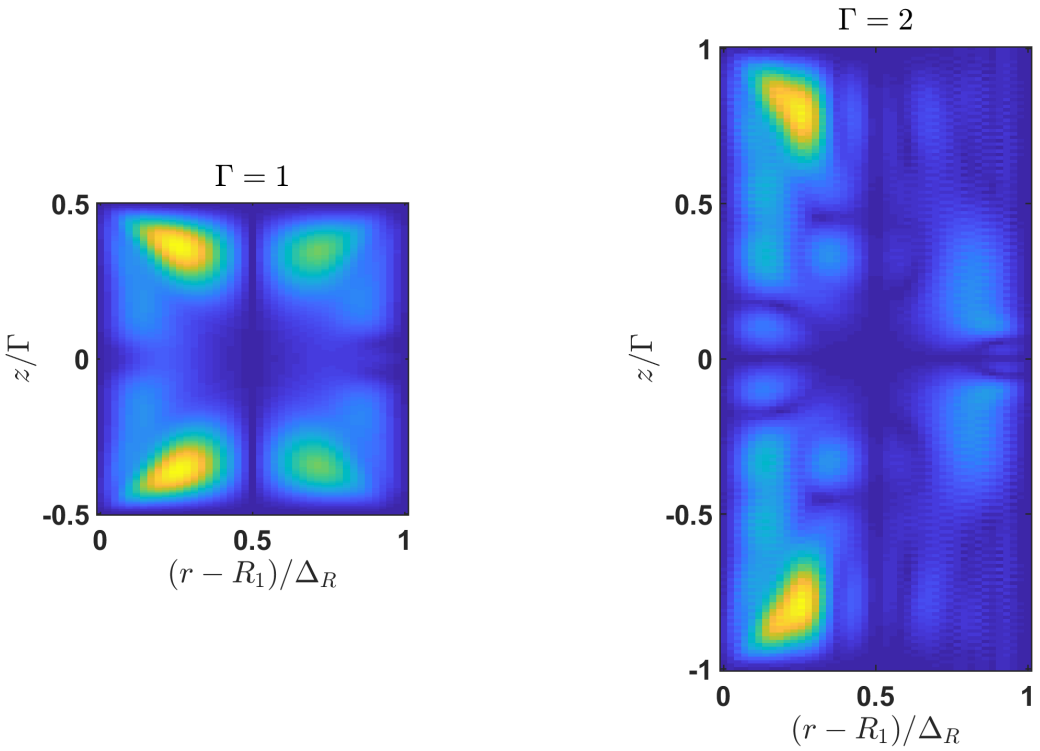


Fig. 4.13 Plot showing the calculated azimuthal velocity perturbation eigenfunction of the most dominant mode at $\Gamma = 1$ (left) and at $\Gamma = 2$ (right) where keeping all other parameters the same. Parameters: $Re = 3000$, $Ri_B = 6$ and $\eta = 0.9$.

the velocity and density perturbations, which would mean one would always observe this instability on each of the formed interfaces in a linear STC.

It is interesting to note here that although $m = 1$ is the dominant mode, the value of growth rate, $\sigma_r$ for mode $m = 2$ is only marginally smaller than that at $m = 1$ (refer to table 4.5). This reminded the author of one of the previous simultaneous PIV and LIF experiments where azimuthal mode $m = 2$ was observed. Figure 4.14 shows the time-series of the azimuthal velocity perturbations and LIF recordings along one radial line for the above mentioned experiment (at $Ri_B = 6.3$). The nature of the flow looks consistent with other experimental observations, but the observed period is $\approx 17$ s which is almost half of the observed period in other experiments with same parameters. There was one more experiment where similar $m = 2$ behaviour was observed. It was one of the preliminary experiments where the line laser was hand-held to visualise the instability and recorded with a mobile camera, and hence, the recording is not good enough to be presented here. We now believe that since our experimental conditions for two-layer STC was $\Gamma = 3$, $m = 2$ was marginally less unstable

than $m = 1$ mode, the flow chooses the dominant mode most of the time, but at times, the non-linear nature of the flow chooses the $m = 2$ mode.

## 4.4 Discussion

In this chapter, we have looked into the linear stability analysis of a two-layer STC flow using the empirically observed mean turbulent flow as the base flow. The base velocity flow profile is purely azimuthal velocity varying in $r$ and the base density profile mimics the empirically observed density profile varying in $z$. The profiles can be seen in figure 4.1. Having a base flow with a dependence in both $r$ and $z$ (refer to figure 4.2), made these stability calculations extremely challenging and computationally very expensive. We were able to successfully make it work with all boundary conditions being satisfied. However, because of the high computational costs involved, we were not able to go to high enough resolution to have no spurious modes. Nonetheless, those spurious modes were easily identifiable and were ignored.

Although we performed our analysis using the base turbulent velocity profile, we did look at the effect of using a laminar TC velocity profile as the base flow since most of the previous studies, to the best of our knowledge, used the laminar TC profile in their numerical simulations and stability studies. We find that the eigenfunctions look considerably different for the two cases, which suggests that it is not appropriate to use the laminar profile for studying turbulent flows.

The first interesting result was that we find the most unstable mode in our calculations to be always azimuthal mode $m = 1$, which was consistent with our experimental observations. Analysing the eigenfunctions of the most dominant mode, suggested the formation of three dimensional circulation cell on both sides on the interface and around both cylinders. It is plausible that these circulation cells lead to the formation of the extremely sharp interfaces at both cylinder boundaries. To confirm that the calculated mode resembles the observed empirical instability, we perform the stability analysis at different $Ri_B$, and found that the instability period is independent of the $Ri_B$, consistent with empirical observations. Most importantly, we were able to predict the instability period consistent with the scaling provided by Oglethorpe (2014) at different radius ratios $\eta$, especially for the range of $\eta$ that was used in the experiments of Oglethorpe (2014) to derive the scale. This strongly suggests that the observed empirical instability has its origins in this linear instability.

However, an open question still exists as to what sets the layer height in an initially linearly stratified STC flow. Leclercq *et al.* (2016*b*) performed a DNS and stability analysis of the STC flow and observed the same layer height as empirically observed by Oglethorpe (2014).

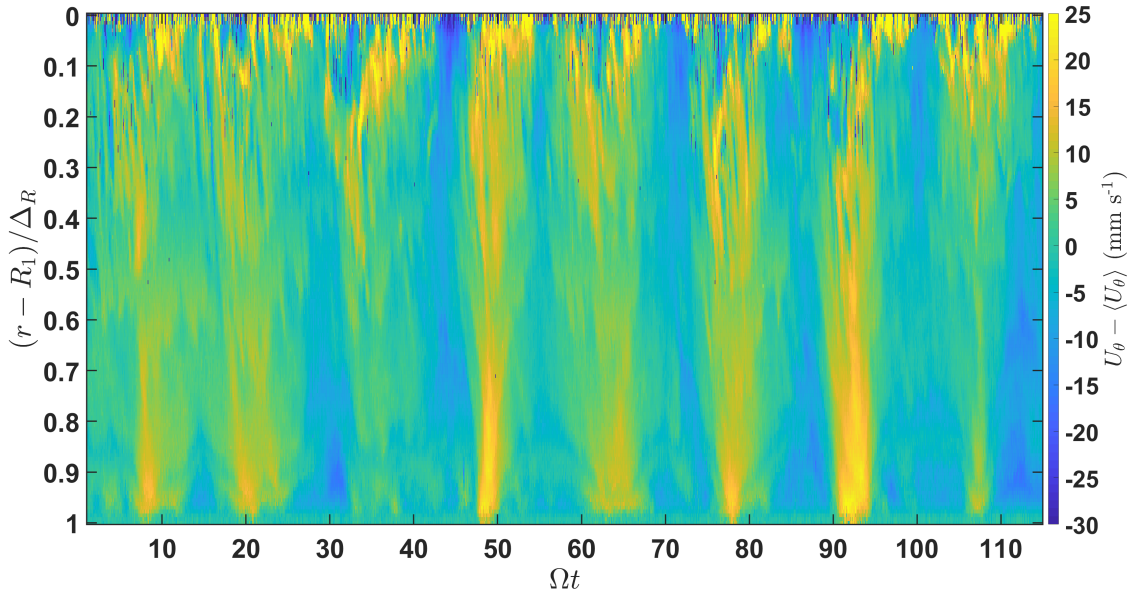


(a)

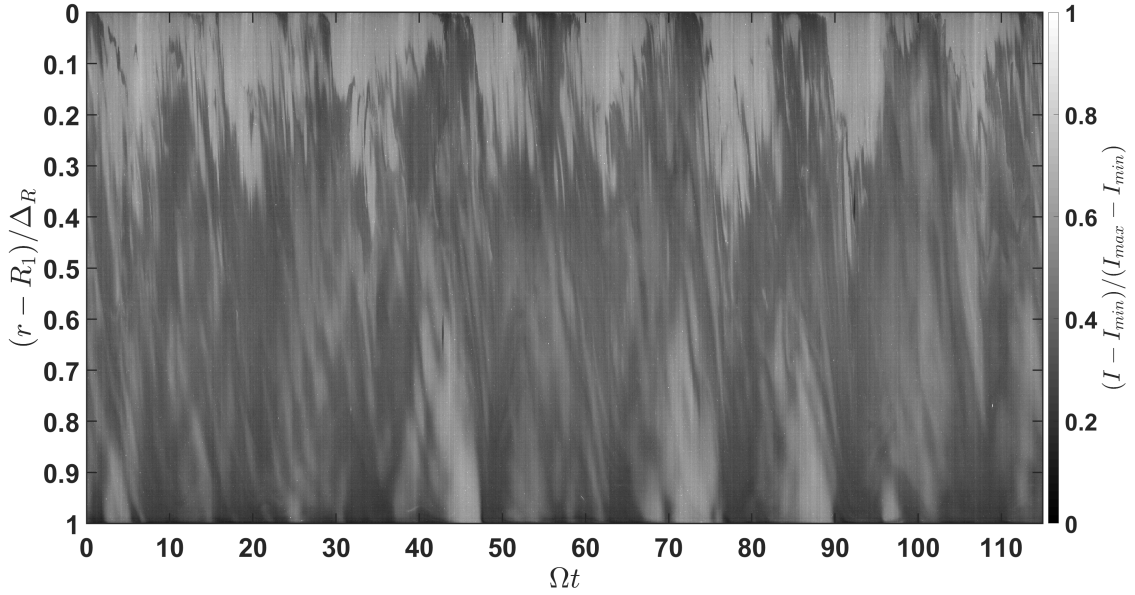


(b)

Fig. 4.14 Plot showing the time-series of (*a*) azimuthal velocity perturbations and (*b*) scalar field, along one radial line for the experiment with $m = 2$ instability. The observed time period is $\sim 17$ s. Parameters: $Re = 14000$ and $Ri_B = 6.3$.

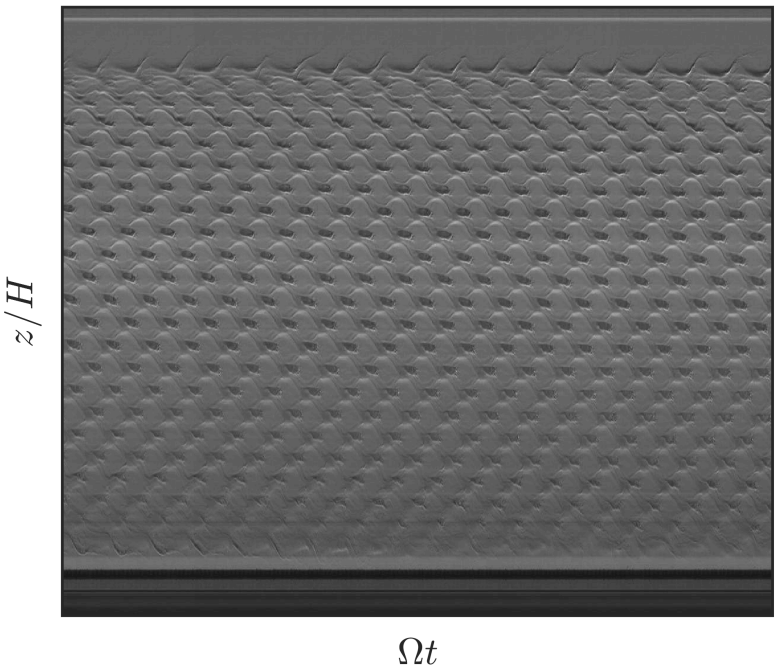


Fig. 4.15 Plot showing a vertical slice from the shadowgraph recordings of an initially linearly stratified STC flow.

They suggested the presence of SRI-like inertia-gravity helical modes causes formation of the layers. Park *et al.* (2017) performed stability analysis and found that SRI (refer to section 1.4) and centrifugal instability (the instability that results in formation of Taylor rolls, etc. in unstratified Taylor-Couette flow) both co-exist and are in competition in centrifugally unstable flows. This was also experimentally confirmed by Park *et al.* (2018). An SRI-like structure has also been observed in an initially linearly stratified and centrifugally unstable experiment performed in our laboratory[1]. Figure 4.15 shows the time-series of a vertical slice from the shadowgraph recordings for that experiment. Under specific lighting conditions, the SRI-line instability is observed. There seem to be two-helical modes, and their interactions form a sharp interface. This also explains the coupling observed for the adjacent layers. Owing to the above discussion, we here hypothesise that during the start of experiment when the flow has not achieved a fully turbulent state, SRI-like helical mode sets in the perturbations, which are then amplified by the 'Phillips mechanism' and forms the layers at a specific characteristic height. Now, on each of the interfaces, there exists the azimuthal mode $m = 1$ instability which is the same as in the two-layer STC flow.

[1]This experiment was performed by Dr. Jamie Partridge before the author joined the laboratory.

# Chapter 5

# Mixing instability in STC at $\mu > 0$

## 5.1 Introduction

In this chapter, we look into the effect of the observed non-linear structure on the interface in a STC flow, with a rotating outer cylinder, alongside the inner cylinder rotation.

Taylor-Couette flow is a popular flow to be studied in a laboratory, which has led to an abundant scientific literature. This is for two major reasons. Firstly, it is easier to achieve high *Re* in a laboratory conditions with a TC apparatus. Secondly, and more importantly, because of the richness of different regimes and flow patterns (Andereck *et al.*, 1986), understanding which has led to significant breakthroughs in explaining various physical flow phenomena. Rayleigh's criterion (Rayleigh, 1917) states that this unstable flow results from the centrifugal instabilities and the domain of these instabilities is set by $\mu < \eta^2$, where $\mu = \Omega_2/\Omega_1$. $\Omega_2$ and $\Omega_1$ are the angular velocities of the outer and the inner cylinder respectively.

The instabilities exist in stratified Taylor-Couette flow as well, so much so that the instabilities have been observed to exist even outside the domain of centrifugal instabilities i.e. for $\mu > \eta^2$, except for the case of solid body rotation i.e. for $\mu = \eta$ (Park & Billant, 2013). In the previous chapters, we discovered and analysed the instability that exists on the interface in purely centrifugally unstable turbulent STC flow ($\mu = 0$). We find that the instability exists in the form of two boundary trapped waves on the interface and their interaction results in mixing.

Rotating the outer cylinder has a stabilising effect on the flow (rotation in the same direction as that of the outer cylinder). However, if the flow is linearly stratified, inertia-gravity waves can exist in the flow and their resonance can have a destabilising effect. Yavneh *et al.* (2001) and Molemaker *et al.* (2001) were the first to reveal the flow to be unstable outside the domain of centrifugal instability. The instability formed here is non-axisymmetric and was given the name 'strato-rotational instability' (SRI) by Dubrulle *et al.*

(2005). Shalybkov & Rüdiger (2005) demonstrated the instability condition for SRI is $\mu < \eta$ which was confirmed by the experiments of Le Bars & Le Gal (2007). However, recent experiments by Ibanez *et al.* (2016) for a stronger stratification shows that the SRI exists for $\mu > \eta$ as well. More recently, through linear stability analysis, Leclercq *et al.* (2016*a*) and Park *et al.* (2017) have shown that the SRI exists even in the centrifugal unstable range and is in competition with the centrifugal instabilities, which was confirmed experimentally by Park *et al.* (2018).

However, although changing $\mu$ can lead to a different instability, for it to exist it requires the presence of a linear stratification. The authors were not able to find any previous study investigating instabilities in a two-layer STC flow with $\mu \neq 0$. In this chapter, we perform experiments with progressively increasing the outer cylinder rotation (i.e. increasing $\mu$) to study the effects on the observed instability at $\mu = 0$, and check if it compares to the SRI.

## 5.2 Experiment

The experiments shown in this chapter use the same Taylor-Couette apparatus as discussed in section 2.2. The inner cylinder of radius, $R_1$ =10 cm is used, which means $\eta = 0.417$. The tank is filled as discussed in section 2.2.1, to produce a two-layer stratification with fresh water and salt water. It is filled to a height of 14 cm i.e. $\Gamma = 1$. A polystyrene lid is used on the free surface to ensure symmetry in the boundary conditions.

### 5.2.1 Shadowgraph

The shadowgraph technique is used in our experiments to get a qualitative idea of the density interfaces. Shadowgraph is the fluid visualization technique used to detect the second derivative of the refractive index in the flow field. The refractive index of the salt solution is proportional to its density. The flow is illuminated by a light source, which is a slide projector for our experiments, kept at some distance ($\sim 2-3$ m) from the screen, for the light rays hitting the screen to be closely parallel. The screen is placed on the other side of the test fluid as the light source. A white film is pasted on the inner cylinder, which acts as a screen in our experiments. The light rays passing through the flow fluid bend due to the refractive index variation of the fluid in that region before hitting the screen. As a result, dark and bright bands are observed on the screen, which are then recorded by the camera. It is worth noting here that, since the light passes through complete flow field before reaching the screen, the observation on the screen is the representation of integration of the second derivative of

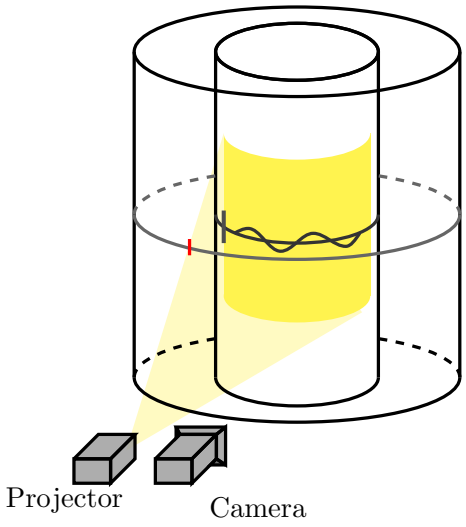


Fig. 5.1 Schematic of the setup used for shadowgraph experiments. The red line is the marker on the outer cylinder to find the region of outer cylinder being projected on the screen.

density along the path of the light. The schematic of the setup used for our experiments is shown in figure 5.1.

## 5.3 Observations and Analysis

### 5.3.1 Experiments

In this section, we look into how the previously observed instability on the interface with fixed outer cylinder is affected by outer cylinder rotation.

We perform experiments using the shadowgraph technique to visualise the interface. The inner cylinder is always made to rotate at $\Omega_1 = 1\,\mathrm{rad\,s^{-1}}$ which gives the Reynolds number for inner cylinder to be $Re_1 = 14000$, which is consistent with the experiments shown in chapter 3. We vary the angular velocity of the outer cylinder progressively, starting from $\Omega_2 = 0\,\mathrm{rad\,s^{-1}}$, in steps of $= 0.1\,\mathrm{rad\,s^{-1}}$ i.e. starting with $\mu = 0$ and increasing $\mu$ progressively in steps of 0.1. The experiment is started at $Ri_B \approx 4$ which is chosen as we previously observed a clear indication of the mixing phenomenon at this $Ri_B$ in a shadowgraph experiment at $\mu = 0$. As expected, we observed a periodic mixing phenomenon occurring at $\mu = 0$ as can be seen in figure 5.2a. The observed period is consistent with the scaling provided by Oglethorpe (2014).It is useful to note that we observe the same instability period in the present experiment at $\Gamma = 1$ as previous experiments at $\Gamma = 3$. This further justifies the use of $\Gamma = 1$ for our linear stability analysis as discussed in chapter 4.

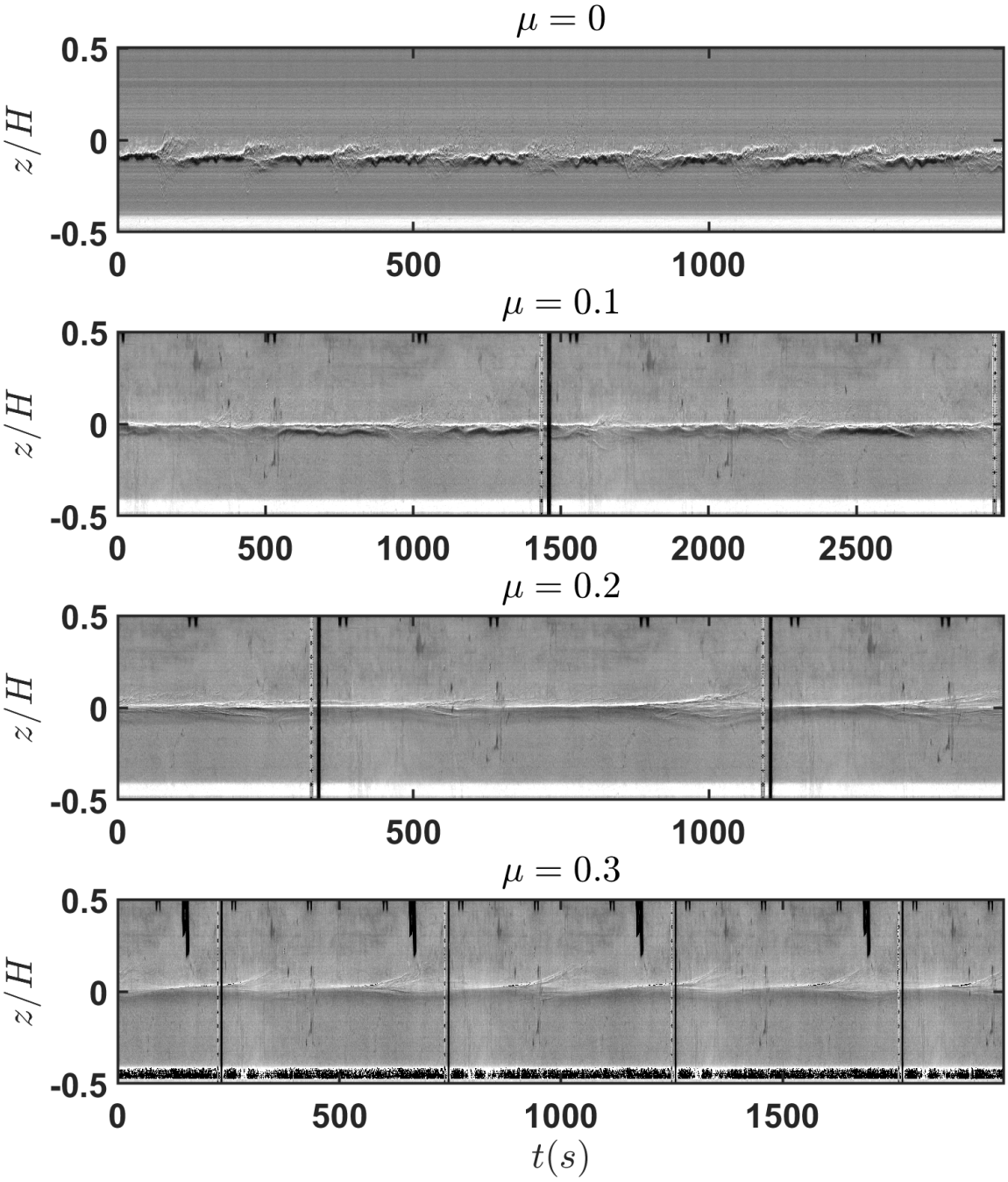


(a)

Fig. 5.2 Time-series of a vertical line from shadowgraph recordings of the two-layer STC flow at different $\mu$. The vertical white line in the time-series is from the ruler that was attached to the outer cylinder and the black line represents its shadow on the inner cylinder.

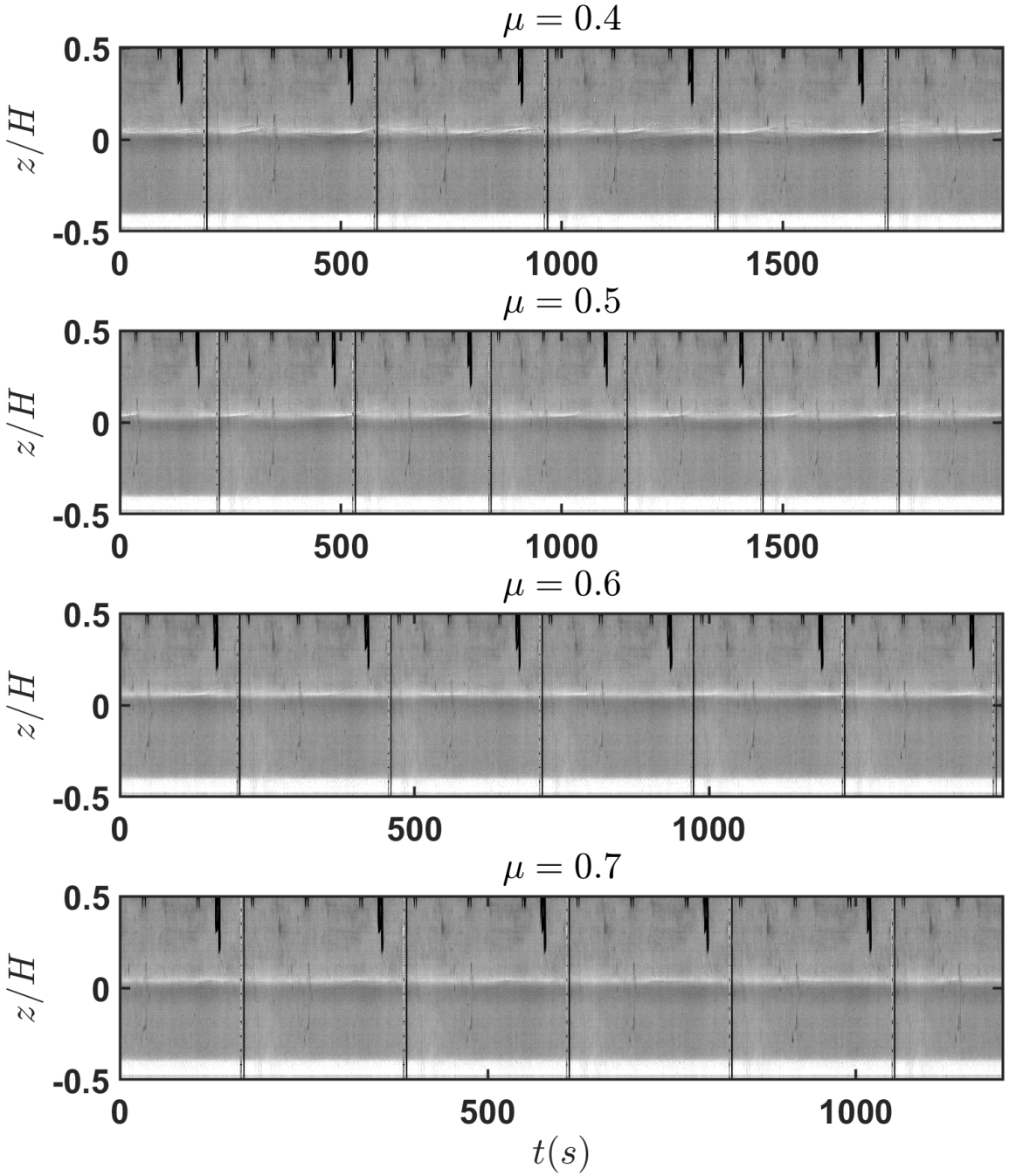


(b)

Fig. 5.2 Time-series of a vertical line from shadowgraph recordings of the two-layer STC flow at different $\mu$. The vertical white line in the time-series is from the ruler that was attached to the outer cylinder and the black line represents its shadow on the inner cylinder.

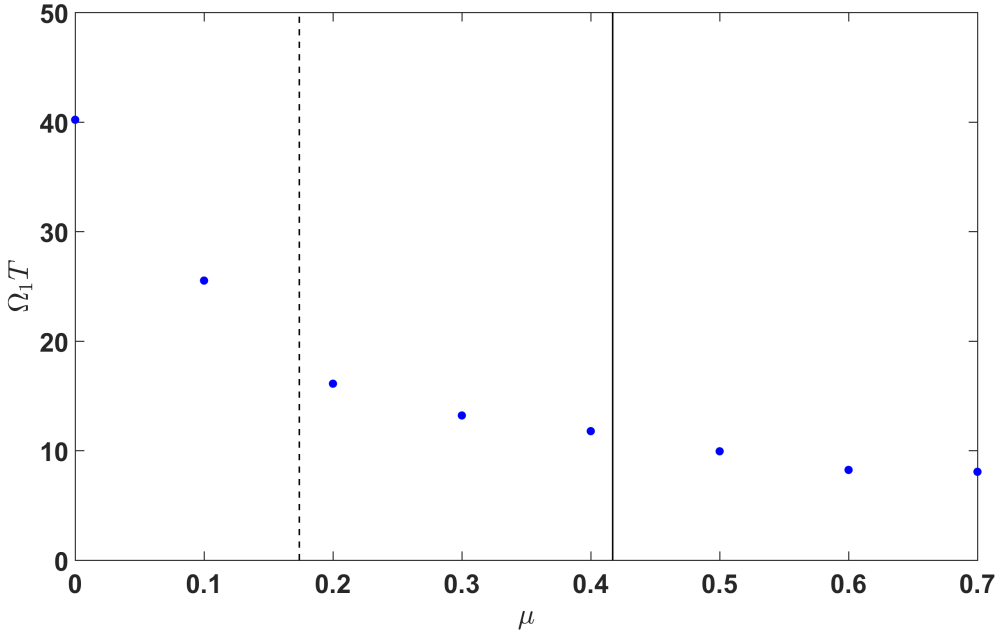


Fig. 5.3 Variation of observed instability period with $\mu$. The solid line the SRI instability condition line $\mu = \eta$ given by Shalybkov & Rüdiger (2005). The dashed line is the Rayleigh's criterion line (Rayleigh, 1917).

Figure 5.2 shows the time-series of a vertical line from the shadowgraph recordings at different $0 \leq \mu \leq 0.7$). A clear periodic event is observed at the interface in all the time-series. In order to find the period, we used a Fast Fourier transform on the observed intensity at the interface over time (a horizontal line on the interface in the time-series). Figure 5.3 shows the observed time period in the above experiments at different $\mu$. We observe that the period non-linearly decreases with increasing $\mu$. An attempt was made to observe the period for both $\mu < 0$ and $\mu > 0.7$ as well. For $\mu < 0$, although a hint of periodicity is observed to the naked eye, interface itself is extremely turbulent to confirm periodicity through shadowgraph images. At $\mu > 0.7$, the interface seems to be completely stable and the instability, if any, can not be visualised using a shadowgraph.

It is seen in figure 5.2 that, although a periodic event exists at all $\mu$ in the range covered, the periodic structure is more turbulent at lower $\mu$, and almost no turbulence is visibly observed at $\mu > 0.4$. This is consistent with the fact that the outer cylinder rotation stabilises the centrifugal flow. As discussed in chapter 3, the observed periodic structure in the shadowgraph recordings is due to periodic splashing at the outer cylinder. We believe that the reduction of observed turbulence means that there is reduced splashing on the outer cylinder as the angular momentum at the outer cylinder increases (i.e. with increasing $\mu$). For the apparatus, the angular momentum at the inner and the outer cylinder boundaries is the same

at $\mu = \eta^2 = 0.174$. We do observe a periodic instability even beyond $\mu = \eta^2$, which, to the best of our knowledge, makes this study the first one to discover an instability in a two-layer STC flow in the centrifugally stable domain of Rayleigh's criterion.

With the angular momentum being balanced, one would expect no further splashing from for $\mu > \eta^2$. We, however, do observe a periodic turbulent structure on the interface in our shadowgraph time-series at $\mu = 0.3$, which represents the presence of splashing. We also observe that the change of behaviour in the flow from splashing to non-splashing occurs around $\mu = 0.4 \approx \eta$. Further insights on this will be given in the next section. It is plausible that this change in behaviour would also result in decreased flux at higher $\mu$ since it was the splashing that resulted in the dominant mixing.

**Comparison with instability at $\mu = 0$**

In the section above, we find that the instability does exist on the interface in a STC flow even in the Rayleigh stable regime. Also, there is a change in flow behaviour from splashing to non-splashing at around $\mu = \eta$. In this section, we make an attempt to compare the observed periodic instability at different $\mu$.

In a turbulent two-layer STC flow with $\mu = 0$, we have previously observed an instability on the interface in the form of two boundary trapped waves, one at each cylinder boundary, and the continuous ejections from the inner boundary layer pushes the mixed fluid blob towards the outer cylinder, suppressing the wave at the outer boundary and resulting in a splash and in turn, causes mixing, as discussed in chapter 3. As the outer cylinder is rotated, it would increase the momentum at the outer boundary and consequently, avoid the splashing by resisting the higher momentum from the inner boundary. This is consistent with our observations as there is reduced turbulence in the periodic structure with increasing $\mu$.

As also discussed in chapter 3, the observed instability at $\mu = 0$ is that the two boundary trapped waves are always in-phase and cause the formation of an extremely sharp interface around both cylinder boundaries. When the extremely sharp interfaces are going around, the average thickness of the interface along the radial line would be reduced. This is consistent with our shadowgraph observations at higher $\mu$ (especially at $\mu > 0.4$). The periodic event for $\mu > 0.4$ exists in the form of periodic sharpening of interface. The temporal extent of this periodic sharpening is less than the observed extent of the extremely sharp interface because the light rays in the present shadowgraph setup are not completely parallel and hence, these shadowgraph recordings do not represent an exact radial line.

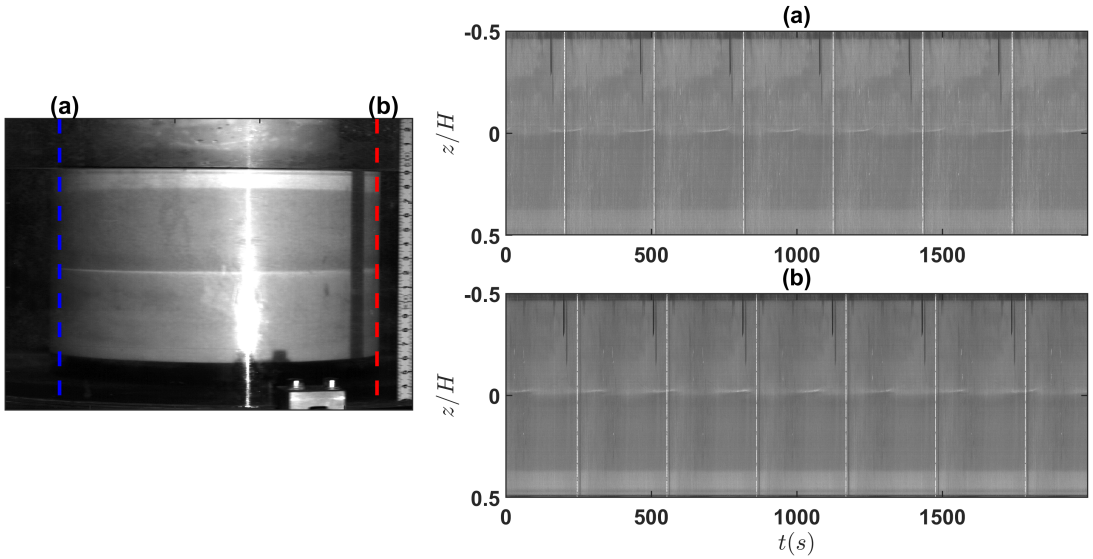


Fig. 5.4 (Left) Figure showing the actual recorded shadowgraph image. (Right) Figure showing time-series of two different vertical lines (dashed lines in left picture) at two ends of the screen. This is done for the experiment with $\mu = 0.5$.

### Azimuthal wavenumber at high $\mu$

The analysis in the previous section gave a qualitative idea that the structure of the instability in the Rayleigh stable regime might be same as that observed at $\mu = 0$. In this section, we look into validating this further.

Another prominent feature of the experimentally observed instability at $\mu = 0$ is that the boundary trapped waves typically exhibit the azimuthal mode $m = 1$. Here we will use our shadowgraph recordings to find out the azimuthal wavenumber for the instability at $\mu > 0$. We plot the time series of two vertical lines from the shadowgraph images, lines being at two ends of the screen as shown in figure 5.4. The top time-series is the time evolution of intensity in the recorded images at the location of blue dashed line, while the bottom time-series is for the red dashed line. Next we plot the intensities at the interface for the two time-series, as seen in figure 5.5. The intensity peaks from the white ruler and its shadow are removed. Clear periodic intensity peaks are observed, representing the presence of this periodic instability. Now, cross-correlating these two intensity curves gives us the time it takes for the instability to move from one end of the screen to the other.

Now, we calculate the region of the circumference for the outer cylinder that is projected on to the screen. We use the ruler which is fixed to the outer cylinder for this purpose. When the ruler comes into the path of the light that is being projected on the screen, a shadow is created. The circumferential distance that the ruler moves for the shadow to cover the

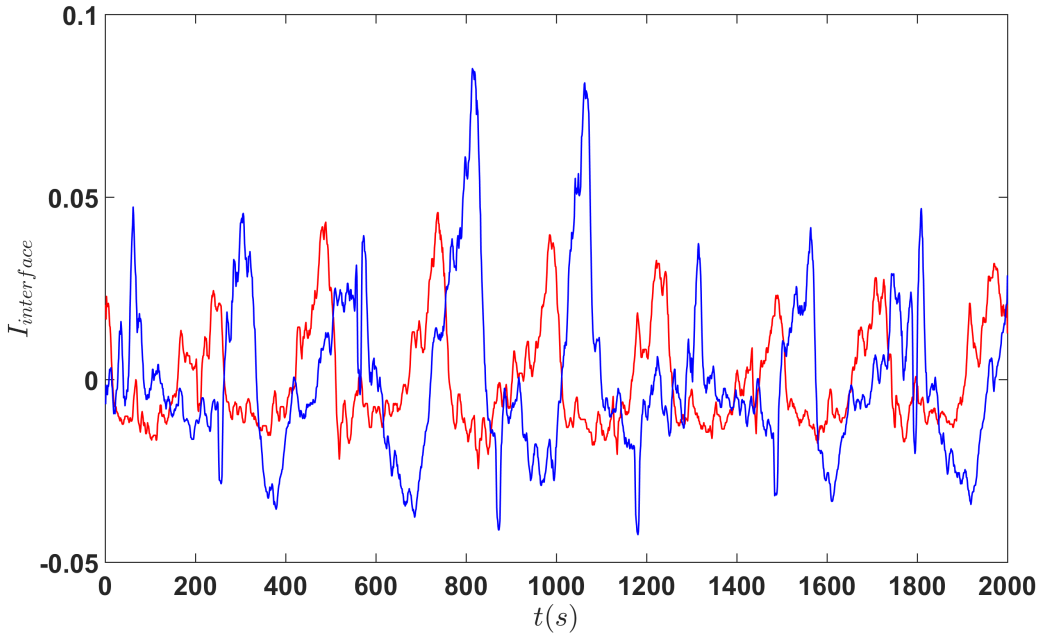


Fig. 5.5 Plot showing the intensity at the interface from two time series in figure 5.4.

complete screen gives us the region of the outer cylinder that is represented by the screen. This idea is also shown in the schematic in figure 5.1 where a red marker represents the ruler. Assuming that the instability exists near the outer cylinder and using the previously calculated period for the instability to cover the region on the screen, we can now calculate the angular velocity of the instability, which, in turn, gives us the period it would take for this instability to go around the annulus. We find that this calculated period matches quite well with the observed period in the shadowgraph time-series for experiments at all $\mu$ shown in figure 5.2, suggesting that if the assumption of the observed periodic structure existing near the outer cylinder is true, the instability is always mode $m = 1$. This assumption is completely valid at lower $\mu$ as we know that it is the splash at the outer cylinder that is being represented as a periodic structure in the shadowgraph time-series. At higher $\mu$, the observed periodic event is the periodic sharpening of the interface. Since the light rays from the projector are not parallel, the sharp interface observed in the shadowgraph is mostly represented by the formation of an extremely sharp interface at the outer cylinder. Because of this, we believe that the our assumption is valid at high $\mu$ as well, and the instability at all $\mu$ is mode $m = 1$.

As discussed above, we believe that the periodic instabilities at different $\mu$ have similar structures, with period reducing at higher $\mu$.

| $\mu$ | $\mathbf{m=1}$ | | $\mathbf{m=2}$ | | $\mathbf{m=3}$ | |
|---|---|---|---|---|---|---|
| | $\sigma_\mathbf{r}$ | $\sigma_\mathbf{i}$ | $\sigma_\mathbf{r}$ | $\sigma_\mathbf{i}$ | $\sigma_\mathbf{r}$ | $\sigma_\mathbf{i}$ |
| **0.1** | 0.1636 | 0.4214 | 0.0509 | 0.7330 | 0.0043 | 0.9434 |
| **0.3** | 0.3840 | 0.7708 | 0.1243 | 1.2762 | 0.0009 | 1.3500 |
| **0.5** | 0.5633 | 0.9813 | 0.2473 | 1.7947 | 0.0926 | 2.5873 |

Table 5.1 Table showing the complex growth rate values, $\sigma$ of the mode with highest growth rate at different azimuthal wavenumbers $m$, calculated using the stability code at $Re = 1000$, $\eta = 0.4$, $\Gamma = 1$ and $Ri_B = 6$. A laminar base flow profile was used.

### 5.3.2 Linear stability analysis at $\mu > 0$

In the previous section, we discovered that a periodic instability is observed for $\mu > 0$, and the structure of this instability seems to be the same as that observed in chapter 3 for $\mu = 0$. As discussed in chapter 4, we performed linear stability analysis on the two layer STC flow using our empirical mean azimuthal flow profile at $\mu = 0$ as the base flow. We were able to predict the empirically observed instability period in our stability analysis, which suggested that the empirically observed instability has its origins in the linear instability.

In this section, we perform the linear stability analysis on the two-layer STC flow at different $\mu$. We use the same code as before, details of which are discussed in section 4.2. Since we do not have the exact empirical base flow profile, we use a laminar Taylor-Couette flow profile for these calculations. The laminar TC $u_\theta$ profile is given as

$$u_\theta = Ar + \frac{B}{r}\,, \tag{5.1}$$

where

$$A = \frac{\mu - \eta^2}{\eta(1+\eta)} \qquad \text{and} \qquad B = \frac{\eta(1-\mu)}{(1+\eta)(1-\eta^2)}\,.$$

As $\mu$ increases, the flow becomes more stable. It can be also seen in figure 5.2 that interfaces at high $\mu$ are completely stable, indicating that the flow might be laminar. Hence, we believe that using laminar TC flow profile as the base flow is a good representation of the present flow, especially at high $\mu$. The density profile is kept the same as before and can be seen in figure 4.1b. Other parameters for the present calculations are $Re = 1000$, $Ri_B = 6$, $\Gamma = 1$ and $\eta = 0.4$ (very close to the experimental value).

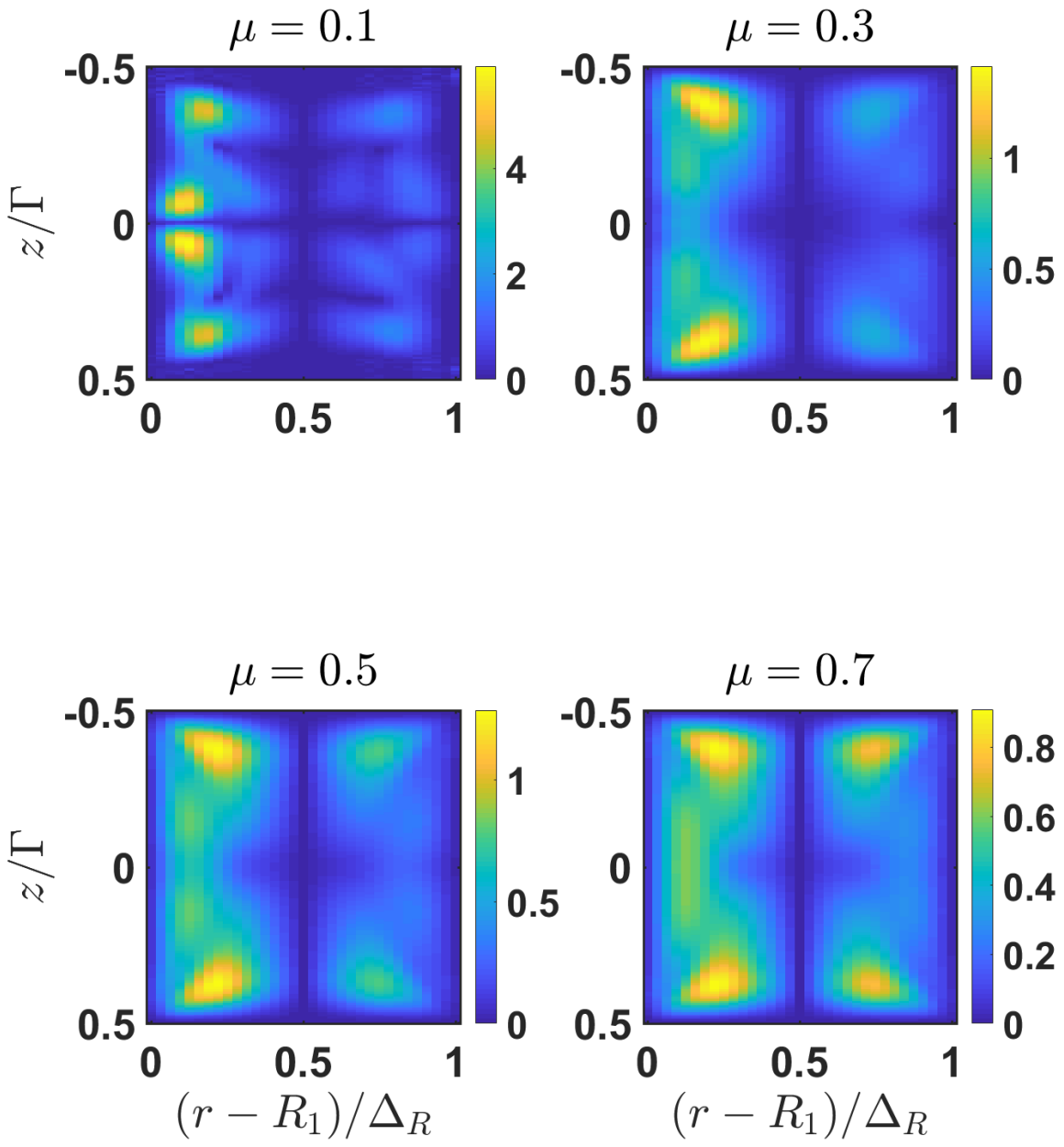


Fig. 5.6 Plot showing absolute magnitude of calculated azimuthal velocity perturbation eigenfunction,$v$ eigenfunction with varying $\mu$.

Table 5.1 shows the calculated eigenvalues for most unstable mode at different $m$. It can be clearly seen that the azimuthal wavenumber $m = 1$ is the dominant mode at all $\mu$. Figure 5.6 shows the absolute value of calculated azimuthal velocity perturbation eigenfunctions for the dominant mode at four different values of $\mu$. The structure of the eigenfunctions look the same for $\mu = 0.3$, 0.5 and 0.7, and are also similar to those observed for $\mu = 0$ using a turbulent flow profile. But the eigenfunction at $\mu = 0.1$ looks very different, both in terms of the structure and the magnitude of velocity fluctuations. We do not completely understand why the eigenfunctions at low $\mu$ using a laminar base flow profile are so different from those at high $\mu$. As discussed in section 4.3.1, the eigenfunctions at low $\mu$ are sensitive to the flow profile. Possibly, the use of a laminar base flow profile when the flow is turbulent is causing this issue. Nonetheless, the eigenfunctions at $\mu > 0.3$ show the presence of circulation cells on both sides of the interface and at both cylinder boundaries, consistent with previous observations at $\mu = 0$. It can also be seen that the relative strength of the circulation cell at the outer cylinder compared to that at the inner cylinder keeps increasing with increasing $\mu$, which possibly is responsible for the reduction of splashing as $\mu$ increases. It is also interesting to note that at $\mu = 0.3$, although the angular momentum at the outer cylinder is greater than that at the inner cylinder, the velocity fluctuations are still observed to be significantly higher near the inner cylinder, which is consistent with our observations of the presence of a splash at $\mu = 0.3$.

Looking at the eigenfunctions, it seems plausible that the instability at higher $\mu$ is similar to that observed for a turbulent flow at $\mu = 0$. To validate further, we calculate the time period of the instability using (4.21) and compare to the experimental observations. Figure 5.7 shows this comparison. The blue circles show the time period at different $\mu$ observed in shadowgraph experiments. The red squares show the predicted time period of the linear instability using the above mentioned analysis. We find a good agreement of the predicted instability time period to that observed empirically, especially at high $\mu$. It is possible the observed discrepancies at low $\mu$ are because of using a laminar base flow profile when the flow is clearly turbulent, as discussed in section 4.3.1. However, this analysis strongly suggests that the observed instability at $\mu > 0$ is the same as the one empirically observed at $\mu = 0$ (discussed in detail in chapter 3) and has its origins in a linear instability as well.

## 5.4 Discussion

In this chapter, we have looked at the implications of rotating the outer cylinder on the previously observed instability in a two-layer STC flow with fixed outer cylinder. We discover that a periodic instability does exist in the flow for $0 \leq \mu \leq 0.7$. To the best of our

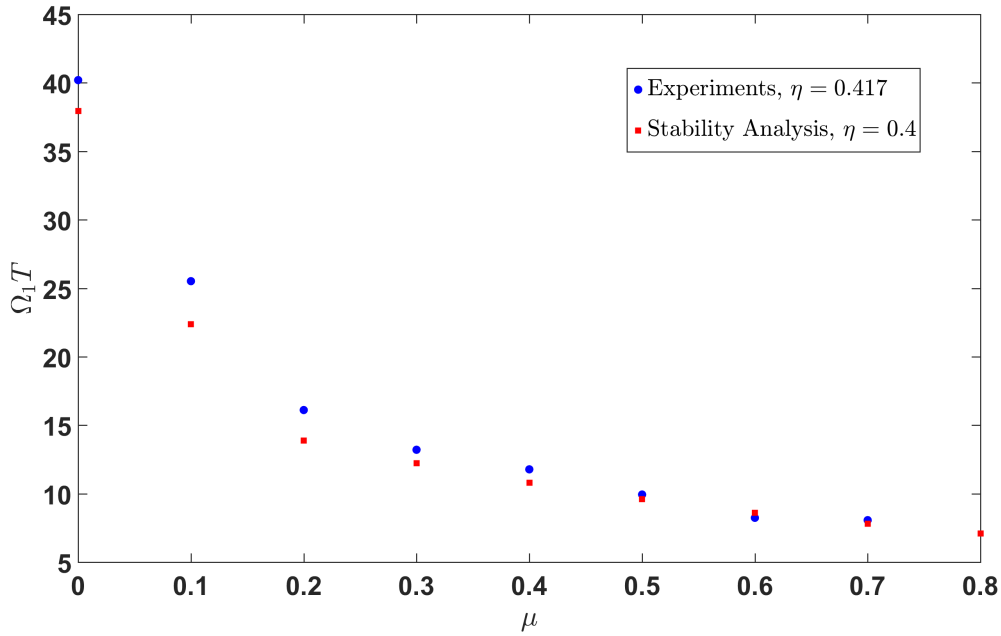


Fig. 5.7 Plot showing the time period of the observed instability in experiments (blue circles) in comparison to that predicted using linear stability analysis.

knowledge, this is the first study to discover an instability in a two-layer STC for parameters outside the range of centrifugal instability as set by Rayleigh's criterion (Rayleigh, 1917). However, unlike an initially linearly stratified STC flow, the instability appears to be the same for both the centrifugally unstable and the centrifugally stable regime. It is observed to be an azimuthal mode $m = 1$ instability for the complete range of $\mu$ that is explored.

We observe that at lower $\mu$, the instability behavior is similar to that observed at $\mu = 0$. A periodic turbulent mixing event is observed in the shadowgraph recordings, which we know, from chapter 3, represents splashing at the outer cylinder. We expected this splashing to stop when the momentum at the inner and the outer cylinders is the same i.e. $\mu = \eta^2$. However, we did observe a turbulent splash even when momentum at outer cylinder was greater than that at the inner cylinder. We found that the splashing mechanism stopped to appearing in the shadowgraph recordings at $\mu = \eta$.

Further, we performed linear stability analysis for the two-layer STC flow at different $\mu$. Since, we did not have any empirical velocity profiles at different $\mu$, we used the laminar TC profile for our analysis here. This is justified as the outer cylinder rotation stabilises the flow, and the flow might be close to laminar flow at high values of $\mu$. We found the azimuthal mode $m = 1$ to be the dominant mode, consistent with our experimental observations. Analysing the eigenfunctions, we observe circulation cells similar to those previously observed for

$\mu = 0$. We also found that the strength of the circulation cell at the outer cylinder is less than that at the inner cylinder even for $\mu > \eta^2$. This is possibly the reason for us observing turbulent splashing for $\mu > \eta^2$. Lastly, we looked at the predicted instability time period at different $\mu$. We find that the predicted time periods are consistent with those observed in the experiment. There are some discrepancies in the predicted and observed time periods at lower $\mu$ which is possibly because of using a laminar base flow when the actual flow is turbulent.

# Chapter 6

# STC at low *Pe*

## 6.1 Introduction

In this chapter, we look into the effects on the interface in a stratified Taylor-Couette flow for flows with relatively high molecular diffusion to inertia.

As discussed in chapter 2, the molecular diffusion can have a significant effect on the flow properties. The same is observed in the oceans as well. The presence of both salt and heat stratification alters the flow behaviour as compared to the flow with only one of the diffusive scalars present. For a long time, the formation of density interfaces in the oceans were specifically attributed to the presence of a double diffusive flux (Foster & Carmack, 1976; Sommer *et al.*, 2013). Although the presence of double diffusion can affect the properties of the interface, interfaces are observed in singly diffusive flows as well, like the presence of interfaces in fresh water lakes by Simpson & Woods (1970) and the interface formation in laboratory experiments as discussed in chapter 3. It is, therefore, important to understand the effect of varying diffusive property scalars separately to have a better understanding of the fluxes in the ocean and in turn, have better parameterisation of the same.

The non-dimensional number that tells us about the relative strength of advection in comparison to diffusion is called the Péclet number, and is defined as

$$Pe = \frac{ud}{\kappa} = Re\ Sc\ , \tag{6.1}$$

where

$$Re = \frac{ud}{\nu} \qquad \text{and} \qquad Sc = \frac{\nu}{\kappa}\ . \tag{6.2}$$

Here $d$ and $u$ are the flow length and velocity scales respectively and $\kappa$ is the molecular diffusivity of the scalar. At lower *Pe*, diffusion plays the dominant role in comparison to

buoyancy flux and vice-versa. In the previous chapters, we have looked into the mixing phenomenon and interface structure at high *Pe*. Here we look into the same at lower *Pe*. One could achieve a lower *Pe* either by reducing the flow *Re* or by using fluid with a lower *Sc*.

Stratified flows behave qualitatively differently at different *Sc* (Zhou *et al.*, 2016). Turner (1968), in their stratified grid mixing experiments, found that the entrainment coefficient $E$ is

$$E \propto Ri_B^{-3/2} , \qquad E \propto Ri_B^{-1} , \tag{6.3}$$

for a salt stratification and a heat stratification respectively. Later, Crapper & Linden (1974) later performed similar experiments and observed the change in flow behavior with changing *Pe*. The found that the thickness of interface decreases with increasing *Pe* in a low *Pe* regime, while in the high *Pe* regime, the interface thickness stays constant. They suggested a presence of a 'diffusive core' in the centre (away from the walls) at low *Pe*, across which the transport due to molecular diffusion occurs and the thickness of the interface is given by the balance of the diffusion across the core and the entrainment at the edges of the layers. At high *Pe*, the interface thickness stays constant as the diffusive transport is negligible and cannot balance the turbulent entrainment. This is consistent with our experimental observation, where the interface thickness largely stays constant throughout.

In this chapter, we perform experiments to study effect on the layer formation and the interface in a STC flow at relatively low *Pe*.

## 6.2 Observations and Analysis

### 6.2.1 Layer formation in STC at varying *Re*

In this section, we look at the layer formation process for initially linearly salt stratified experiments at different *Re* with keeping the *Ri* constant.

For understanding the nature of salt stratified flows, performing laboratory experiments is of utmost importance as it is very difficult to numerically simulate those flows due to high computational costs involved owing to high *Sc* of salt solutions. This is because for high *Sc* flow, in order to completely understand the flow, one has to resolve the flow down to the Batchelor scale $\lambda_B$, which goes as

$$\lambda_B \propto Sc^{-1/2} , \tag{6.4}$$

which means a much finer computational grid would be required (Lagaert *et al.*, 2012). The *Sc* for salt stratification is $Sc \sim 700$ while that for heat stratification is $Sc \sim 7$, making

simulation of salt stratified flows very computationally expensive. Hence, most simulations are done at a lower *Sc*, which is not a true representation of salt stratified flows.

However, as discussed in section 6.1, the flow behaviour in stratified flows depends on *Pe*. It is relatively less computationally expensive to achieve higher *Re* as compared to *Sc*, which can in turn give higher *Pe*. We here performed initially linearly stratified STC flow experiments with reducing *Re* to find the lowest *Pe* where robust layer formation is observed in order to open the possibility of such flows to be simulated numerically which can give us further insights on energy budgeting and help us understand the flow better.

### Experiment

The present experiments use the same Taylor-Couette apparatus as discussed in section 2.2. The inner cylinder of radius, $R_1 = 10\,\text{cm}$ is used, which means $\eta = 0.417$. The tank is filled as discussed in section 2.2.1. However, in the present case, the flow rate of each pump is continuously varied through a computer program to achieve a stable linear stratification. A polystyrene lid is used on the free surface to ensure symmetry in the boundary conditions. The conductivity probe is used to measure the fluid density and is calibrated in the same way as before (refer to section 2.2.2).

### Observations

In order to be able to compare the experiments at different *Re*, we run the experiments at a constant Richardson number, which is defined as

$$Ri = \frac{N_o^2}{\Omega^2}\ , \tag{6.5}$$

where

$$N_o = \sqrt{-\frac{g}{\rho_o}\frac{d\rho}{dz}}\ . \tag{6.6}$$

Here $g$ is the acceleration due to gravity, $\rho_o$ is the reference density and $\frac{d\rho}{dz}$ is the density gradient in the vertical direction. Oglethorpe (2014) performed initially linearly stratified STC flow experiments and did a linear fit to the observed layer heights in all her experiments. She found that the layer height $h_l$ scales as

$$h_l = (0.215\frac{U_H}{N_o} + 0.0009) \pm 0.003\ \text{m}\ , \tag{6.7}$$

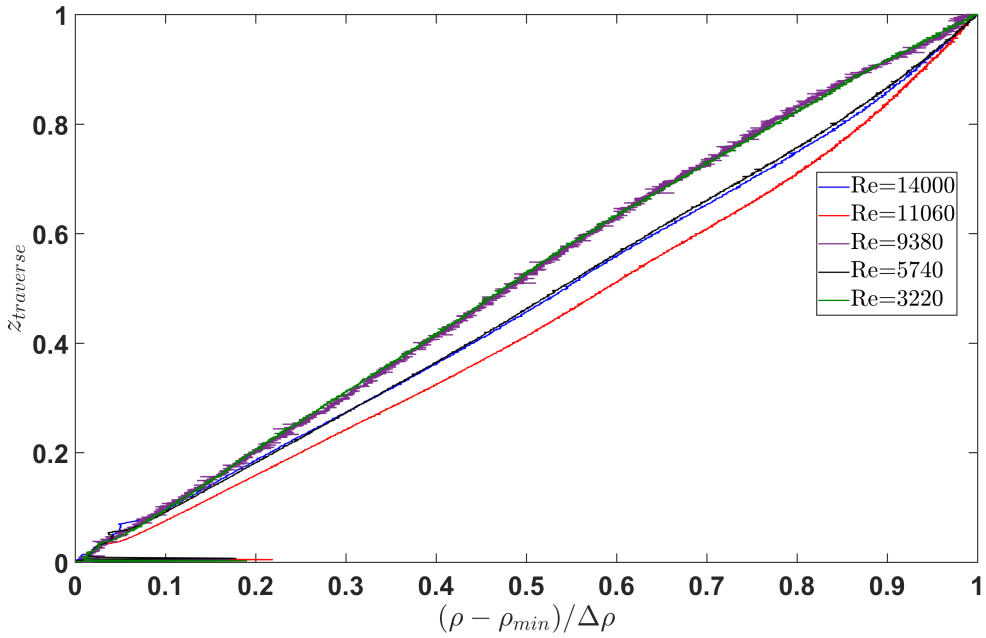


(a)

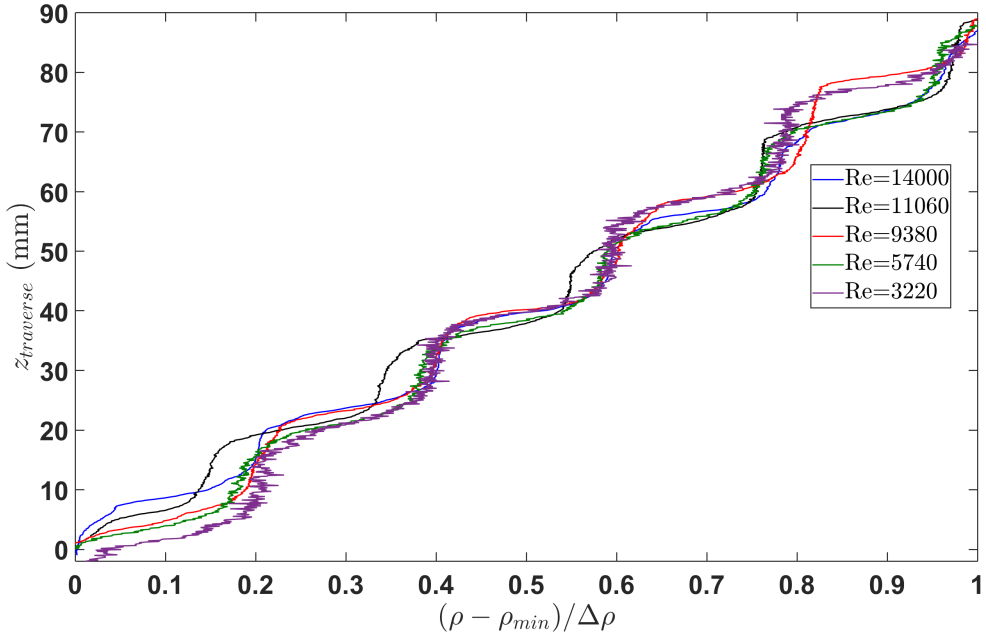


(b)

Fig. 6.1 $(a)$ Plot showing initial stratification profile for five different experiments at different *Re*. $(b)$ Plot showing density profiles after 300 rotation periods of the inner cylinder for the experiments at different *Re*. Layer formation is observed at all *Re*.

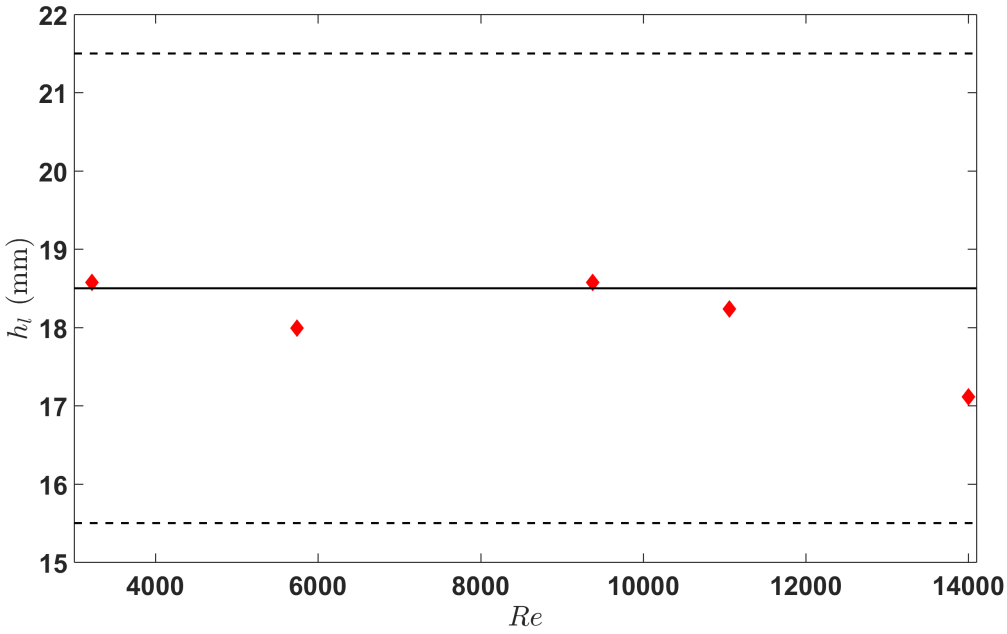


Fig. 6.2 Plot showing average layer height observed in the time frame of 300-500 rotation periods for each experiment. The red diamonds are the layer height results from the Fourier transform of the signal. The black solid and dashed lines represent the mean layer height and the standard deviations respectively observed by Oglethorpe (2014).

where $U_H = \sqrt{\Delta_r r_i}$ is the horizontal velocity scale. Keeping $Ri$ constant also ensures $\frac{U_H}{N_o}$ to be constant, which means the observed $h_l$ in present experiments could be compared with Oglethorpe's scaling. The $Ri$ for all experiments is kept at $Ri \approx 4.7$ by varying the $N_o$ for each experiment. Five different experiments are performed at five different $Re =$ 14000, 11060, 9380, 5740, and 3220.

Figure 6.1a shows the initial density profiles for each experiment. The profiles look linear to a good approximation. We looked at the layer formation in the experiments after 300 rotation periods of the inner cylinder in order to ensure that the layers are fully developed. Figure 6.1b shows the density profiles after 300 rotation periods. Layer formation is observed for experiments at all $Re$ and the layer height looks similar for all $Re$. Now to compare the observed layer heights with the scaling provided by Oglethorpe (2014), we take the mean of density profiles in a time-frame of 300-500 rotation periods. Then, after removing the linear trend, we perform fast Fourier transform on the signal which gave us the layer height for each $Re$ experiment. Figure 6.2 shows the observed layer height at different $Re$. The black solid line represents the mean layer height from Oglethorpe's scaling and the dashed lines represent the standard deviation. The observed layer heights at all $Re$ are well within the standard deviation range, which suggests that the layer formation process is robust at-least

for $Re \geq 3220$. To note here that the observed interface formation at $Re \approx 3000$ justifies us performing the stability analysis at $Re = 3000$ as discussed in chapter 4.

### 6.2.2 Interface at low *Pe*

In this section, we look into how the interface is affected in an experiment with high molecular diffusion in comparison to inertia i.e. at low *Pe*.

#### Experiment

We use the same TC setup for these experiments as before (refer to section 2.2.) The inner cylinder of radius, $R_1 = 10$ cm is used. The tank is filled as discussed in section 2.2.1. For the heat experiments, we wrap the outside of the apparatus with a thermal insulating material in order to minimise the heat diffusion into the surroundings. A small window is kept uncovered for the camera to visualise the flow. The inner cylinder is painted white and acts as a screen for shadowgraph experiments. A polystyrene lid is used on the free surface to ensure symmetry in the boundary conditions and to provide thermal insulation from the top as well. The thermistor mounted on the traverse is used to measure the temperature in heat stratified experiments, while a conductivity probe is used to measure density in salt stratified experiments.

#### Observations

We perform STC experiments using heat as the diffusing scalar with $Sc \sim 7$. Although the idea was to have a two-layer experiment, because of the high diffusion of heat, in the time it took to fill the tank, the interface grows to almost 25% of the height of fluid in the tank. The tank is filled to a height of 42 cm, with fresh water at $\approx 25\,^{\circ}$C in the lower layer and that at $\approx 40\,^{\circ}$C in the upper layer. The inner cylinder is rotated at $0.5\,\mathrm{rad\,s^{-1}}$ which gives $Re = 7000$ and starting $Ri_B \approx 10$. After every 40 s, the thermistor traverses through the flow to get the temperature profile. The recorded temperature profiles over time can be seen in figure 6.5. It can be seen that the mean temperature reduces over time, which is because of heat diffusing out into the surroundings.

As discussed in chapter 2, for the experiments with salt solution, the diffused interface during the tank filling process sharpens as turbulence is generated in the layer. However, for the present heat experiments, we did not observe the sharpening of the interface as the cylinder is rotated. At the same time, despite high molecular diffusion, the thickness of the interface stays constant throughout the experiment. Figure 6.3 shows the variation of the interface thickness calculated from the temperature profiles as the vertical distance over

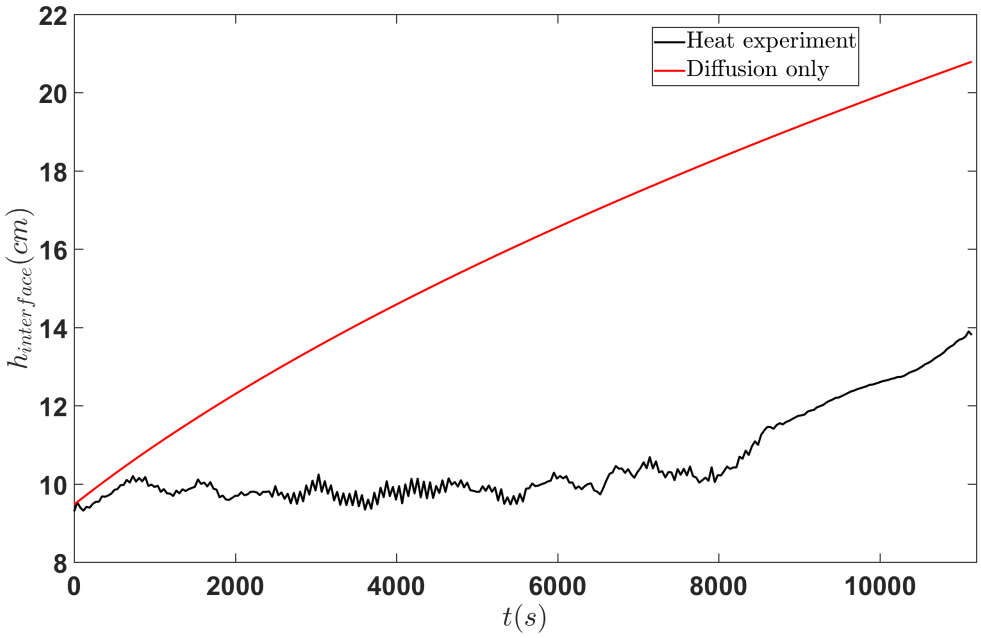


Fig. 6.3 Plot showing the observed interface thickness for a heat stratified STC experiment over time. The red curve is the predicted interface thickness if it was to grow by diffusion only.

which temperature spread is 90% of the total temperature difference in the two layers. The red curve represents the interface thickness if the interface was growing by diffusion only, in the absence of turbulence. The cylinder was made to stop rotating around 8000 s and the interface starts to grow again owing to heat diffusion. The rate of increase of the interface thickness here is consistent with that of diffusion only. These observations are consistent with that of Crapper & Linden (1974) at low *Pe*. This is consistent with their argument that the thickness of the interface is decided by the balance of diffusion and mechanical turbulent transport.

In order to investigate this further, we perform two separate heat STC experiments with the same parameters, where for one the thermistor is made to traverse in the middle of the annular gap, while for the other it is made to traverse near the outer cylinder boundary. Since the interface diffuses significantly during the tank filling process itself, there exists a region in the middle where the stratification is close to linear. From our observations in salt stratified experiments, one would expect the formation of layers and interface in this region. The observed temperature profiles for both experiments are shown in figure 6.5. The colour in the plots represents time, where blue represents time near the start of the experiment while maroon represents the end of the experiment. We observe the formation of layers and interfaces near the outer cylinder while there is no obvious trace of layer formation in

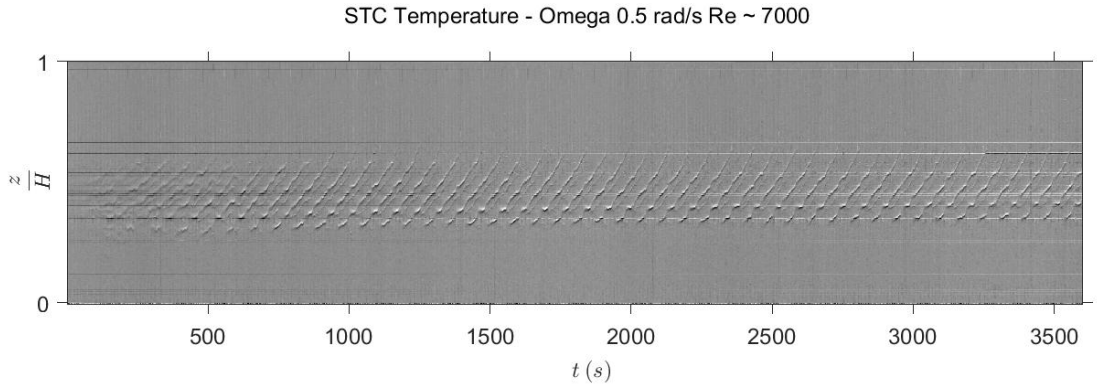


Fig. 6.4 Plot showing time-series of a vertical slice from the shadowgraph recordings in a heat stratified STC experiment.

the middle of the annulus gap. This is consistent with observations of Crapper & Linden (1974) (referring to figure 3a in their paper). They argued a presence of a 'diffusive core' in the middle where heat diffusion occurs. In order to have a quasi-steady state, the diffusive flux is balanced by the presence of entrainment flux near the walls where the temperature gradient goes to zero. We believe that the same argument is valid for the heat STC as well. A 'diffusive core' exists in the middle of the annulus and since the interface thickness stays constant, the diffusive flux is being balanced by vertical transport by turbulence. It is this turbulent flow near the boundaries that is causing the formation of interfaces that is observed near the outer cylinder.

Further, we perform a shadowgraph experiment to look into the structure of the interface. Figure 6.4 shows the time-series of a vertical slice from the shadowgraph recordings. The layer formation is observed here as well. However, the interfaces are seen to continuously drift upwards. On closer observation, we find that the interface drifts upwards and then stays at a location for a small duration, trying to form a stable interface as observed in salt experiments. Analysing it further, we find that the observed time-period in figure 6.4 is consistent with the scaling provided by Oglethorpe (2014) (refer to equation (3.2)). Moreover, using the analysis described in section 5.3.1, we find that the periodicity here exhibits azimuthal mode $m = 1$ as well. This suggests that the same instability, as observed for salt-stratified STC experiments, exists for heat stratification as well, however, the diffusion dominates at lower *Pe* and results in a visibly different flow behaviour.

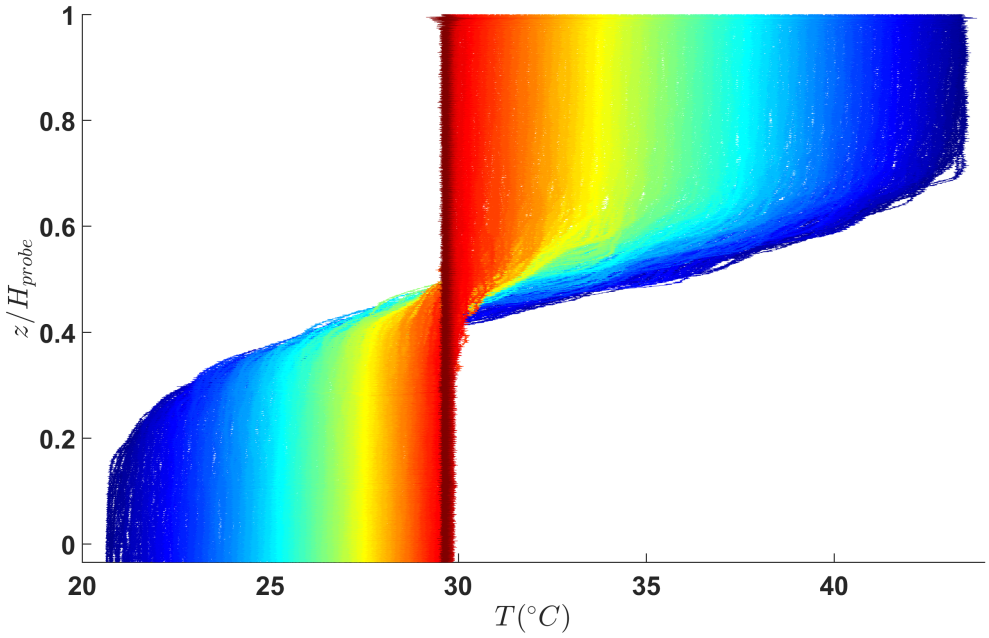


(a)

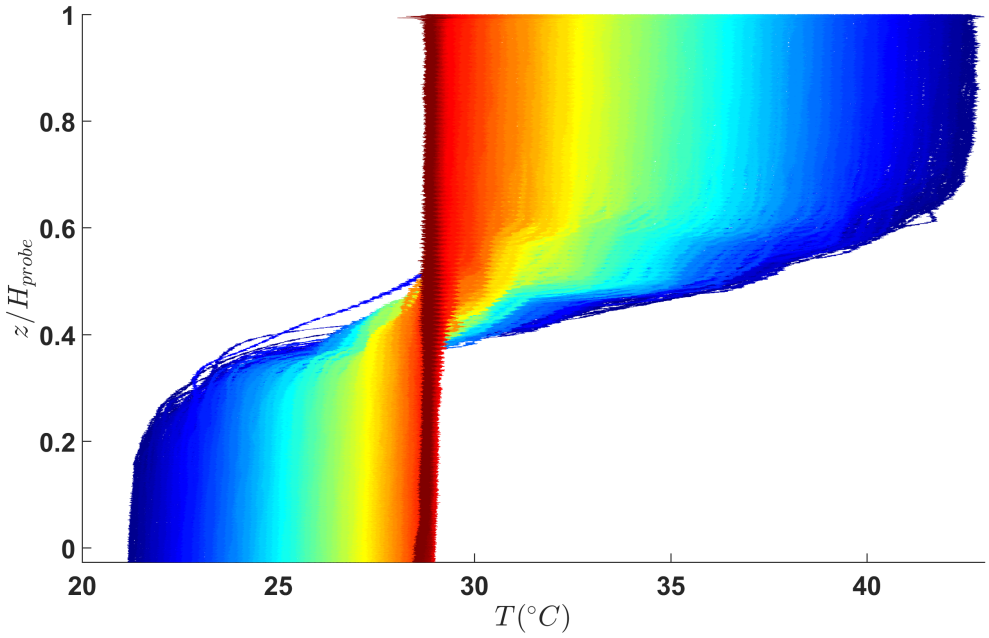


(b)

Fig. 6.5 Plot showing evolution of density profiles over time with a thermistor traversing $(a)$ in the middle of the annular gap, and $(b)$ near the outer cylinder. The colour of the profiles represent the time, with blue being the profile at the start of the experiment and maroon being the profile near the end.

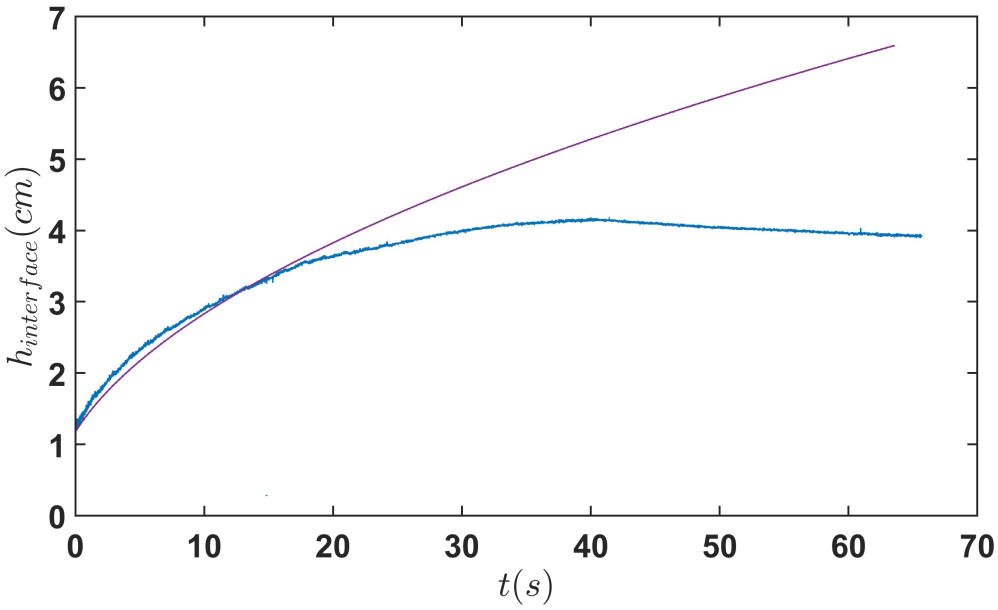


Fig. 6.6 Plot showing the observed interface thickness for a salt stratified STC experiment at low $Re = 4220$ and a starting $Ri_B \approx 340$, over time. The purple curve is the predicted interface thickness if it was to grow by diffusion only.

So far, the experiments discussed were performed at low $Sc$. In order to confirm that the argument of Crapper & Linden (1974) at low $Pe$ is completely valid for STC as well, we perform an experiment with salt stratification but at low $Re$ and high $Ri_B$, ensuring a high diffusion flow regime. The same TC apparatus as mentioned above is used. The inner cylinder is rotated at $0.3\,\mathrm{rad\,s^{-1}}$ which gives $Re = 4200$. The tank is filled with salt water solution and fresh water such that starting $Ri_B \sim 340$. Since we were using salt as the scalar with $Sc = 700$, we were able to fill the tank with a sharp interface.

We observe that the interface does not stay sharp as in the experiments discussed in chapter 2. Figure 6.6 shows the observed interface thickness over time. The purple line shows the predicted interface thickness if it was growing by just diffusion. We find that the interface thickness starts to increase at the start of the experiment. The rate of increase of the interface thickness is consistent with the interface growing by diffusion only. The interface thickness grows to a maximum and stays constant later throughout the experiment. As the diffusion was dominating the flow, the interface thickness kept growing and it stayed constant when the balance of the diffusion and turbulent entrainment is achieved, consistent with Crapper & Linden (1974).

## 6.3 Discussion

In this chapter, we have looked into some different STC experiments at low *Pe*. We performed initially linearly stratified STC experiments at a range of *Re* to find the lowest *Re* where the flow is dynamically similar, in order to open up the possibility of that being numerically simulated. We observe a robust layer formation for the complete range of *Re*, the lowest being $Re = 3220$.

We then looked at the implications on the interface in a two-layer STC in a high diffusing regime i.e. low *Pe*. We performed experiments using heat where the interface had already diffused during the time of filling the tank. We found that as the experiment was started, the interface thickness stayed constant and started to increase again when the experiment was stopped. We also performed a salt stratification experiment with extremely high $Ri_B$ ensuring the flow to be in a diffusive regime. We found that the interface thickness grew initially at the same rate as predicted as if growing by diffusion only. However, at some point, it stops growing and the interface thickness stays constant beyond that point. These results were consistent with the argument by Crapper & Linden (1974) that for low *Pe* experiments where they suggested that at low *Pe*, there exists a competition between diffusion and turbulent transport, which decides the layer thickness.

# Chapter 7

# Conclusions and future work

The aim of this PhD project was to provide further insights into the previously observed periodic mixing process across the interface in a stably stratified centrifugally unstable turbulent Taylor-Couette flow and, in turn, increase our understanding of turbulent mixing in horizontally sheared stratified environments with direct relevance to ocean mixing. We reviewed the literature and identified open questions about the mixing phenomenon in a stratified Taylor-Couette (STC) flow. In particular, we addressed four questions in this thesis: explaining the observed (Oglethorpe, 2014) change in flow behaviour in STC (a horizontally sheared stratified flow) resulting in a change in buoyancy flux at a specific critical bulk Richardson number ($Ri_B$) in contrast to other stratified flow studies; determining the structure of the periodic mixing instability; providing explanations about the origins of this instability; and if this instability would persist in a centrifugally stable environment. In this chapter, we will review the results described in the previous chapters, and provide some directions for future research.

### 7.0.1 Conclusions

In order to further investigate the Oglethorpe *et al.* (2013)'s universal flux curve, we conducted laboratory experiments, starting at a high $Ri_B$, to study buoyancy flux across the interface in a two-layer stratified STC. We observed that the total flux curve is consistent with Oglethorpe's universal flux curve. However, analysing further we found that the total observed flux has a significant contribution from the diffusive flux, especially at high $Ri_B$ and the actual buoyancy flux is a monotonically decreasing function with increasing $Ri_B$ (except at very low $Ri_B$ where the interface overturns and the fluid mixes completely). Hence, Oglethorpe's universal flux curve is not a correct representation of buoyancy flux in a STC flow. These experiments are discussed in chapter 2. Through fitting a power law, we also found the actual buoyancy flux

goes as $\hat{F} \sim Ri^{-0.5}$, which suggests that the entrainment coefficient in the flow is $E \sim Ri^{-1.5}$. This is consistent with the results of Turner (1968) for their salt stratified experiments with grid-mixing.

Moreover, since the buoyancy flux is a monotonically decreasing function of $Ri_B$, it satisfies the pre-requisite for the 'Phillips mechanism', which states that a small perturbation from linear stratification will continue to grow, if the vertical buoyancy flux is decreasing with increasing density gradient. This means that any perturbation in an initially linearly stratified STC that causes the increase in density gradient will be amplified, which leads to a layer formation. This suggests that the layer formation by the 'Phillips mechanism' is preferred in an initially linearly stratified STC flow.

We also conducted experiments to discover the structure of the periodic mixing event previously observed by Oglethorpe (2014). Through simultaneous LIF and PIV, we found that an instability in the form two in-phase boundary trapped mode waves on the density interface, with azimuthal mode $m = 1$, one at each cylinder boundary results in mixing. Owing to these waves, the interface periodically goes through a series of events. It starts with an interface of constant thickness throughout the radial gap. As these waves pass, they result in the formation of extremely sharp interfaces near both cylinder boundaries. The extent of these extremely sharp interfaces then grows further into the annulus. This suppresses the mixed fluid region in the middle of the annulus. At the same time, high shear in the inner cylinder boundary layer results in the formation of mixed fluid parcels which are continuously ejected along the interface into the annulus. These parcels are entrained into the mixed fluid region, increasing its momentum and causing it to move out towards the outer cylinder. This causes the mixed fluid region to splash onto the outer cylinder boundary and move vertically as an intrusive gravity current in both the layers. From PIV results, we found an increase in azimuthal velocity during the splash. The stable stratification then starts to act and produces a buoyant force to suppress this vertical fluid motion. This pushes the mixed fluid region back towards the inner cylinder, resulting in a constant thickness interface again. This process continues periodically throughout and results in the observed mixing. These experiments are discussed in chapter 3.

We further discussed the implications on this mixing mechanism with reducing $Ri_B$. We provided an interpretation of the observed enhanced flux at lower $Ri_B$. Through analysing LIF and PIV data, we found that with reducing $Ri_B$, the extent of the extremely sharp interface goes increasingly further into the annulus, resulting in a much smaller mixed fluid region. At the same time, the strength of the periodic enhancement of azimuthal velocity during the splashing process decreases with decreasing $Ri_B$. Further analysis suggested that there are two phenomena that result in vertical mixing: 'scouring', where large scale turbulent eddies

in each layer cause mixing in the regions where $Ri$ reduces locally due to perturbations on the interface; and 'splashing' which causes vertical fluid motion at the outer cylinder boundary and subsequent homogenisation by turbulent eddies. Although we found the flow to have enhanced scouring on the interface with reducing $Ri_B$ (due to increased interface thickness), the increased extent of extremely sharp interface into the annulus results in reduction of area over which scouring could take place. On the other hand, with reducing $Ri_B$, a much stronger splashing is observed. This is consistent with the reduced strength of the periodic azimuthal velocity enhancements with reducing $Ri_B$. This suggested that the enhanced flux observed at lower $Ri_B$ results from enhanced splashing.

In chapter, 4, we presented results from a linear stability analysis for a two-layer STC flow using a base flow with both $r$ and $z$ dependence. We use the empirically observed turbulent mean velocity profile varying in $r$ and a two-layer density profile varying in $z$, as our base flow. We found the azimuthal mode $m = 1$ is the dominant mode whose period is independent of $Ri_B$, consistent with the experimental observations. Furthermore, we also consistently predicted the time-period of the instability at different $\eta$ from Oglethorpe's scaling. This strongly suggests that the empirically observed instability in an inherently turbulent STC flow has its origins in a linear instability. In addition, we also provided a hypothesis for observed coupling with the adjacent interfaces formed in initially linearly stratified STC flow. We hypothesise that at the start of experiment, when the flow has not achieved a fully turbulent state, an SRI-like helical mode sets in the perturbations which are amplified by the 'Phillips mechanism' and forms the layers at a specific characteristic height. Now, on each of the interfaces, there exists the above discussed azimuthal mode $m = 1$ instability.

We also looked at the implications of rotating the outer cylinder on the previously observed instability on the interface in a two-layer STC with fixed outer cylinder. We discovered that same azimuthal $m = 1$ instability exists at all $\mu$ explored ($0 \leq \mu \leq 0.7$), with reducing time period at higher $\mu$. We also performed linear stability analysis on a two-layer STC flow at different $\mu$. We again found the azimuthal mode $m = 1$ to be the dominant mode and were able to consistently predict the observed time period at all $\mu$. This suggests that the instability on the interface in a two-layer STC flow is always a linear instability. The experiments and stability calculation results are discussed in chapter 5.

Lastly, we conducted experiments, discussed in chapter 6, to look into the layer formation process in an initially linearly stratified STC at low $Re$ and have found the layer formation is a robust phenomena for all $Re > 3220$. We also looked at the implications on the interface in STC flow with high diffusion properties (i.e. low $Pe$) through a two-layer STC flow experiments using heat stratification and another with salt stratification at low $Re$. We found

that there exists a competition between diffusion and turbulent transport that decides the interface thickness, consistent with Crapper & Linden (1974).

### 7.0.2 Directions for future work

In this thesis, we have looked at the mixing mechanism across the interface in a two-layer STC. From our quantitative horizontal plane measurements, we believe that the observed enhanced flux at low $Ri_B$ (refer to figure 2.10) is because of the enhanced splashing that occurs as $Ri_B$ reduces. In order to validate this experimentally, quantitative measurements in the vertical plane are required which were not possible in the present setup owing to the refractive index variations due to the curvature of the outer cylinder. Thus placing the outer cylinder in a rectangular transparent enclosure, filled with water, would remove the effects of refractive index variation. This would provide better insights into the splashing mechanism and in turn, the overall mixing process. This setup would also make it possible to have three-dimensional PIV measurements of the flow. The data could then provide further information on the rate of input and dissipation of kinetic energy, allowing for the measurement of mixing efficiency or $R_f$ directly. These could then be compared to other stratified flow experiments to check for universality in different stratified turbulent flows. Performing three-dimension numerical simulations for a two-layer STC would also be useful, however, it would be quite computationally expensive the at high $Re$ and $Sc$ required to match the experiments.

Talking about universality, it would also be interesting to perform STC experiment in an apparatus with a small annular gap width, i.e. $\eta \approx 1$, to have a direct comparison to horizontally sheared plane Couette flow, which is closely analogous to the flow in oceans. Similarly, it would also be interesting to understand the STC behaviour with a large annular gap, which can have relevance in understanding flow behaviour in astrophysical disks. The present experiments, and that of Oglethorpe (2014), were performed only at moderate values of $\eta$. From our linear stability calculations for the two-layer STC, which were performed over a wide range of $\eta$, we find that the eigenfunctions for small $\eta$ look significantly different from those at high $\eta$. This is especially prominent for $\eta < 0.2$ and can be seen in figure 4.11. At the same time, the calculated time period for $\eta < 0.2$ also diverges quite significantly from the empirical scaling provided by Oglethorpe (2014). This suggests a change of instability behaviour and possibly the mixing mechanism at small $\eta$. Therefore, performing experiments with a wide annular gap apparatus would be useful in understanding this change of flow behaviour.

An unstratified Taylor-Couette flow is known to show a wide variety of flow regimes at different inner and outer cylinder Reynolds numbers (refer to figure 1.2). However, this range

is still unexplored for STC. We performed some two-layer STC experiments with the inner cylinder rotating at $\Omega_1 = 1\,\mathrm{rad\,s^{-1}}$ while changing the rotation speed of the outer cylinder i.e. varying $\mu$. Using the shadowgraph visualisation technique, we find that the azimuthal mode $m = 1$ instability does exist for $\mu > 0$, similar to that observed in a purely centrifugally unstable case ($\mu = 0$). It would be interesting to explore the flow behaviour over the range of initial conditions ($\Omega_1, \Omega_2, R_1, R_2, \Delta_R$ and/or $\Delta\rho_0$) and develop a flow regime curve for a two-layer STC similar to that in figure 1.2. Moreover, the flow regimes in initially linearly stratified STC, or more exotic initial density profiles, also remain relatively unexplored and would be an interesting avenue for further research. The data from the above study can also help understand what determines the length scale embedded in $Ri_B$ (i.e. $R_2$) which was identified by Oglethorpe (2014).

In this thesis, we provide a good understanding of the mixing instability and the resulting mixing mechanism in the two-layer STC, it is still unclear what sets the observed layer height in an initially linearly stratified STC. The mechanism behind the observed coupling of the mixing instability between the adjacent so-formed layers is also unknown. Oglethorpe (2014) found that the layers formed in an initially linearly stratified STC depends upon $R_1$ and $\Delta_R$. Thus, it would be interesting to explore the flow over a range of various geometric conditions to get a better understanding of the layering process. Future experiments could also use a rotating frustum in place of the inner cylinder or an inner cylinder with varying roughness to study how the size of the layers changes with the vertical changes in the boundary that generates the flow.

Based on our understanding of the STC, we hypothesised that the resonance of SRI-like helical modes is what is causing the initial perturbation to the density field which gets intensified via the 'Phillips mechanisms' and forms layers. A separate $m = 1$ instability then rides on these interfaces. Since SRI is known to be a linear instability, it would be good to look into the linear stability analysis of a linearly stratified STC using a turbulent base flow to predict the observed layer height. This could give us the mathematical understanding of the layer formation process.

# Bibliography


ALFORD, MATTHEW H, GIRTON, JAMES B, VOET, GUNNAR, CARTER, GLENN S, MICKETT, JOHN B & KLYMAK, JODY M 2013 Turbulent mixing and hydraulic control of abyssal water in the samoan passage. *Geophysical Research Letters* **40** (17), 4668–4674.

ANDERECK, C DAVID, LIU, SS & SWINNEY, HARRY L 1986 Flow regimes in a circular couette system with independently rotating cylinders. *Journal of Fluid Mechanics* **164**, 155–183.

AVILA, MARC, GRIMES, MATT, LOPEZ, JUAN M & MARQUES, FRANCISCO 2008 Global endwall effects on centrifugally stable flows. *Physics of Fluids* **20** (10), 104104.

BALMFORTH, NJ, SMITH, STEFAN G LLEWELLYN & YOUNG, WR 1998 Dynamics of interfaces and layers in a stratified turbulent fluid. *Journal of Fluid Mechanics* **355**, 329–358.

BARENBLATT, GI, BERTSCH, M, DAL PASSO, R, PROSTOKISHIN, VM & UGHI, MAURA 1993 A mathematical model of turbulent heat and mass transfer in stably stratified shear flow. *Journal of Fluid Mechanics* **253**, 341–358.

BLUTEAU, CE, JONES, NL & IVEY, GN 2013 Turbulent mixing efficiency at an energetic ocean site. *Journal of Geophysical Research: Oceans* **118** (9), 4662–4672.

BOUBNOV, BM, GLEDZER, EB & HOPFINGER, EJ 1995 Stratified circular couette flow: instability and flow regimes. *Journal of Fluid Mechanics* **292**, 333–358.

BÜCHEL, P, LÜCKE, M, ROTH, D & SCHMITZ, R 1996 Pattern selection in the absolutely unstable regime as a nonlinear eigenvalue problem: Taylor vortices in axial flow. *Physical Review E* **53** (5), 4764.

CATON, FRANÇOIS, JANIAUD, BÉATRICE & HOPFINGER, EJ 1999 Primary and secondary hopf bifurcations in stratified taylor-couette flow. *Physical review letters* **82** (23), 4647.

CATON, FRANÇOIS, JANIAUD, BÉATRICE & HOPFINGER, EJ 2000 Stability and bifurcations in stratified taylor–couette flow. *Journal of Fluid Mechanics* **419**, 93–124.

CHANDRASEKHAR, SUBRAHMANYAN 1961 *Hydrodynamic and hydromagnetic stability*. Courier Corporation.

CHANG, YC & MYERSON, AS 1985 The diffusivity of potassium chloride and sodium chloride in concentrated, saturated, and supersaturated aqueous solutions. *AIChE journal* **31** (6), 890–894.

CLARK, MATTHEW 2011 *Handbook of textile and industrial dyeing: principles, processes and types of dyes*. Elsevier.

COLES, DONALD 1965 Transition in circular couette flow. *Journal of Fluid Mechanics* **21** (03), 385–425.

COUETTE, MAURICE 1890 Etudes sur le frottement des liquides. PhD thesis.

CRAPPER, PF & LINDEN, PF 1974 The structure of turbulent density interfaces. *Journal of Fluid Mechanics* **65** (1), 45–63.

DEARDORFF, JW & YOON, S-C 1984 On the use of an annulus to study mixed-layer entrainment. *Journal of Fluid Mechanics* **142**, 97–120.

DI PRIMA, RC & SWINNEY, HARRY 1985 Instabilities and transition in flow between concentric rotating cylinders. *Hydrodynamic instabilities and the transition to turbulence* pp. 139–180.

DONNELLY, RUSSELL J 1991 Taylor-couette flow: The early days. *Physics Today* **44** (11), 32–39.

DUBRULLE, B, MARIE, LOUIS, NORMAND, CH, RICHARD, D, HERSANT, F & ZAHN, J-P 2005 A hydrodynamic shear instability in stratified disks. *Astronomy & Astrophysics* **429** (1), 1–13.

EDEN, CARSTEN, CZESCHEL, LARS & OLBERS, DIRK 2014 Toward energetically consistent ocean models. *Journal of Physical Oceanography* **44** (12), 3160–3184.

ELLISON, TH & TURNER, JS 1959 Turbulent entrainment in stratified flows. *Journal of Fluid Mechanics* **6** (3), 423–448.

FERRARI, RAFFAELE & WUNSCH, CARL 2009 Ocean circulation kinetic energy: Reservoirs, sources, and sinks. *Annual Review of Fluid Mechanics* **41**, 253–282.

FOSTER, THEODORE D & CARMACK, EDDY C 1976 Temperature and salinity structure in the weddell sea. *Journal of Physical Oceanography* **6** (1), 36–44.

GROSSMANN, SIEGFRIED, LOHSE, DETLEF & SUN, CHAO 2016 High–reynolds number taylor-couette turbulence. *Annual review of fluid mechanics* **48**, 53–80.

GUYEZ, ESTELLE, FLOR, J-B & HOPFINGER, EJ 2007 Turbulent mixing at a stable density interface: the variation of the buoyancy flux–gradient relation. *Journal of Fluid Mechanics* **577**, 127–136.

HOEPFFNER, JÉRÔME 2007 Implementation of boundary conditions.

HOLBROOK, W STEVEN & BLACIC, TANYA M 2010 First images and orientation of fine structure from a 3-d seismic oceanography data set. *Ocean Science* **6** (2), 431.

HOLFORD, JOANNE M & LINDEN, PF 1999 Turbulent mixing in a stratified fluid. *Dynamics of atmospheres and oceans* **30** (2), 173–198.

HUA, BACH LIEN, LE GENTIL, SYLVIE & ORLANDI, PAOLO 1997 First transitions in circular couette flow with axial stratification. *Physics of Fluids* **9** (2), 365–375.

HUISMAN, SANDER G, SCHARNOWSKI, SVEN, CIERPKA, CHRISTIAN, KÄHLER, CHRISTIAN J, LOHSE, DETLEF & SUN, CHAO 2013 Logarithmic boundary layers in strong taylor-couette turbulence. *Physical review letters* **110** (26), 264501.

IBANEZ, RUY, SWINNEY, HARRY L & RODENBORN, BRUCE 2016 Observations of the stratorotational instability in rotating concentric cylinders. *Physical Review Fluids* **1** (5), 053601.

IPCC 2013 Ipcc, 2013: summary for policymakers in climate change 2013: the physical science basis, contribution of working group i to the fifth assessment report of the intergovernmental panel on climate change.

IVEY, GN, WINTERS, KB & KOSEFF, JR 2008 Density stratification, turbulence, but how much mixing? *Annu. Rev. Fluid Mech.* **40**, 169–184.

JAYNE, STEVEN R 2009 The impact of abyssal mixing parameterizations in an ocean general circulation model. *Journal of Physical Oceanography* **39** (7), 1756–1775.

KATO, H & PHILLIPS, OM 1969 On the penetration of a turbulent layer into stratified fluid. *Journal of Fluid Mechanics* **37** (04), 643–655.

KOSCHMIEDER, EL 1979 Turbulent taylor vortex flow. *Journal of Fluid Mechanics* **93** (03), 515–527.

LAGAERT, JEAN-BAPTISTE, BALARAC, GUILLAUME, COTTET, GEORGES-HENRI & BÉGOU, PATRICK 2012 Particle method: an efficient tool for direct numerical simulations of a high schmidt number passive scalar in turbulent flow. In *Summer Program 2012. Center of Turbulence Research*, pp. 167–176.

LATHROP, DANIEL P, FINEBERG, JAY & SWINNEY, HARRY L 1992 Turbulent flow between concentric rotating cylinders at large reynolds number. *Physical review letters* **68** (10), 1515.

LE BARS, MICHAEL & LE GAL, PATRICE 2007 Experimental analysis of the stratorotational instability in a cylindrical couette flow. *Physical review letters* **99** (6), 064502.

LECLERCQ, COLIN, NGUYEN, FLORIAN & KERSWELL, RICH R 2016*a* Connections between centrifugal, stratorotational, and radiative instabilities in viscous taylor-couette flow. *Physical Review E* **94** (4), 043103.

LECLERCQ, COLIN, PARTRIDGE, JAMIE L, AUGIER, PIERRE, CAULFIELD, COLM-CILLE P, DALZIEL, STUART B & LINDEN, PAUL F 2016*b* Nonlinear waves in stratified taylor–couette flow. part 1. layer formation. *arXiv preprint arXiv:1609.02885* .

LECLERCQ, COLIN, PARTRIDGE, JAMIE L, AUGIER, PIERRE, DALZIEL, STUART B & KERSWELL, RICH R 2016*c* Using stratification to mitigate end effects in quasi-keplerian taylor–couette flow. *Journal of Fluid Mechanics* **791**, 608–630.

LEWIS, GREGORY S & SWINNEY, HARRY L 1999 Velocity structure functions, scaling, and transitions in high-reynolds-number couette-taylor flow. *Physical Review E* **59** (5), 5457.

LILLY, DOUGLAS K 1983 Stratified turbulence and the mesoscale variability of the atmosphere. *Journal of the Atmospheric Sciences* **40** (3), 749–761.

LINDEN, PF 1979 Mixing in stratified fluids. *Geophysical & Astrophysical Fluid Dynamics* **13** (1), 3–23.

LINDEN, PF 1980 Mixing across a density interface produced by grid turbulence. *Journal of Fluid Mechanics* **100** (04), 691–703.

MOLEMAKER, M JEROEN, MCWILLIAMS, JAMES C & YAVNEH, IRAD 2001 Instability and equilibration of centrifugally stable stratified taylor-couette flow. *Physical review letters* **86** (23), 5270.

MORTON, BR, TAYLOR, GEOFFREY INGRAM & TURNER, JOHN STEWART 1956 Turbulent gravitational convection from maintained and instantaneous sources. *Proceedings of the Royal Society of London. Series A. Mathematical and Physical Sciences* **234** (1196), 1–23.

MUNK, WALTER & WUNSCH, CARL 1998 Abyssal recipes ii: energetics of tidal and wind mixing. *Deep Sea Research Part I: Oceanographic Research Papers* **45** (12), 1977–2010.

MUNK, WALTER H 1966 Abyssal recipes. In *Deep Sea Research and Oceanographic Abstracts*, , vol. 13, pp. 707–730. Elsevier.

NARIMOUSA, SIAVASH & FERNANDO, HARINDRA JS 1987 On the sheared density interface of an entraining stratified fluid. *Journal of Fluid Mechanics* **174**, 1–22.

OGLETHORPE, RLF 2014 Mixing in stably stratified turbulent taylor–couette flow. PhD thesis, DAMTP, University of Cambridge.

OGLETHORPE, RLF, CAULFIELD, CP & WOODS, ANDREW W 2013 Spontaneous layering in stratified turbulent taylor–couette flow. *Journal of Fluid Mechanics* **721**, R3.

OLSTHOORN, JASON 2017 On vortex rings impacting a sharply–stratified interface. PhD thesis, DAMTP, University of Cambridge.

PARK, JUNHO & BILLANT, PAUL 2013 The stably stratified taylor–couette flow is always unstable except for solid-body rotation. *Journal of Fluid Mechanics* **725**, 262–280.

PARK, JUNHO, BILLANT, PAUL & BAIK, JONG-JIN 2017 Instabilities and transient growth of the stratified taylor–couette flow in a rayleigh-unstable regime. *Journal of Fluid Mechanics* **822**, 80–108.

PARK, JUNHO, BILLANT, PAUL, BAIK, JONG-JIN & SEO, JAEMYEONG MANGO 2018 Competition between the centrifugal and strato-rotational instabilities in the stratified taylor–couette flow. *Journal of Fluid Mechanics* **840**, 5–24.

PARK, YOUNG-GYU, WHITEHEAD, JA & GNANADESKIAN, ANAND 1994 Turbulent mixing in stratified fluids: layer formation and energetics. *Journal of Fluid Mechanics* **279**, 279–311.

PELTIER, WR & CAULFIELD, CP 2003 Mixing efficiency in stratified shear flows. *Annual review of fluid mechanics* **35** (1), 135–167.

PHILLIPS, OM 1972 Turbulence in a strongly stratified fluid—is it unstable? In *Deep Sea Research and Oceanographic Abstracts*, , vol. 19, pp. 79–81. Elsevier.

POSMENTIER, ERIC S 1977 The generation of salinity finestructure by vertical diffusion. *Journal of Physical Oceanography* **7** (2), 298–300.

PRASAD, AJAY K 2000 Particle image velocimetry. *CURRENT SCIENCE-BANGALORE-* **79** (1), 51–60.

RAYLEIGH, LORD 1917 On the dynamics of revolving fluids. *Proceedings of the Royal Society of London. Series A, Containing Papers of a Mathematical and Physical Character* **93** (648), 148–154.

RAYLEIGH, LORD 1965 Appendix: The solution of the characteristic value problems. *Proceedings of the Royal Society of London. A* **283**, 550–555.

RUDDICK, BR, MCDOUGALL, TJ & TURNER, JS 1989 The formation of layers in a uniformly stirred density gradient. *Deep Sea Research Part A. Oceanographic Research Papers* **36** (4), 597–609.

RÜDIGER, G & SHALYBKOV, DA 2009 Stratorotational instability in mhd taylor-couette flows. *Astronomy & Astrophysics* **493** (2), 375–383.

SCHMITTNER, ANDREAS, LATIF, MOJIB & SCHNEIDER, BIRGIT 2005 Model projections of the north atlantic thermohaline circulation for the 21st century assessed by observations. *Geophysical research letters* **32** (23).

SHALYBKOV, D & RÜDIGER, G 2005 Stability of density-stratified viscous taylor-couette flows. *Astronomy & Astrophysics* **438** (2), 411–417.

SHERWIN, TOBY J 2010 Observations of the velocity profile of a fast and deep oceanic density current constrained in a gully. *Journal of Geophysical Research: Oceans* **115** (C3).

SIMPSON, JH & WOODS, JD 1970 Temperature microstructure in a fresh water thermocline. *Nature* **226** (5248), 832–835.

SMITH, GP & TOWNSEND, AA 1982 Turbulent couette flow between concentric cylinders at large taylor numbers. *Journal of Fluid Mechanics* **123**, 187–217.

SOMMER, TOBIAS, CARPENTER, JEFFREY R, SCHMID, MARTIN, LUECK, ROLF G, SCHURTER, MICHAEL & WÜEST, ALFRED 2013 Interface structure and flux laws in a natural double-diffusive layering. *Journal of Geophysical Research: Oceans* **118** (11), 6092–6106.

STRANG, EJ & FERNANDO, HJS 2001 Entrainment and mixing in stratified shear flows. *Journal of Fluid Mechanics* **428**, 349–386.

STROGATZ, SH 1994 Non-linear dynamics and chaos (perseus, new york) .

TAYLOR, GEOFFREY I 1923 Stability of a viscous liquid contained between two rotating cylinders. *Philosophical Transactions of the Royal Society of London. Series A, Containing Papers of a Mathematical or Physical Character* **223**, 289–343.

THORPE, SA 1966 Notes on 1966 summer geophysical fluid dynamics (woods hole oceanographic institute, woods hole, ma, 1966) p. 80.

TREFETHEN, LLOYD N 2000 *Spectral methods in MATLAB*, , vol. 10. Siam.

TUCKERMAN, LAURETTE S 2014 Taylor vortices versus taylor columns. *Journal of Fluid Mechanics* **750**, 1–4.

TURNER, JS 1968 The influence of molecular diffusivity on turbulent entrainment across a density interface. *Journal of Fluid Mechanics* **33** (4), 639–656.

TURNER, JOHN STEWART 1979 *Buoyancy effects in fluids*. Cambridge University Press.

VALLIS, GEOFFREY K 2017 *Atmospheric and oceanic fluid dynamics*. Cambridge University Press.

WOODS, ANDREW W, CAULFIELD, CP, LANDEL, JR & KUESTERS, A 2010 Non-invasive turbulent mixing across a density interface in a turbulent taylor–couette flow. *Journal of Fluid Mechanics* **663**, 347–357.

WUNSCH, CARL & FERRARI, RAFFAELE 2004 Vertical mixing, energy, and the general circulation of the oceans. *Annu. Rev. Fluid Mech.* **36**, 281–314.

YAVNEH, IRAD, MCWILLIAMS, JAMES C & MOLEMAKER, M JEROEN 2001 Non-axisymmetric instability of centrifugally stable stratified taylor–couette flow. *Journal of Fluid Mechanics* **448**, 1–21.

ZARON, EDWARD D & MOUM, JAMES N 2009 A new look at richardson number mixing schemes for equatorial ocean modeling. *Journal of physical oceanography* **39** (10), 2652–2664.

ZELLOUF, Y, DUPONT, P & PEERHOSSAINI, H 2005 Heat and mass fluxes across density interfaces in a grid-generated turbulence. *International journal of heat and mass transfer* **48** (18), 3722–3735.

ZHOU, QI, TAYLOR, JOHN & CAULFIELD, COLM-CILLE 2016 Turbulence, mixing and prandtl number effects in stratified plane couette flows. In *VIIIth International Symposium on Stratified Flows*, , vol. 1.